

**3D-printed custom substratum to accentuate fast functional responses from
microbial colonization**

by

Gabriel Felipe Proaño Peña

A dissertation submitted to the Graduate Faculty of
Auburn University
In partial fulfillment of the
requirements for the Degree of
Doctor of Philosophy

Auburn, Alabama
December 15, 2018

Keywords: additive manufacturing, ammonia removal, algal turf scrubber, wastewater
treatment, specific surface area, moving bed biofilm reactor

Copyright 2018 by Gabriel Felipe Proaño Peña

Approved by

Dissertation Committee

Dr. Andres L. Carrano, Co-Chair, Auburn University

Dr. David M. Blersch, Co-Chair, Assistant Professor of Biosystems Engineering

Dr. Richard Sesek, Associate Professor of Industrial and Systems Engineering

Dr. Timothy McDonald, Professor of Biosystems Engineering

Abstract

Recent studies have shown the feasibility of growing benthic organisms on customized substratum by using Additive Manufacturing (AM). Their proven capabilities to fabricate objects at high speed and with complex geometries according to a pre-defined digital design makes the scope of AM to include environmental applications, such as the design of surface topographies for phototrophic biofilm production (Kardel et al., 2015).

This dissertation is part of a cross-disciplinary research effort to investigate the interaction between customized surfaces, algal communities and microbial biofilms in general. The first goal is to investigate the effect of different interstitial surface area distribution on the early colonization of benthic algal biomass in a laboratory-based Algal Turf Scrubber (ATS). 3D printed plates with 4 different surface types were elaborated with extruded Polylactic Acid using Fused Deposition Modelling (FDM) and a Makerbot printer with 0.1 mm layer thickness. Plates with randomized sections were deployed inside an Algal Turf Scrubber under laboratory conditions for 7 days. Treatments having 3 different interstitial surface distributions called *pockets* were compared to a flat surface and tested for their biomass density by freeze-dried weight. Results determined that interstitial pockets provided larger initial algal densities than substratum lacking them, and suggested that an optimal value of pocket distribution exists for maximum colonization.

Moving Bed Biofilm Reactors (MBBR) can have a high performance by having suspended carriers that are free to move in the wastewater to be treated while providing a surface for attachment of active micro-organisms.

The second goal of this work assessed the design, fabrication and functional testing of 3-D biofilter media carriers for use in Moving Bed Biofilm Reactor (MBBR) technology for wastewater treatment. Specific surface area and topology of the biofilter media carrier are among the most important parameters that determine the performance and efficiency of the system. Mathematical models and 3D printing were used to design and fabricate media with three different levels of complexity that provided large specific surface area and refugia to protect biofilm from sloughing. Results not only confirmed the capability to 3D-print gyroid shaped biocarriers with a large surface area, but also demonstrated their functionality for removing ammonia from the prepared synthetic wastewater at rates that were directly related to the specific surface area of the carrier. The results suggest new approaches for design of carriers with high surface area that can increase performance in reactor technologies for wastewater treatment.

Acknowledgments

First, I want to say thanks to God for being within my family all the time and particularly these four years of study abroad.

Thanks to my wife Francisca Burgos and Romina Proaño for all the love and understanding, particularly during the last six months of the program. I am sorry with Romina for not being on her 8th birthday. I promise to work hard to make this effort worth for all of us.

To Francisca, for not only being my wife and life mate but also for advising me and helping me on my research particularly on the topics related to her field of expertise.

To my parents, sisters, and relatives, for encouraging me to keep up regardless of the adversities. Thanks mom Lula for taking care of my duties in Ecuador and for believing in me all the time. To my uncle Victor, for always being present when I needed.

To my father in law, Don Jaime, for the support to my family and for providing free advice and encouragement to me to move on in life. To my mother in law, Dolly, thanks for taking care of my family on their way back to Ecuador.

Thanks to my advisors Dr. Andres Carrano and Dr. David Blersch. Thanks for letting me be part of this novel cross combined field of research. Thanks Dr. Carrano for giving me the opportunity to research with you and learn from your knowledge on surface

engineering and additive manufacturing. Same to Dr. Blersch, for supporting me and my research when I needed, especially in the last two years when my research demands increased and the biological component required special observation. Thanks, both of you for your commitment until the end. Thanks to my committee members, Dr. Timothy Mc Donald and Dr. Richard Sesek for providing expertise and guidance to this research effort.

Special thanks to Dr. Covadonga Arias for letting me use her laboratory resources on my research at any time I needed, I really appreciate it. Thanks to Dr. Virginia Davis, Dr. Matthew Waters, Dr. Brendan Higgins, Dr. Yi Wang, and Dr. Mehmet Billor.

I cannot forget those friends that were there to give me a hand on my research Romi Novriadi, Shamim Naigaga, Candis Ray, John Rains, Jarrod Litton, Pablo Jiménez, Qichen Wang, Haixing Peng, Kathryne Jernigan, Stacey Lafrentz, Alison Aceves, Wenlong Cai, Shangjun Wang, and a special one to T Speir, the administrator of CASIC building, for being always willing to help.

Thanks to Behnam Rasoolian, Sam Bishop, Jorge Zuñiga, Doris, Victor, Jiménez-Pereira and Dunn-Peña family for your friendship.

Thanks to my lab mates: Dr. Kamran Kardel, Dr. Joseph Ekong, Dr. Ali Khoshkhoo, Manjinder Kaur MSc, Mauricio Henriquez MSc, Zahra Karimi and Roger Viticoski for sharing your learning experiences and helping on my work when needed.

Special acknowledgment to the crew of undergraduate students that were part of the last phase of the biofilter project: Mary Beth Cassity, Courtney Eagle, Robert Darden, and Thomas Orzech. Thanks also to the collaborators of the first stage as well: Olivia Elliot, Stephanie Gray, Michael McClay, Bakr Nassief, Ann Nunnelley, Zane Trott, and Eric Vogt.

A special gratitude to Dr. Jorge Valenzuela for opening me the doors to Auburn University, in particular to the Industrial and Systems Engineering department. Thanks for your advice when it was requested. Thanks to Dr. Bill Daniels as well for providing guidance to my family and me when we just arrived at Auburn. Finally, to Ramona Shierling-Nelson for being always willing to help at the department.

I want to thank the Ecuadorian government that by means of the Secretaria Nacional de Ciencia y Tecnología (SENESCYT) funded my doctoral studies.

Table of Contents

Abstract	ii
Table of Contents	vii
List of Tables	xiii
List of Figures	xvi
1. Introduction	1
2. Literature Review	5
2.1. Biofilm formation.....	5
2.2. Algal Turf Scrubber (ATS)	7
2.3. Moving Bed Biofilm Reactor (MBBR)	12
3. Research Questions	17
4. Experiment 1: Impact of the substratum interstitial surface area distribution in highly packed textures on Algal biomass colonization rate	18
4.1. Materials and Methods	18
4.1.1. Design of the substratum plate.	21
4.1.2. The interstitial space generation	22
4.1.3. The arrangement	24
4.1.4. Biomass harvesting	26

4.1.5. Preliminary Experimentation	28
4.1.5.1. Preliminary methodology for biomass determination: Biomass Oven-Drying	29
4.1.5.2. Preliminary Results.....	32
4.1.6. Micro Gravimetric Method for Algal Biomass estimation.....	35
4.1.6.1. Pelletizing Process	35
4.1.6.2. Freeze drying process	37
4.1.6.3. Micro-weighing Process	38
4.2. Results	41
4.3. Discussion	43
4.3.1. Hydrodynamic Analysis	49
4.3.1.1. Average Shear Stress Analysis	51
4.3.1.2. Velocity Profile Analysis	55
4.3.1.3. Velocity Boundary Layer Analysis	59
4.3.1.4. Force Analysis	61
4.3.1.4.1. Lift Forces	63
4.3.1.4.2. Gravitational and Buoyancy Forces.....	64
4.3.1.4.3. Drag Forces	67

5. Experiment 2: Comparative analysis of the functional performance between a traditional and a novel high surface area 3D printed media in a Moving Bed Biofilm Sequencing Batch Reactor for Wastewater Treatment	73
5.1. Materials and Methods	73
5.1.1. Mathematical modeling of the gyroids	73
5.1.2. Fabrication of the gyroids.	77
5.1.2.1. Printing Parameters.....	77
5.1.2.2. Printing post-process.....	78
5.1.2.2.1. Cleaning process for carrier with small surface area.....	78
5.1.2.2.2. Cleaning process for carrier with medium surface area.	79
5.1.2.2.3. Cleaning process for carrier with large surface area.	80
5.1.3. Specific Surface Area characterization of the carriers	80
5.1.3.1. Gyroids' Specific Surface Area determination.....	80
5.1.3.1.1. Gyroids' Surface Area determination	81
5.1.3.1.2. Gyroids' bulk volume determination	82
5.1.3.1.3. Gyroid's Specific Surface Area calculation	83
5.1.3.2. Kaldnes' Specific Surface Area determination	83
5.1.3.2.1. Kaldnes' Surface Area estimation	84
5.1.3.2.1.1. Reverse Engineering technique for Kaldnes' Surface Area determination	84

5.1.3.2.2. Kaldnes' volume determination	85
5.1.3.2.3. Kaldnes' s Specific Surface Area calculation	86
5.1.4. Moving Bed Biofilm Sequencing Batch Reactor (MBBSBR) design, fabrication, and operation	88
5.1.4.1. MBBSBR system components	88
5.1.4.2. Aeration Mechanism for MBBSBR operation.....	89
5.1.4.2.1. Dissolved Oxygen (DO) considerations for nitrifying conditions	90
5.1.4.3. Temperature Conditioning for MBBSBR operation	91
5.1.4.4. Sampling Mechanism for MBBSBR.....	92
5.1.5. MBBSBR operational design	93
5.1.5.1. Ammonia as the substrate for testing carriers' functional performance ..	94
5.1.5.2. Surface area removal rate (SARR) considerations.....	96
5.1.5.3. Surface area loading rate (SALR) considerations.....	98
5.1.5.4. Ammonia-Nitrogen loading removal rate (NH ₃ -N-LRR) considerations ..	98
5.1.5.5. Required carrier surface area (RCSA).....	98
5.1.5.6. Required carrier volume (RCV)	98
5.1.5.7. Alkalinity considerations for Nitrification Processes.....	99

5.1.5.8. Synthetic wastewater preparation.....	100
5.1.6. Bacterial inoculation process of the carriers	102
5.1.7. Acclimatization Process of the carriers in the reactors	103
5.1.8. Ammonia and Nitrate Determination.....	104
5.1.9. Experimental Design.....	105
5.1.9.1. Methodology for hypothesis 1.....	105
5.1.9.2. Methodology for hypothesis 2.....	107
5.1.9.3. Randomization of the jars and carriers	109
5.1.9.4. Protocol for experiment 2	110
5.2. Results	112
5.2.1. Preliminary results for hypothesis 1	112
5.2.2. Results for hypothesis 1	115
5.2.2.1. Ammonia removal results for hypothesis 1.....	115
5.2.2.2. Nitrate production results for hypothesis 1	117
5.2.3. Results for hypothesis 2	123
5.2.3.1. Ammonia removal results for hypothesis 2.....	123

5.2.3.2. Nitrate production results for hypothesis 2	125
5.3. Discussion	131
5.3.1. Economic Impact	139
6. Conclusions	142
7. References	148

List of Tables

Table 1: Recipe of F/2 algae food (Guillard & Ryther, 1962; Guillard, 1975).....	21
Table 2: Experimental treatment levels for interstitial surface area distribution.....	26
Table 3: Kruskal-Wallis test for border effects on biomass productivity.	34
Table 4: Mean values and standard deviations (in parentheses) of algal biomass densities (in mg/cm ²) of each treatment per harvest, and p values from ANOVA between treatments for each harvest.	42
Table 5: Logistics curve fitting for biomass density per day of cultivation.....	44
Table 6: Linear model, growth rate and regression coefficient for the linear region of algal biomass density growth.....	46
Table 7: Linear model, growth rate and regression coefficient for the final region of algal biomass density growth.....	47
Table 8: Best curve fit for Boundary Layer Characterization	60
Table 9: Modification to Code 1 to achieve the three gyroid types.	76
Table 10: Surface Area per carrier unit determination from 3D models	82
Table 11: Bulk volume of gyroids	83
Table 12: Specific surface area per gyroid type	83
Table 13: Surface area information from Netfabb® for the reverse-engineered Kaldnes 1	85
Table 14: Calculated bulk volume for Kaldnes 1	86

Table 15: Calculated specific surface area for Kaldnes 1.....	86
Table 16: Summary of parameters for carriers.....	87
Table 17: Calculated levels of ammonia for the beginning of the run.....	95
Table 18: Values of SARR _{max} and NH ₃ -N at SARR _{max} (at 15°C).....	97
Table 19: Alkalinity requirements for MBBSBR operation.....	99
Table 20: Excess of alkalinity on MBBSBR for buffering at neutral pH.....	100
Table 21: Chemicals composition for <i>Seachem (Salt Mixed) Marine Salt</i>	101
Table 22: Synthetic water recipe for MBBSBR.....	102
Table 23: Experimental design to test hypothesis 1.....	106
Table 24: Experimental design to test hypothesis 2.....	107
Table 25: Medians of the pooled total ammonia nitrogen (in mg/L) per treatment to prove hypothesis 1, and p values for Kolmogorov-Smirnov, Levene, Kruskal-Wallis and Mood's median test.....	119
Table 26: Medians of the pooled nitrate nitrogen (in mg/L) per treatment to prove Hypothesis 1, and p values for Kolmogorov-Smirnov, Levene, Kruskal-Wallis and Mood's median test.....	121
Table 27: Medians of the pooled 8-hour total ammonia nitrogen removal percentage for each treatment (Hypothesis 1), and p values for Kolmogorov-Smirnov, Levene, Kruskal-Wallis and Mood's median and test.....	122
Table 28: Medians of the pooled total ammonia nitrogen (in mg/L) per treatment to test hypothesis 2, and p values for Kolmogorov-Smirnov, Levene, Kruskal-Wallis and Mood's median test.....	127
Table 29: Medians of the pooled nitrate nitrogen (in mg/L) per treatment for Hypothesis 2, and p values for, Kolmogorov-Smirnov, Levene, Kruskal-Wallis and Mood's median test.....	128

Table 30: Medians of the percentage of ammonia removal for each treatment (Hypothesis 2), and p values for ANOVA, Kolmogorov-Smirnov, Levene and Kruskal-Wallis test..	130
Table 31: Logistic curve fitting for ammonia removal on hypothesis 1	134
Table 32: Logistic curve fitting for nitrate production on hypothesis 1	135
Table 33: Logistics curve fitting for ammonia removal on hypothesis 2	137
Table 34: Logistics curve fitting for ammonia removal on hypothesis 2	138
Table 35: Cost analysis for treating 1.3 L of wastewater (15% fill ratio / 200 mL)	139

List of Figures

Figure 1: Mixed community algal biofilm development.....	6
Figure 2: ATS for experiment #1	18
Figure 3: Algal species dominant during the seeding process	19
Figure 4: Light Map over the surface of the ATS (units in $\mu\text{mol m}^{-2} \text{s}^{-1}$).....	20
Figure 5: Substratum Plate for Experiment 1 (Left) Model views; (Right) 3D printed plate.	21
Figure 6: Geometrical model for interstitial space generation	22
Figure 7: <i>On the left: Screen mat wrapped around a PVC sheet. On the right: Introduction of the PVC and screen mat into the surface of the ATS.</i>	24
Figure 8: Randomized arrangement of the plates	25
Figure 9: Schematic of the harvesting tool to capture algal biomass from interstitial spaces	27
Figure 10: The harvesting process: Vacuuming	28
Figure 11: Evaluation of the border effect on algal biomass attachment: (Left) 3D-printed blocking tool (Right) 2D-top view of the blocking effect of the tool for harvesting purposes	29
Figure 12: Summary of preliminary methodology for algal biomass estimation.....	31
Figure 13: Different levels of algal colonization per treatment 5 days after deployment in the ATS.	32
Figure 14: Outcomes from preliminary work for experiment 1.....	33

Figure 15: Biomass Productivity per region type	34
Figure 16: 2 mL and 0.2 mL pelletized algal samples.	36
Figure 17: Lyophilization system for algal freeze drying (capacity: 1.5 L, vacuum: 0.014 mbar, temperature: -50 °C)	37
Figure 18: Microbalance for algal biomass determination. (range: 3 mg., resolution: 1 ug)	38
Figure 19: Illustration of protocol for Experiment 1	40
Figure 20: 3D printed plates between 5 and 9 days of algal colonization.....	41
Figure 21: Logistic curve fit Biomass Density vs Time for the pooled 3 runs results	44
Figure 22: Linear region of the fitted logistic curve	45
Figure 23: Final region of the fitted logistic curve	47
Figure 24: Computational Domain for the 3D-printed part imported into Solidworks-Flow	50
Figure 25: Distribution of the shear stress acting over the whole testing plate	51
Figure 26: Average Shear Stress at the surface of the 3D-printed plates.	52
Figure 27: Visual correlation between the simulated average shear stress (bottom) and the actual starting algal density (top). <i>Plate oriented downstream</i>	54
Figure 28: Algal biofilm development starting close to the center of the plate section. .	55
Figure 29: Water velocity vectors on the 0-pocket treatment	56
Figure 30: Water velocity vectors on the 25-pocket treatment	56
Figure 31: Water velocity vectors on the 36-pocket treatment	57

Figure 32: Water velocity vectors on the 81-pocket treatment	57
Figure 33: Vorticity along the treatments.....	58
Figure 34: Boundary Layer Profile along treatments	59
Figure 35: Semilog plot of the water velocity at the Boundary Layer.....	61
Figure 36: Free body diagram of algal cell debris	62
Figure 37: Theoretical Lift force at the boundary layer of the treatments	65
Figure 38: Theoretical Particle Reynolds number per treatment at the boundary layer.	68
Figure 39: Theoretical drag force per treatment at the boundary layer.....	70
Figure 40: Drag coefficient as function of the Particle Reynolds number for the treatments at the boundary layer.....	71
Figure 41: Gyroid surface.....	74
Figure 42: Spherical gyroid surface.....	75
Figure 43: Netfabb® workspace for surface area determination of 3D models	81
Figure 44: K1 carrier, from left to right: digital file, 3D printed part, commercial.....	85
Figure 45: Picture and sketch of part of the MBBSBR system for experiment 2	88
Figure 46: Sketch of a single MBBSBR and components	89
Figure 47: Picture and sketch of the aeration ring inside the MBBSBR.....	90
Figure 48: 100 mL syringe for taking water samples.....	92
Figure 49: Influence of ammonia nitrogen and DO concentration on removal rate at 15°C (Ødegaard, 1999).....	96
Figure 50: Water samples after the dosage of reagents for color development prior to photometric measurements.....	105

Figure 51: Illustration of Hypothesis 1 and Hypothesis 2.....	108
Figure 52: Randomized locations per run.....	109
Figure 53: Workflow per run	111
Figure 54: Ammonia-N Percentage Removal during the first nine 8 hour-runs.	112
Figure 55: Nitrate-N production during the first nine 8 hour-runs.	113
Figure 56: Raw Ammonia-N and Nitrate-N determination. In A) Ammonia-Nitrogen on Run 7, B) Nitrates-Nitrogen on Run 7, C) Ammonia-Nitrogen on Run 8, D) Nitrates-Nitrogen on Run 8.	114
Figure 57: Ammonia concentration vs. time for run 1 (Hypothesis 1).....	116
Figure 58: Ammonia concentration vs. time for run 2 (Hypothesis 1).....	116
Figure 59: Ammonia concentration vs. time for run 3 (Hypothesis 1).....	117
Figure 60: Nitrate concentration vs. time for run 1 (Hypothesis 1)	118
Figure 61: Nitrate concentration vs. time for run 2 (Hypothesis 1)	118
Figure 62: Nitrate concentration vs. time for run 3 (Hypothesis 1)	119
Figure 63: Pooled total ammonia concentration vs. time (Hypothesis 1).....	120
Figure 64: Pooled nitrate concentration vs. time production (Hypothesis 1).....	121
Figure 65: 8-hour TAN removal percentage for each biocarrier type for Hypothesis 1.	122
Figure 66: Ammonia concentration vs. time results for run 1 (Hypothesis 2)	123
Figure 67: Ammonia concentration vs. time results for run 2 (Hypothesis 2)	124
Figure 68: Ammonia concentration vs. time results for run 3 (Hypothesis 2)	124

Figure 69: Nitrate concentration vs. time results for run 1 (Hypothesis 2).....	125
Figure 70: Nitrate concentration vs. time results for run 2 (Hypothesis 2).....	126
Figure 71: Nitrate concentration vs. time for run 3 (Hypothesis 2)	126
Figure 72: Pooled ammonia concentration vs. time (Hypothesis 2)	128
Figure 73: Pooled nitrate concentration vs. time (Hypothesis 2)	129
Figure 74: 8-hour TAN removal percentage for Hypothesis 2.	130
Figure 75: Total ammonia nitrogen results fitted in a logistic curve (Hypothesis 1).....	133
Figure 76: Nitrate production results fitted in a logistic curve (Hypothesis 1)	135
Figure 77: Total ammonia nitrogen results fitted in a logistic curve (Hypothesis 2).....	137
Figure 78: Nitrates production results fitted in a logistic curve (Hypothesis 2)	138
Figure 79: Cost and Removal Rate by biocarrier type.....	140

1. Introduction

Wastewater is the water that has been utilized by population from municipal or industrial effluents under different applications and whose new composition makes it no longer reusable without a proper treatment. The diversity of constituents that merge into sewage can carry pathogens creating more unfavorable conditions for further human consumption (Metcalf & Eddy, 2003). With the increase in regulatory policies around the world (Cai et al., 2013), it is necessary to develop strategies to assess this problem. The process of wastewater treatment involves a series of steps where pollutants are gradually removed until reaching a certain level of treatment for public exposure. Preliminary treatment includes coarse screening and grit removal of large objects. After that, primary treatment is characterized by the removal of sediments and floating solids present. Most of the wastewater treatment plants end with secondary treatment that uses microbial removal of the residual organic matter still present from the primary effluents. Alternatives for the process include Activated Sludge and Trickling Filtration. Finally, in special cases, tertiary and advanced treatment is used for the removal of nutrients that have not been removed in the earlier stages.

Many biotechnologies are employed for pollutant removal in wastewater treatment by using attached microbial communities of algae (e.g. Algal Turf Scrubbers) or bacteria (e.g. Moving Bed Biofilm Reactors). Algal treatment is considered a sustainable option to provide an effective process for wastewater remediation. The main reason is that the nutrients required for algal cultivation such as nitrogen or phosphorus are found available from wastewater sources. Algal growth can uptake nitrogenated compounds such as

nitrites (NO_2^-), harmful for aquatic animal's life, but important nutrient that support algal growing conditions. In a similar way, bacterial cultivation keeps the goal of enriching its biomass by removing organic carbon compounds from wastewaters while enhancing the uptake of nutrients (the water's pollutant). Both microbial processes are beneficial from an economic standpoint because the production of algal biomass has an economic value as biofuel and as bioproduct (Christenson & Sims, 2011) and the sludge collected in clarifiers, in addition to the fact that it is continuously recycled, it is anaerobically digested and used for biogas production (Bachmann et al., 2015).

Algae are heterogeneous assemblages of photosynthetic organisms ranging in size from single cells (microns) to giant seaweeds (decameters) (Graham et al., 2016) with the capability to uptake dissolved elements and incorporate them into their biomass. These organisms base their metabolisms on the capture of light, generally from natural sources, to produce oxygen after sequestering carbon dioxide from their surroundings in a mechanism called photosynthesis (Barber & Tran, 2013). This natural process can be reproduced either in the field or under controlled laboratory conditions to optimize subsequent processes such as biomass production or wastewater treatment (Bhatnagar et al., 2011; Cho et al., 2011; Golueke et al., 1957).

An economical alternative for algal cultivation is Algal Turf Scrubber (ATS) technology. ATS takes advantage of periphytic algae, a mixed community of algae and microorganisms including bacteria, attaching to surfaces as a turf of algal filaments (no more than several centimeters tall). The design of ATSSs results in high algal production

to remove a large quantity of dissolved pollutants from the influent water. The ATS is characterized by the conditions of the intense light source and the implementation of a water surge generator that enhances mixing of the nutrients along the water body. Maintenance includes frequent harvest to avoid algal death from the basal region of the turf (Adey & Loveland, 2011) and to remove biomass harboring the pollutants.

The bacterial approach for the fixed film technology is the Moving Bed Biofilm Reactors (MBBR), which emerged in Europe in the late 1980s and early 1990s (Ødegaard, 1999; Ødegaard et al., 1994) at the Norwegian University of Science and Technology in cooperation with a Norwegian company (Anox Kaldnes AS) (Borkar et al., 2013). MBBR technology is based on biocarriers suspended inside the wastewater under treatment. These biocarriers move freely with advective mixing while providing a bed for microbial growth. For the growth of aerobic bacteria, aerators are incorporated into the reactor, while for anaerobic bacteria mixers are mounted instead. A combined operation of aerators and mixers can provide anoxic conditions as well. Applications include nitrification processes where the ammonia present in the wastewater oxidizes under the presence of oxygen by the mediation of nitrifying bacteria such as *Nitrosomonas sp.* and *Nitrobacter sp.* that convert into nitrite and then into nitrates respectively.

Observations taken from natural waters and laboratory research have shown that the early stages of the microbial biofilm depend on the topographic conditions provided by the substratum. Surface parameters such as roughness affect the adhesion, settlement, and attachment of the first microbial cells during biofilm development (Burkholder &

Wetzel, 1989; Miller et al., 1987; Vadeboncoeur et al., 2006). In this context, Additive manufacturing (AM), is an emerging technology that has the capability to fabricate suitable 3-D substratum for applications related to wastewater treatment processes.

Additive Manufacturing or 3D printing, fabricate 3-D objects by building up material, layer upon layer, according to a pre-defined digital design. The high speed and ability to print complex geometries makes the scope of AM not limited to reproduce designs for small batch manufacturing; but also allows it to include environmental applications such as the design of surface topographies for microbial colonization (Kardel et al., 2015). The level of resolution of AM to reproduce plastic polymer or nylon parts at the micron scale includes complex 3-dimensional geometrical patterns and features that can enhance the conditions required for the growth of algal or bacterial biofilms (Dong et al., 2015; Elliott et al., 2017). To date, no research has focused on the evaluation of 3D printed high-surface area carriers for biofilms to remove ammonium from wastewater and evaluate its removal rates against traditional biocarriers. Another unexplored area of research is the optimization of the configuration of interstitial spaces (zones of the substratum generated between tightly-packed 3D printed hemispheres) (Kardel et al., 2015) affecting the early onset colonization of algal biofilms. Favorable results on both proposed studies have the potential to accelerate nutrient removal processes in wastewater treatments.

2. Literature Review

2.1. Biofilm formation

Biofilm development is one of the first stages during the algal turf formation. It can be defined as a mixed community of microorganisms attached to a substratum under the presence of water for extended periods of time. The photosynthetic biofilm is the result of favorable conditions in terms of nutrient availability, symbiotic relationships among microorganisms and environmental factors.

Biofilm is characterized by the presence of extracellular polymeric substances (EPS) that bind cells themselves and to surfaces. In algae, EPS constitute the mucilage excreted by algae whose functional role varies. It helps to hold together a group of cells to form colonies, but also works as a sheath to enclose algal filaments as a mechanism of protection against herbivores (Graham et al., 2016). EPS is not only generated by active secretion, but also from cell lysis or debris adsorbed from the surrounding environment. The result is a matrix of polysaccharides, proteins, nucleic acids, and lipids that provide a microenvironment rich in nutrients that favors either bacterial or algal growth (Schnurr & Allen, 2015). The production of EPS varies depending on the environmental conditions. For example, the diatom *Amphora coffaeiformis* shows an increased production of EPS when exposed to substratum with good adhesion strength with EPS (Becker, 1996)

The presence of bacteria, algae or EPS in the biofilm depends on its maturity. Figure 1 illustrates different proposed stages of the photosynthetic biofilm (Schnurr & Allen, 2015).

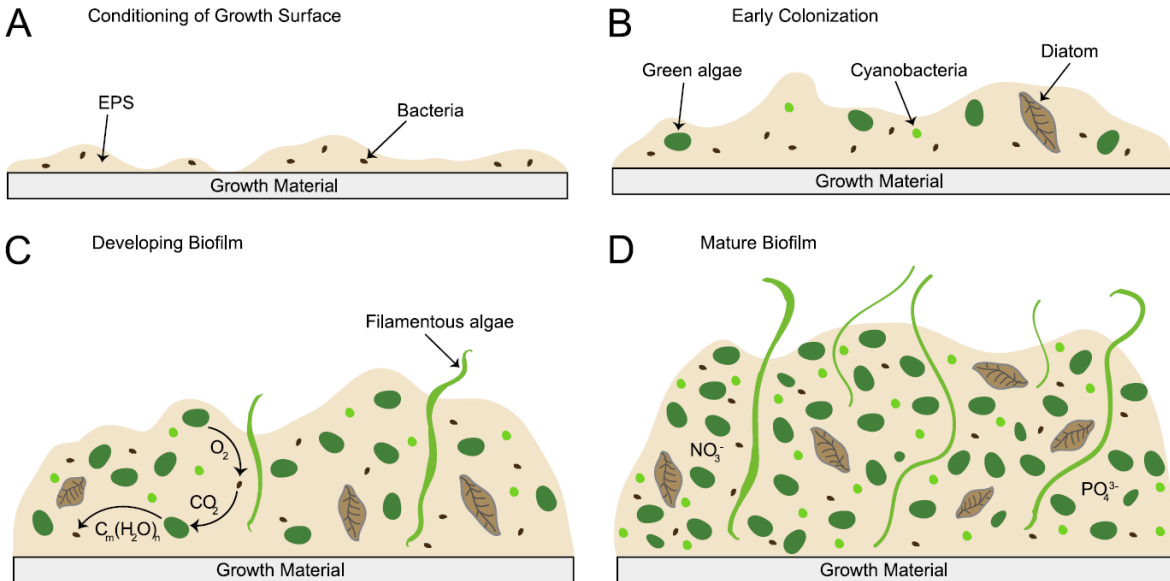


Figure 1: Mixed community algal biofilm development taken from (Schnurr & Allen, 2015)

Figure 1A refers to the early stage when the proportion of EPS is greater in comparison to the presence of algae and bacteria (Barranguet et al., 2004; Zippel & Neu, 2005). Figure 1B and 1C show the following stage after the establishment of the EPS matrix, where bacteria migrate to the upper layers of the biofilm to compete for nutrients (Mack et al., 1975). Figure 1D illustrates a mature algal biofilm upon favorable light and nutrient availability.

Surface roughness plays a role on the protection of the developed biofilm. The initial adhesion of bacteria has been reported to occur at locations where they are sheltered against shear forces in such a way that the attachment process turns irreversible (Teughels et al., 2006). It has also been observed that when the substratum has been exposed to cleaning processes, biofilm growing on rough substratum promotes fast

regenerations due to the rapid reproduction of remaining species without the need of recolonization (Quiryneen & Bollen, 1995).

2.2. Algal Turf Scrubber (ATS)

ATS technology uses turf algae (generally filamentous) attached to a plastic screen to purify natural waters under conditions of abundant sunlight, good dispersion of nutrients (driven by wave action), and strong currents (Adey & Loveland, 2011). The water treatment process is accomplished by the algal uptake of nutrients from polluted waters that are later removed with the algal biomass by frequent harvesting processes.

The first attempt to implement ATS technology at a large scale (154 m. long x 6.7 m wide) for wastewater treatment is reported by (Craggs et al., 1996) from a facility located in Paterson, California. The yearly mean removal of nitrogen and phosphorus was 1.11 ± 0.48 gN/ m² /day and 0.73 ± 0.28 gP /m² /day, respectively. Implementations at a medium scale such as in (Sindelar et al., 2015) were able to identify optimal inflow regimes, rates, and phosphorus concentrations for optimal algae scrubber total phosphorus (TP) removal. Experiments in natural environments, such as on a secondary canal, also assessed the permanent removal of excess phosphorus from agricultural run-off (Adey et al., 1993). Reported results showed a total phosphorus removal range of 380-507 kg P/ha/year, suggesting the possibility of scaling-up to larger water treatment systems.

Water flow dynamics are a key determinant for algae colonization patterns. Studies show that water laminar flow allows the establishment of benthic algal biofilm because of

interactions at the interface between the surface (substratum) and the aquatic medium (Irving & Allen, 2011). On the other hand, turbulent flows can stimulate the production of attached algae through the delivery of critical nutrients (Biersch et al., 2013). Understanding the role of flow turbulence in algal growth provides an approach for modulating algal production when a saturation relationship exists with increasing nutrient concentration.

Substratum characteristics are another main variable for optimal algal growth. Experimental research has emphasized the importance of microtopography on algal settlement and germination mostly on spores of marine macroalgae (Harlin & Lindbergh, 1977; Norton & Fetter, 1981; Reed et al., 1988), and corresponding analogies also take place for algae in freshwater systems (Sheath, 1984). Studies regarding benthic algae agree on the important role that substratum has on the formation of algal biofilm as part of the natural mechanism for algal community establishment. It has been determined that substratum such as rock containing microcrevices and depressions where spores can settle without being dislodged by abrasion or current (Burkholder & Wetzel, 1989; Miller et al., 1987). The effects of surface texturing on algal cell attachment have also been a subject of investigation. Particularly, the affinities between algal cell size with the predesigned textures on the substratum have been identified. (Cui et al., 2013) tested the responses of *Scenedesmus dimorphus* and *Nannochloropsis oculata* under the presence of ridges, pillars, and grooves microfabricated on solid carriers. Results showed that algal cells were able to penetrate through the features, but the actual attachment was preferred when the diameter of the settling cell was close to the feature size, providing support to

the contact point theory (Scardino et al., 2006). In general, the capability to manipulate topographic parameters of the substratum constitutes a major factor to control the development of the biofilm (Burkholder, 1996).

Several fabrication processes have been implemented with the objective of manipulating topographic parameters thus having a better control on algal biofilm formation. (Granhag et al., 2004) used pressing techniques in combination with heat to mold plankton nets achieving micro topographies characterized by their mean roughness depth (R_z) in the range (R_z : 25-100 μm) with the objective of testing settlement and adhesion preferences on *Ulva linza*. (Cao et al., 2009) created dimple features (6-8 μm diameter, 2-3 μm depth) on stainless steel by using Nd: YVO₄ laser to test surface roughness affinities on the attachment of *Scenedesmus dimorphus*. (Hassan et al., 2012) fabricated different surface roughness by means of traditional abrasive processes to test the attachment behavior of *Oscillatoria sp.* under the presence of shear stress. (Cui et al., 2013) used laser micromachining and micro-rolling milling fabricated topographies (ridges: 1-5 μm , pillars: 2-30 μm , groove, 10-100 μm) on two different polymers (nylon and polycarbonate) to study the attachment preferences of *Scenedesmus dimorphus* and *Nannochloropsis oculata*. Current research efforts are taking advantage of the benefits of Additive Manufacturing by designing complex and reproducible features that are not possible to fabricate with traditional techniques (Kardel et al., 2015; Kaur, 2016). Thus, the capability to manipulate surface topography parameters by the inclusion of 3D printed features now allows researchers to gain more control of the algal biofilm colonization and microorganisms in general.

To determine that algal biofilms can colonize 3D printed substratum, (Kardel et al., 2015) used PolyJet technology to fabricate circular plates with quadrants containing hemispherical surface features of increasing scales characterized by their averaged roughness (R_a)(500, 1000 and 2000 μm and a smooth section R_a : 0.198 μm as control). The plates were placed in a bench-scale ATS inoculated with a mixed algal community dominated by *Spirogyra communis* for 45 continuous days. Direct observation showed evidence of a surface roughness effect on biomass density. Furthermore, the same study reported the presence of algal biofilm firmly attached on regions denominated *interstitial spaces* even after the harvesting processes that included mechanical scraping, rinsing and vacuuming. These residual patches containing algal biomass were suggested as zones of refugia useful for further regrowth.

In the same direction, (Blersch et al., 2017) demonstrated the capabilities of 3D printed surfaces with the capability to influence the colonization of various species in a mixed periphyton community in natural streams. The 3D printed plates included six different topographic sections of tightly-packed hemisphere patterns of average area peak-to-valley height of 100, 500, 1000, 1500, and 2000 μm and a smooth section as the control. After 30 days of exposure in a local stream, biomass from the plates were harvested and was keyed via microscopy to the genus level. As a result, it was determined that *Microspora wileana* has a preference for feature sizes lower than 500 μm , while *Sigeoclonium tenue* prefers feature sizes less than or equal to 100 μm and greater than or equal to 1500 μm . The fundamentals for such observations rely on the formation of

quiescent zones on the substratum. These zones disrupt the turbulent regime of the overlying flow at the boundary layer due to the interaction between the topographic features on the substratum and the overlying flow. It was suggested that different cell sizes of different algal species interact with these quiescent zones in colonization.

The existence of quiescent zones in a flow field is definitively applicable to understand algal biofilm formation. (Nikitin, 1973) considers benthic biofilm of algae in microzones at the liquid-solid interface whose environmental conditions differ from the surrounding aquatic environment. (Vogel, 1981) refers to the overlying boundary layer of quiescent water as a region where solutes travel only by slow diffusion, isolating the biofilm community to some degree from the medium. Thus, the presence of features on the substratum as topography have the potential to form quiescent zones and induce the creation of microhabitat chemically distinct and nutrient-enriched relative to the overlying water (Burkholder, 1996). With this context, the presence of algal biofilm inside the interstitial spaces on the 3D printed plates in (Kardel et al., 2015) after harsh harvesting action can be used as evidence of the formation of quiescent zones on such regions. It could be possible that with the generation of features on the substratum surface some mechanisms already identified in nature are being mimicked. For example, corals perform by themselves the generation of microvortices to enhance mass transfer of nutrients (Shapiro et al., 2014). If different levels of algal densities were identified at the interstitial spaces, it might be the result of different levels of disruption on the characteristics of the diffusive boundary layer, just as coral perform in nature. Interstitial spaces have the potential to be part of a privileged region of the substratum where the

development of algal biofilm can even be accelerated due to the possible formation of nutrient-enriched microhabitat on it. If the formation of such regions is confirmed, there is an avenue to improve algal biomass productivities. To date, no studies have addressed the optimal configuration of interstitial spaces between features on surface topographies affecting the early onset colonization of algal biofilms.

2.3. Moving Bed Biofilm Reactor (MBBR)

Several applications involving the implementation of MBBR for secondary and even tertiary levels of wastewater treatment have been reported. These include pharmaceutical wastewater (Brinkley et al., 2008), petroleum contaminated waters (Mahmoudkhani et al., 2012), pulp and paper industry wastes (Rusten et al., 1994) and piggery wastewater treatment (Sombatsompop et al., 2011). An advantage of MBBR technology is that the volume of wastewater to be treated is not solely a function of the size of the reactor designed for the process. Instead, the process relies on engineering configurations within which biocarriers considerations gain more relevancy. For example, by increasing the media fill fraction (the volume of biocarriers provided to the reactors with respect to the required volume of wastewater under treatment) surface area is increased and the process can be improved due to the more available substratum for the microorganisms to attach on to perform their metabolic activity. Another alternative is to increase the specific surface area (SSA) of the biocarrier (the ratio of the total surface area of the biocarrier to its bulk volume). Thus, biocarrier SSA is a critical parameter to the performance of MMBR technology.

Reproducing water treatment processes at a lab scale is necessary to test the performance of new designs for biocarriers. For research purposes, small to medium scale reactors are used to increase the number of experimental treatments, experimental units and statistical power (Colt et al., 2006a). Several considerations and aspects require control including an air supply, dissolved oxygen, the microbial community, nutrient loading rate, and temperature. For applications regarding nitrogen removal, MBBRs are commonly used for nitrification. Air supply injects oxygen to enhance nitrogen oxidation, while at the same time achieving mixing of the treated water. Both air velocity and the injected oxygen that later dissolves in water are factors that determine nitrogen removal rates (Kamstra et al., 2017; Rusten et al., 2006). (Kamstra et al., 2017) conducted a research to study the effect of mixing and scale on MBBRs. Specifically, at a small scale (0.8 L), it was found that superficial air velocity tested at a range of velocities (2.2, 5.9, 9.3, 13.9 m/h) and media fill fractions (0, 25, 50 and 75%) have a strong effect on mixing time. However, in the same study, mixing time proved to have an effect on total ammonia nitrogen (TAN) removal. At 25% filling, the maximum rate was $0.85 \text{ gN m}^{-2} \text{ d}^{-1}$; while at 50 filling percentage, the rate was only $0.55 \text{ gN m}^{-2} \text{ d}^{-1}$. Additionally, TAN removal was reduced when the superficial air velocity was below 5 m.

Previous investigations have assessed the effect of different operational factors (hydraulic retention time, temperature, type of carrier and carrier filling ratio) on the community structure of the bacterial biofilm present on MBBRs (Calderon et al., 2012). Results show that media fill fraction (50%) is a significant factor that influences species diversity where bacterial community. Investigations also show the influence of temperature on TAN

removal rates. (Kinyage & Pedersen, 2016) went into detail on this regard, and after testing the performance of biocarriers across a range of temperatures (6 - 36 °C), it was determined ammonium and nitrite removal kinetics were fastest at 30°C. This temperature matches with (Hofman & Lees, 1953) that exclusively studied the metabolism of *Nitrosomonas*, where all experiments to investigate the oxidation of ammonia to nitrite were at 30°C.

The establishment and development of the amount of biofilm on the carrier's surface is a factor that needs special control. For example, in nutrient removal processes involving nitrogen, while the biofilms' microbial activity performs the oxidation and removal of ammonia nitrogen, an excess of the biofilm growth can result in its detachment from the surface of the carrier. This, in fact, may transform the original reactor's design (moving bed biofilm) into a hybrid unit (moving bed biofilm and suspended sludge) (Bassin et al., 2016). Furthermore, as the biofilm thickens, less oxygen penetrates to the deepest layer of biofilm (Barwal & Chaudhary, 2015), in consequence reducing its capacity for nutrient removal.

Several research efforts have tried to investigate variants on the design of the carrier to improve its performance in MBBR through the amount of bacterial biofilm. These variations include shapes, sizes, and materials (Chu & Wang, 2011; Gong et al., 2011; Levstek & Plazl, 2009). The design of the filter media relies on several considerations, such as material density, buoyancy, and settleability, that need to be reported when new designs are issued (Colt et al., 2006) because of their impact on the performance of an MBBR. Avoiding media clogging is also an important consideration. (Hayder et al., 2017)

reported the principal causes of clogging in detail, where the thickness of the biofilm, the water flow regime, the geometry of the biocarrier, and the levels of aeration are major factors.

Additive manufacturing is a cutting-edge technology that has been emerging recently and provides the capability to fabricate predesigned models of biocarriers with high levels of complexity in their geometry and a higher resolution for desired microtextures compared to traditional fabrication processes. The feasibility of achieving microbial colonization on 3D printed substratum has already been determined by (Carrano et al., 2016; Kardel et al., 2015) when it was implemented as cubic gyroids in phototrophic biofilm reactors. (Dong et al., 2015) reported the fabrication of three fullerene-type biocarriers using Laser Selective Sintering (SLS) technology and evaluated biofilm growth performance. Under simulated sewage wastewater conditions in which all biocarriers type were fixed at the same time into the same sequencing batch reactor, results showed that biofilm growing on the 3D biocarriers were thicker than that on the outer regions of the K3, but thinner if compared from the inner walls. (Elliott et al., 2017) produced 3D printed gyroid-based biofilters by implementing PolyJet Technology and established the feasibility of implementing such technology for biocarrier fabrication in MBBR reactors for nitrification.

To date, no research has focused on the evaluation of 3D printed carriers to remove ammonia from wastewater and evaluate its removal rates against traditional biocarriers. The 3D printed carriers reported in (Elliott et al., 2017) have the potential to accomplish faster nutrient removals due to the large specific surface area. Additionally, such gyroid-

type carriers are characteristic for the complexity of its geometry that makes it possible to achieve unique hydrodynamic flow patterns that do not only favor the trap of biomass but also accelerate the start-up of MBBRs (Chen et al., 2015). Given the fidelity of PolyJet technology, different levels of void space can be designed in such a way that an optimal value of specific surface area can be determined to provide maximized ammonia removal rates.

3. Research Questions

This study aims to provide support to ways to improve the processes of wastewater treatment using fixed biofilm reactor through solid substratum engineering. Two demonstrations of this approach include the manipulation of interstitial surface area distributions on the substratum for the growth of algal turfs and design of novel large surface area biocarriers for nitrification MBBRs.

Guiding research questions that emerge from this topic are as follows:

- Research question 1: What is the effect of the distribution of the interstitial surface of substratum topography on the early onset colonization of benthic algae in an Algal Turf Scrubber (ATS) apparatus?
- Research question 2: What is the effect of specific surface area and geometry of 3D printed biocarrier on the nitrification removal of ammonia from wastewater in a Moving Bed Biofilm Reactor?

The approach is achieved by:

- Laboratory ATS experiments to investigate early colonization on designed topographies with varying interstitial space.
- Laboratory scale Sequencing Batch MBBRs to measure nitrification rates using designed carriers of varying SSA and geometry.

4. Experiment 1: Impact of the substratum interstitial surface area distribution in highly packed textures on Algal biomass colonization rate

The aim of the first experiment is to investigate the effect of different interstitial surface area distribution on the early onset colonization rate of benthic algae biomass in a laboratory-based bioreactor. Three treatment levels of interstitial surface area distribution and a control level were considered to observe the effect on algal biomass density over time.

4.1. Materials and Methods

The experimentation was carried out in the ATS (Algal Turf Scrubber) located at the Center for Advanced Science, Innovation and Commerce (CASIC) building at Auburn University (Figure 1). It comprises a 30-gallon reservoir with nutrient media that is continuously pumped through a tipping bucket that provides a periodic water wave surge to a 1 m² of shallow algal turf (2 cm depth) to finally return to the container.

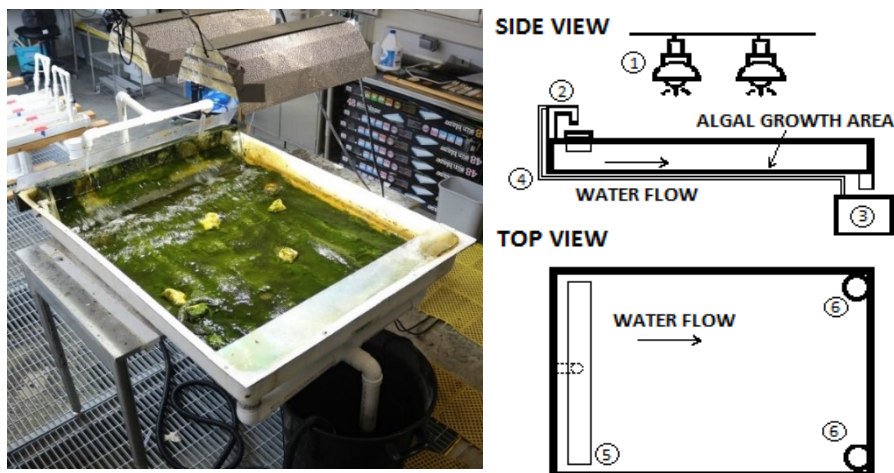


Figure 2: ATS for experiment #1
(1: metal halide lamps 2: water inlet 3: water reservoir 4: water return line 5: Tipping bucket 6: drainage)

The ATS was seeded with harvested algae from the algal reactors reported in (Ekong, 2017) located in CASIC building as well, which was predominantly established with microalgal communities of *Microscopora floccose* and *Mougeotia scalaris* (see Figure 3) derived from a natural community collected from Chewacla Creek in Auburn, Alabama.



**Figure 3: Algal species dominant during the seeding process
(Magnification: 800X)**

The ATS was fed by using a method that keeps the behavior of a continuous mode reactor. To achieve this, 15 gallons of water were replaced daily with fresh nutrient media, using 7.5 ml of commercial Proline F/2 algae food (Pentair Co., Apopka, Florida), which is based on the (Guillard, 1975) F/2 formation recipe (see Table 1). The flow rate was kept at 45 L min^{-1} with a tipping frequency of 4 min^{-1} . During experimentation, daily measures of temperature (24.6 ± 0.5)[$^{\circ}\text{C}$], conductivity (0.08 ± 0.01)[mS], and pH ($7.65.6 \pm 0.22$) were taken from the surface water of the reactor prior to water replacement (see Appendix I). The average nitrate concentration was 21 mg/L whereas phosphate concentration was below 5 mg/L. Continuous external light (photoperiod 24:0) was provided by two 400 W metal halide grow lamps (Virtual Sun®, La Verne, California) located above the cultivator. To make sure the algal turf of the reactor was exposed to a

homogenous incidence of light, several light intensity measures were taken close to its surface by using a quantum flux meter probe (LI-250 Light Meter and LI-190 Quantum Sensor, LI-COR Biosciences, Lincoln, Nebraska, USA). Light intensity at the surface water was recorded $(241 \pm 51) [\mu\text{mol m}^{-2} \text{s}^{-1}]$. Figure 4 displays the light intensity map for different regions of the ATS.

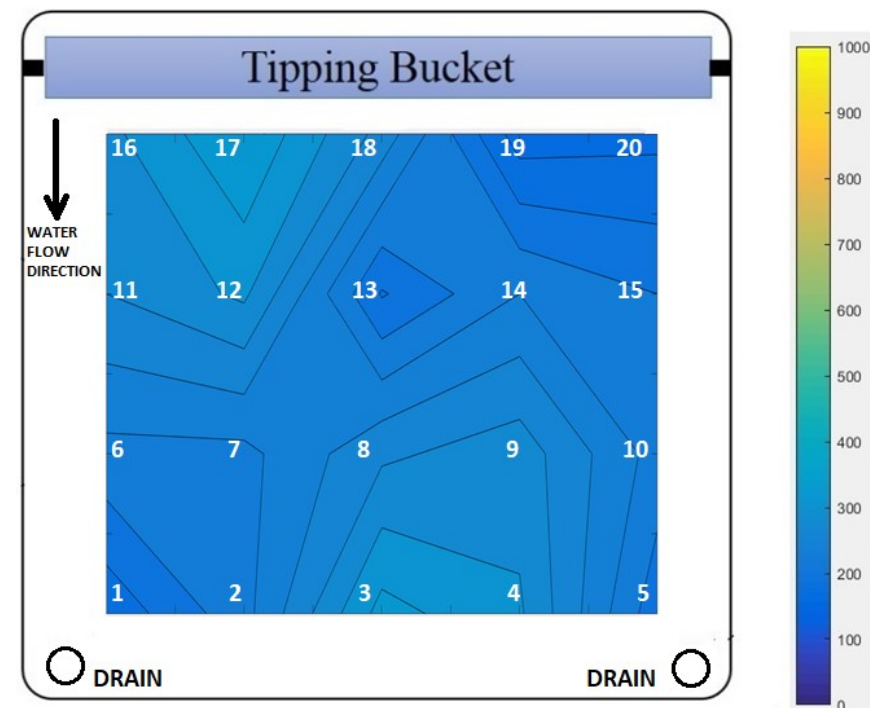


Figure 4: Light Map over the surface of the ATS (units in $\mu\text{mol m}^{-2} \text{s}^{-1}$)
Numbers represent locations where light intensity measures were taken

**Table 1: Recipe of F/2 algae food (Guillard & Ryther, 1962; Guillard, 1975)
Taken from (Kaur, 2016)**

Chemical Component	Mass (g mol ⁻¹)	Final concentration (M)	Final concentration (g L ⁻¹)
NaNO ₃	84.98	8.82×10 ⁻⁴	0.075
NaH ₂ PO ₄ ·H ₂ O	137.97	3.62×10 ⁻⁵	0.005
FeCl ₃ ·6H ₂ O	270.30	1.17×10 ⁻⁵	0.0032
MnCl ₂ ·4H ₂ O	197.01	9.10×10 ⁻⁷	1.79×10 ⁻⁴
ZnSO ₄ ·7H ₂ O	186.00	7.65×10 ⁻⁸	2.19×10 ⁻⁵
CoCl ₂ ·6H ₂ O	237.00	4.20×10 ⁻⁸	9.95×10 ⁻⁶
CuSO ₄ ·5H ₂ O	249.00	3.93×10 ⁻⁸	9.79×10 ⁻⁶
Na ₂ MoO ₄ ·2H ₂ O	237.88	2.60×10 ⁻⁸	6.18×10 ⁻⁶
Thiamine · HCl (vitamin B1)	333.27	2.96×10 ⁻⁷	1.00×10 ⁻⁴
Biotin (vitamin H)	242.45	2.05×10 ⁻⁹	5.00×10 ⁻⁷
Cyanocobalamin (vitamin B12)	1355.4	3.69×10 ⁻¹⁰	5.00×10 ⁻⁷
Na ₂ SiO ₃ ·9H ₂ O	284.04	1.06×10 ⁻⁴	0.030
Na ₂ EDTA·2H ₂ O	374.24	1.17×10 ⁻⁵	0.0044

4.1.1. Design of the substratum plate.

The substratum plate for this experiment was 19.2 cm x 4.8 cm with sections of dome-shaped features with different radii as testing treatments, all having the same height over the sections of the plate as shown in Figure 5.

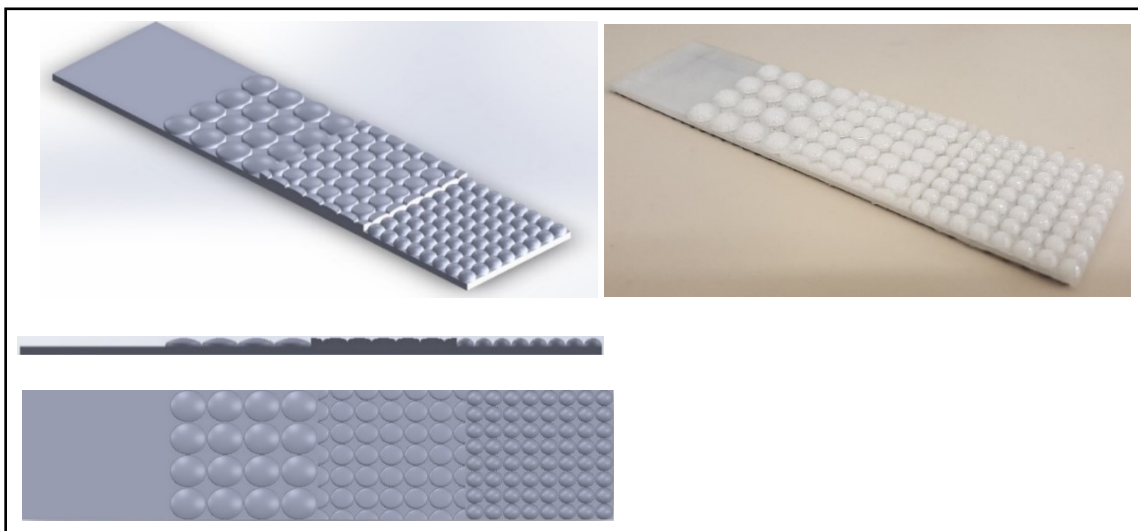


Figure 5: Substratum Plate for Experiment 1 (Left) Model views; (Right) 3D printed plate.

Every section of each plate was designed in Solidworks® (Dassault Systèmes SolidWorks Corp., Waltham, Massachusetts) and fabricated in Natural PLA (Polylactic Acid, MakerBot Filament, part number: MP05612) by printing on a Makerbot FDM (Fused Deposition Modelling) printer with 0.1 mm layer thickness at a 195°C extrusion temperature. Once all the sections were printed, they were glued onto a 1-mm mesh plastic screen with silicone glue (aquarium grade), until assembling a 4-section plate as shown on same Figure 5.

4.1.2. The interstitial space generation

The generation of interstitial spaces (green regions in Figure 6) was achieved by the projection of curved features as visualized on the same top view.

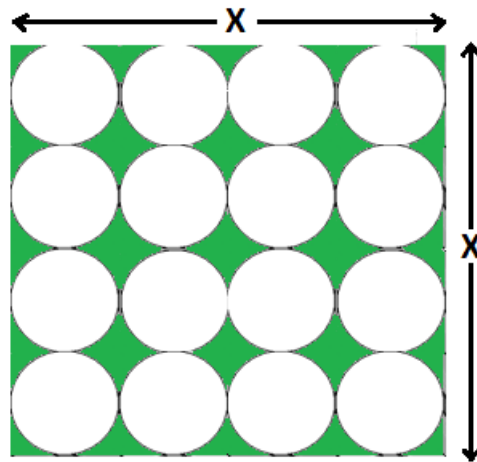


Figure 6: Geometrical model for interstitial space generation

The total interstitial surface area generated by the close-packed features can be estimated by geometry.

For any squared section taken from the 3D printed plate with side length x , with n features of the identic circular projected surface area and m features on each side, the projected surface area of the whole squared section (S_s) is given by:

$$S_s = x^2$$

Since the projected surface area of each hemisphere feature (S_F) is circular 2D-geometry, it can be calculated by πr^2 , where r is the radius of each projected hemisphere given by

$$\frac{x}{2m}$$

Hence,

$$S_F = \pi \left(\frac{x}{2m} \right)^2 = \frac{\pi x^2}{4 m^2}$$

The total feature projected surface area S_{TF} (considering all hemispheres) is $n S_F$, or:

$$S_{TF} = \frac{n \pi x^2}{4 m^2}$$

Thus, the total interstitial surface area (S_I) can be calculated by subtracting the total feature projected surface area from the projected surface area of the whole section:

$$S_I = S_s - S_{TF} = x^2 - \frac{n \pi x^2}{4 m^2}$$

But, $n = m^2$

$$S_I = x^2 - \frac{m^2 \pi x^2}{4 m^2} = x^2 - \frac{\pi x^2}{4} = x^2 \left(1 - \frac{\pi}{4} \right)$$

Or:

$$S_I = 0.215 x^2$$

The previous analysis shows that the total interstitial surface area generated by close-packed circular features with different projected surface area depends only on the length of the plate section side and is independent of the feature radii. This geometric property was utilized for designing and testing different interstitial surface area distributions while maintaining the same total interstitial surface area at the same time.

4.1.3. The arrangement

During preliminary observations, the plates were zip-tied onto a large screen mat that was anchored to the surface of the ATS, but due to visual evidence of undesired floating regions, it was decided to introduce a perforated PVC sheet that was wrapped with the initial screen mat and was allowed to sink below the water surface of the ATS (see Figure 7).

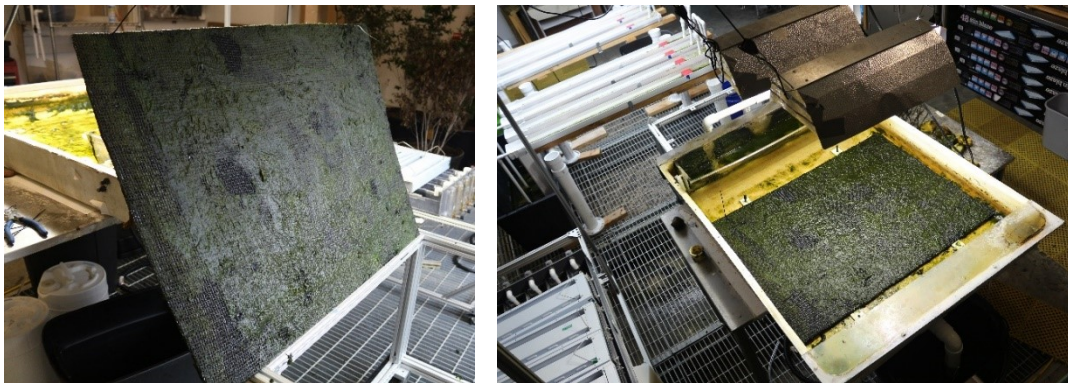


Figure 7: On the left: Screen mat wrapped around a PVC sheet. On the right: Introduction of the PVC and screen mat into the surface of the ATS.

After having the ATS acclimated to the PVC sheet, the testing plates (in an array free of trends) were mounted on it by zip-tying their overlaid mesh plastic screen contour to the PVC. The array free of trends avoided having repeated sequences of printed sections along the same column. For example, if in a column of the array (in alignment to the water

flow direction) a 25-pocket section was preceded by a 36-pocket section, such sequence happened only once in the column of the array. The PVC with the plates were both sunk below the surface of the ATS water. Improved stability of the testing plates with reduced floating was observed.



Figure 8: Randomized arrangement of the plates

The layout of the plates as shown in Figure 8 aims to decrease any possible light shading effect created (especially over the flat section) and reduce possible uneven hydrodynamic flow patterns generated by drastic changes of size on adjacent features. The latter consideration is minimized though by designing the domes with the same height. Details of the geometry generated by the features are shown in Table 2.

Table 2: Experimental treatment levels for interstitial surface area distribution

Treatment Level	Replicates	Interstitial Surface Area Distribution Level	Number of Interstitial surface area pockets	Total interstitial surface area (cm²)	Diameter of the projected dome (cm)	Height of domes (cm)
A	21	Control Surface	0	NA	NA	NA
B	21	Low	25	4.95	1.2	0.3
C	21	Medium	36	4.95	0.8	0.3
D	21	High	81	4.95	0.6	0.3

4.1.4. Biomass harvesting

Algal biomass was precisely and selectively harvested every day during seven days from the interstitial spaces in each region. The harvesting process was developed using a 100 ml Erlenmeyer flask with a two-holed rubber stopper #2. The flask worked as a collector of the harvested biomass.

A piece of plastic capillary tubing was incorporated through each hole of the stopper and worked as tube fitting. One fitting was designed to be connected to the central vacuum system of the lab, and the other to be plugged to a conical metallic tip with a 1 mm orifice at the end of it. This was used to selectively vacuum the biomass from the pockets of each section (Figure 9).

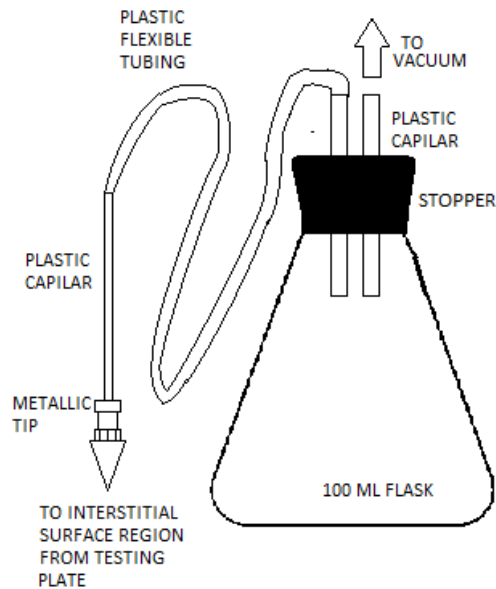


Figure 9: Schematic of the harvesting tool to capture algal biomass from interstitial spaces

Three plates were randomly selected every day for harvest. Only one plate was removed at a time to avoid air drying of the algae while on queue for harvesting. For this, the ATS was shut down and completely drained on its surface before removing the plates from the reactor. For each harvesting event, only the interstitial spaces from every section of each plate were harvested with a combination of steps which include: vacuuming (V), mechanical scraping (S), and distilled water rinsing (R). The sequence for harvesting every section was R-V-S twice (Figure 10). The biomass collected from the interstitial space of each section was stored separately in a labeled plastic 50 ml falcon tube that was filled to top with distilled water if needed.



Figure 10: The harvesting process: Vacuuming

4.1.5. Preliminary Experimentation

To support formal experimentation, the influence of the borders of the plates on the algal biomass attachment was subject to preliminary experimentation. This was addressed due to the visual identification of algal clump formations in such regions. For this, the productivity of biomass collected from the inner and the outer regions of the printed plate was measured. An extra 3D printed tooling provided precise harvesting on the desired regions. Figure 11 (Left) shows the 3D-printed square frame fitting on a section of a plate. This piece was designed to fit on each section of the plate and mask the outer regions while harvesting the inner pockets (Figure 11 -Right). The harvesting of the outer regions was done after completion of the inner ones without the mediation of the tool.

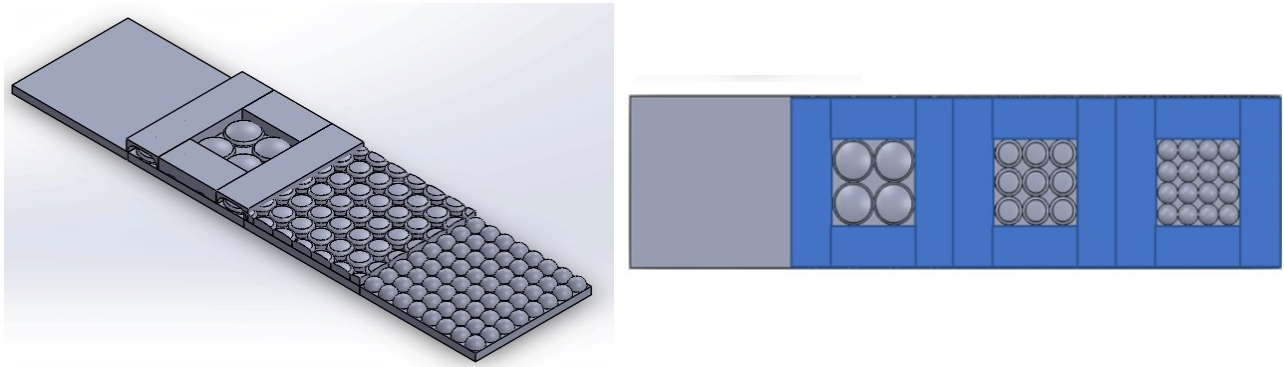


Figure 11: Evaluation of the border effect on algal biomass attachment: (Left) 3D-printed blocking tool (Right) 2D-top view of the blocking effect of the tool for harvesting purposes

4.1.5.1. Preliminary methodology for biomass determination: Biomass Oven-Drying

Since the quantification of the harvested biomass was not performed immediately right after collection, falcon tubes were used to store algae samples in a fridge at 5°C for a period of time of no more than 48 hours. When extra time for storage was needed, samples were placed into a freezer at -20° C. Retrieval of samples from the freezer was performed in 2 steps. First, the samples were replaced into the fridge to let them thaw. Second, they were placed in room temperature to proceed to the subsequent drying process.

Samples were filtered using 47 mm diameter glass microfiber filters (Whatman Cat No. 1822-047) suitable to resist high-temperature (500 °C). The filter papers used for the filtering process were pre-dried in the oven at 105°C for 24 hours and then placed in the desiccator for 24 hours. The pre-dried filter paper was weighed on a digital balance (Acculab) with a resolution of 0.0001 grams. The readings were saved under the name “Filter Paper Dry Weight (FPDW)”. Tweezers were utilized to manipulate the filters to avoid contamination through hand manipulation. Filters were then placed on a properly labeled aluminum container.

The filtration process was done with a magnetic filtering apparatus connected to a vacuum flask. The vacuum was provided by the centralized system of the building. Once all the samples were filtered they were placed in a conventional oven at 105 °C for 24 hours. When dried, the samples were removed from the oven and replaced into a desiccator for 24 hours. Finally, the filters were weighed back considering now the amount of biomass that was collected during the harvesting process from all the interstitial spaces from each section and flat one. The readings were saved under the name “Total Dry Weight (TDW)” and computed with the following approaches.

To quantify the daily biomass productivity, the biomass dry weight (DW) was first obtained by deducting the weight of the empty pre-dried filter (FPDW) from the weight of the dried algal biomass samples (TDW).

$$DW = TDW - FPDW$$

The net biomass density (NBD) was then normalized per unit area

$$\text{NBD} = \text{DW} / A$$

where A is the surface area where the algae were harvested from; in this case, the interstitial area.

Finally, the Daily Biomass Productivity (DBMP) was calculated by dividing the net biomass density by the count of cultivation days (n), (e.g., 1,2,3,4,5,6,7)

$$\text{DBMP} = \text{NBD} / n$$

A summary picture showing the sequence for the preliminary methodology from harvesting until obtaining the oven dried algal biomass estimation is shown in Figure 12.

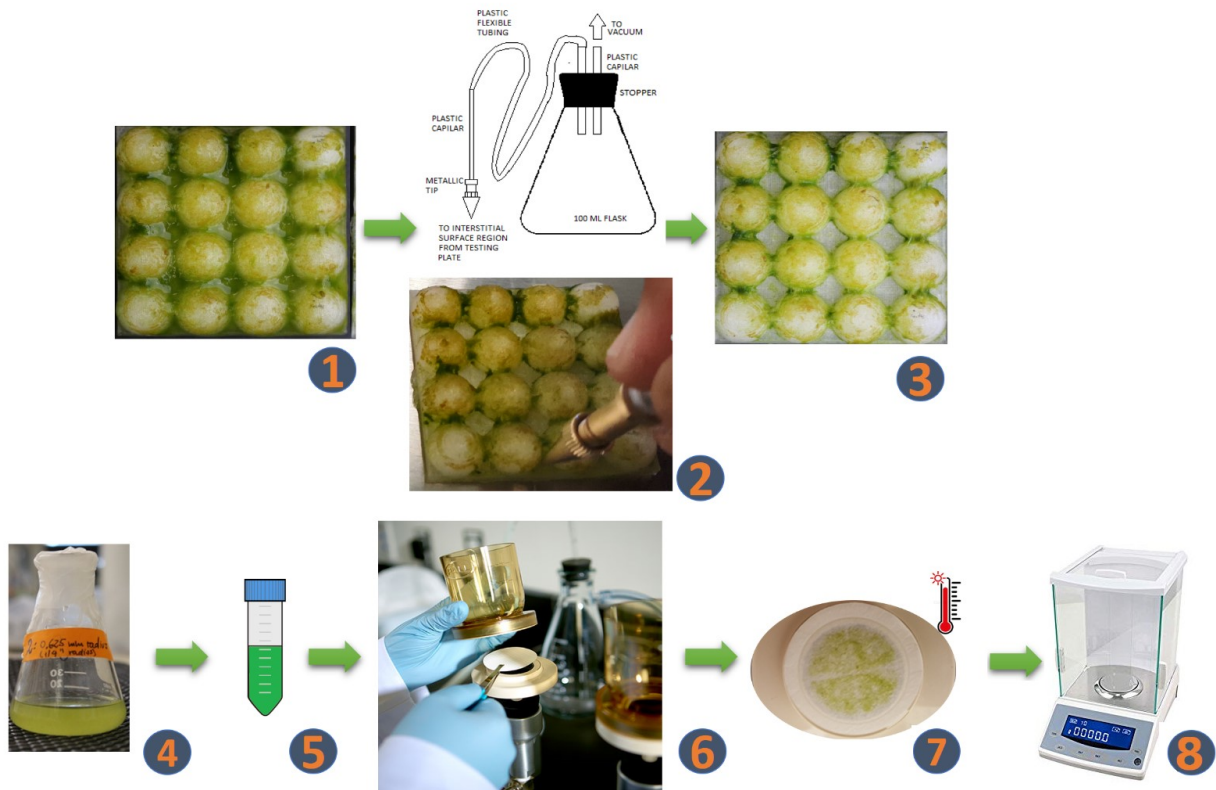


Figure 12: Summary of preliminary methodology for algal biomass estimation.
1. Raw algal samples from plates 2. Harvesting process 3. Harvested plate 4. Algal sample right after harvest 5. Algal samples for storage 6. Filtering process 7. Oven drying 8. Oven dried weight estimation

4.1.5.2. Preliminary Results

Visual differences in the amount of algae colonizing the different treatments of interstitial space distributions were identified (see Figure 13). The amount of harvested biomass available for estimation appeared to be limited though, however, during the first days of colonization.

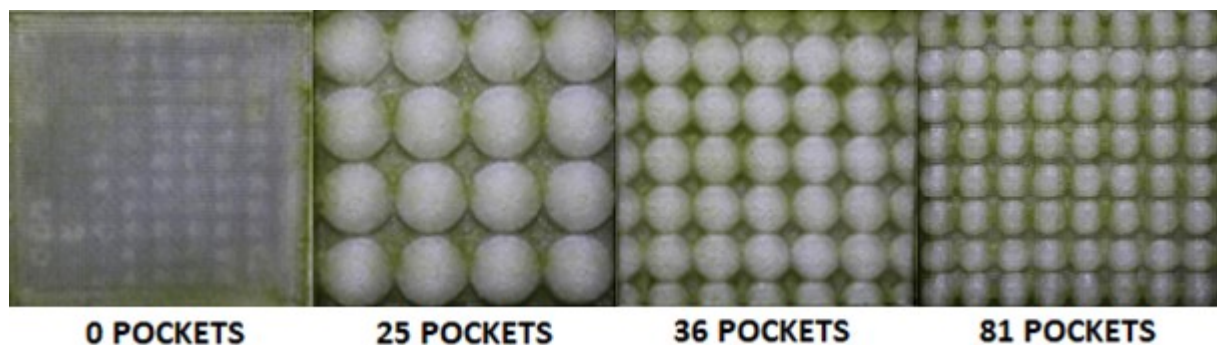


Figure 13: Different levels of algal colonization per treatment 5 days after deployment in the ATS.
(All section types at the same magnification)

The histogram on Figure 14a shows the data distribution for the estimated biomass, which revealed negative biomass estimations with the oven-drying method. These events occurred because the readings taken from the balance while weighing the algae samples retained in the filter were sometimes less than those taken when weighing solely the filter itself. This was obviously an error on the estimation. Possible reasons can be attributed to the influence of static charge that might be generated during the manipulation of the filters while weighing (Swanson & Kittelson, 2008), in addition to lack of precision in the balance.

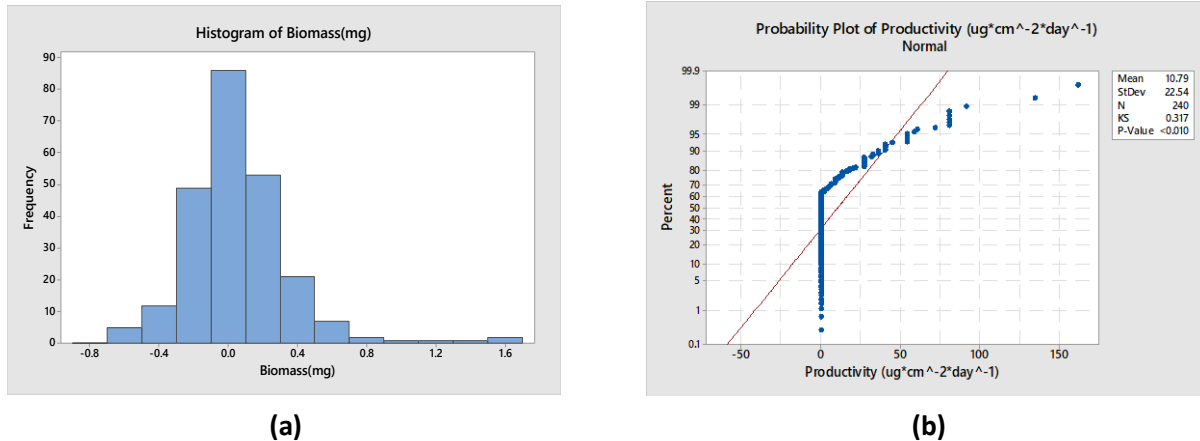


Figure 14: Outcomes from preliminary work for experiment 1. (a) Histogram of the algal biomass collection from the overall plates' interstitial pockets (b): Kolmogorov-Smirnoff Test of Normality for the Biomass Productivity collected from the overall interstitial pockets.

To deal with the presence of negative data, these values were truncated to zero and analyzed with the consideration of having a non-normal distribution as shown in Figure 14b.

A Kruskal-Wallis test was used to analyze the statistical significance of the border effect on algal biomass productivity. Such test was applied to determine whether the medians of the algal biomass productivity taken from the harvest from the inner regions of the plate section differed from the ones from the outer. Given the non-normal distribution of the preliminary data, in addition to the presence of outliers, for statistical analysis, Kruskal-Wallis test was suitable given the number of samples ($n=120$) and the 2 region types that were analyzed (inner and outer region of the section plate). Figure 15 shows the interval plot from the two region-type and Table 3 shows the p-value obtained from the statistical test, thus concluding that medians from both region types are equal ($p=0.072$).

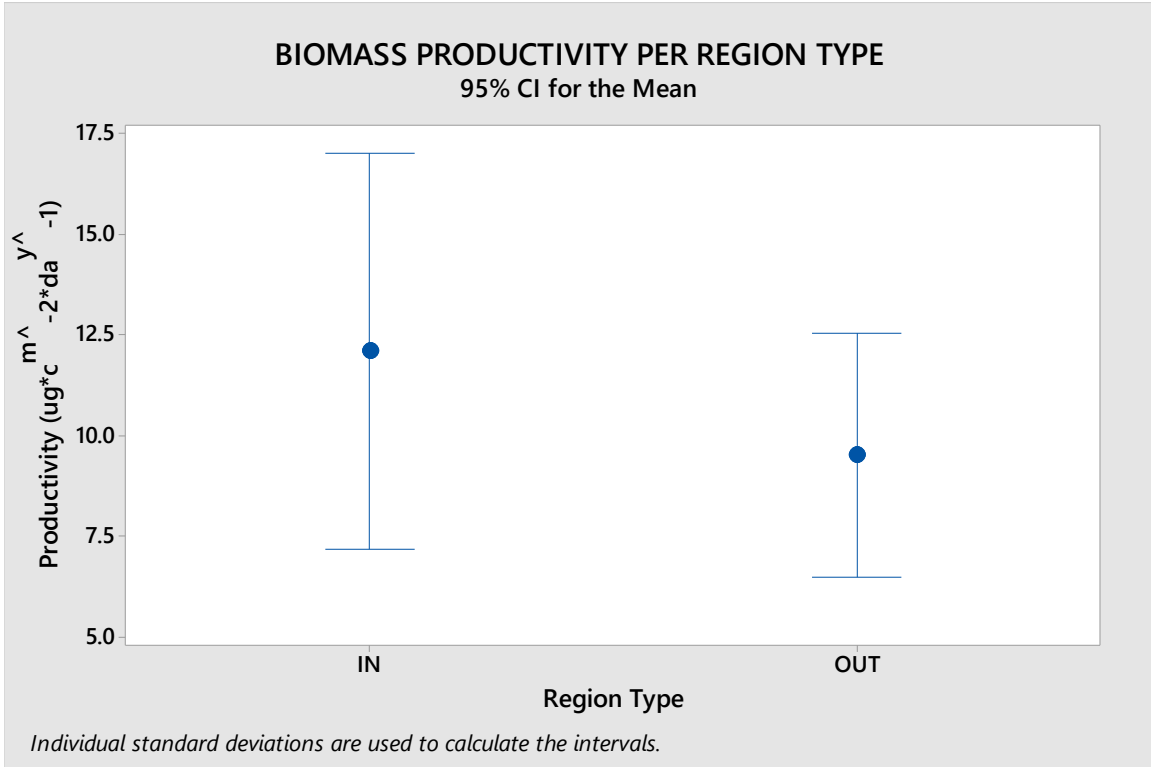


Figure 15: Biomass Productivity per region type (Inner and Outer region of the testing plate)

Table 3: Kruskal-Wallis test for border effects on biomass productivity.

Null hypothesis	H ₀ : All medians are equal		
Alternative hypothesis	H ₁ : At least one median is different		
Method	DF	H-Value	P-Value
Not adjusted for ties	1	3.23	0.072
Adjusted for ties	1	4.33	0.037

With the information obtained from preliminary results, it was decided to perform a full harvest from all the interstitial spaces with no concerns on any border effect.

4.1.6. Micro Gravimetric Method for Algal Biomass estimation

Given the lack of fidelity on the biomass estimation by oven drying, an alternative methodology was developed instead. To deal with the limited biomass available for estimation, it was determined to keep the testing plates in the ATS on hold for 5 days after deployment to allow enough algal biofilm colonization to be measurable by micro-gravimetry.

The biomass determination was performed over 7 days and included pelletizing, freeze drying and weighing the samples on a microbalance.

4.1.6.1. Pelletizing Process

Once the samples were harvested and placed in the 50 ml Falcon tubes, they were taken to the Aquatic Microbiology lab from the School of Fisheries, Aquaculture and Aquatic Sciences located in the same CASIC building at Auburn University. Samples passed through a series of centrifugation and decanting processes until reaching a pelletized algal sample capable to fit in a 0.2 ml PCR tube. Prior to this, the empty 0.2 ml PCR tubes were labeled, pre-dried in a desiccator glass chamber for 24 hours and weighed with a microbalance (Sartorius TM, 3000 mg range, resolution: 0.001 mg) located at Funchess Hall from the Crop, Soil and Environmental Sciences department at Auburn University. The weights were registered for further biomass estimation. The pelletizing protocol is described as follows.

1. Centrifugation of the sample in 50 mL Falcon tube at 5000 RPM using Centrifuge Eppendorf 5804R for 15 minutes.
2. Decanting and disposal of the supernatant generated from step 1.
3. Transferring of the pelletized sample from the 50 mL tube to 2 mL PCR tube.
4. Centrifugation of the sample contained in the 2 mL PCR tube using micro Centrifuge Eppendorf 5415 D at 13000 RPM for 10 minutes.
5. Decanting and disposal of the supernatant generated from step 4.
6. Transferring of the pelletized sample from the 2 mL tube to a 0.2 mL PCR tube.
7. Centrifugation of the sample contained in into the 0.2 mL PCR tube using micro Centrifuge Eppendorf 5415 D (using the corresponding adaptors for the tubes) at 13000 RPM for 10 minutes.
8. Once finished with the process, the tubes were kept into a PCR rack inside a box that was stored at 5 °C

Figure 16 shows the aspect of algal samples after being pelletized in a 2 mL and 0.2 mL PCR tube. The picture also corresponds to preliminary harvest trials until being able to determine the optimal first day of harvest for reproducible algal biomass quantification.

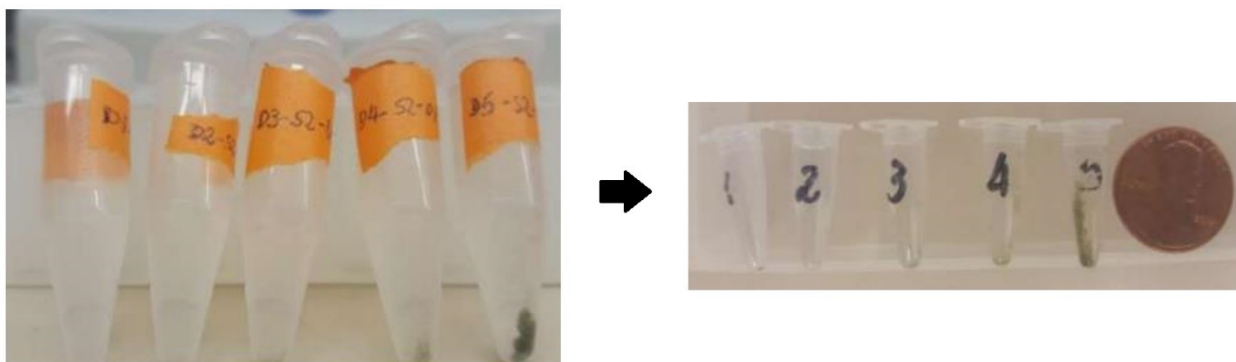


Figure 16: 2 mL and 0.2 mL pelletized algal samples.
Tubes arranged from left to right by period of cultivation (1,2,3,4,5 days)

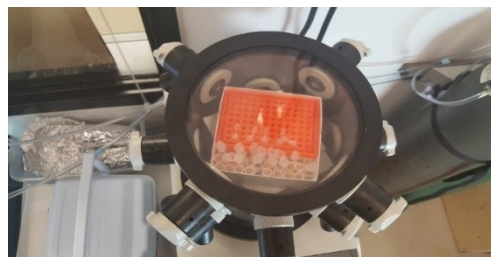
4.1.6.2. Freeze drying process

After completion of the pelletizing process, the samples were prepared for the subsequent freeze-drying process. For this, the 0.2 ml tubes with the algal samples were removed from the freezer, uncapped and parafilm on top. A small hole was perforated in the parafilm to allow moisture to escape. Sample tubes were stored in a rack inside a subzero freezer from the Aquatic Microbiology lab at -80°C for 24 hours. The following day, samples were placed into a cooler for freeze drying.

The freeze dryer (Labconco™, Figure 17a) was located at the Forest Product Development Center at Auburn University. Prior to freeze drying, samples were kept on hold (15 minutes) in a subzero freezer at -80°C until freeze dryer was set and ready for operation. Once the desired temperature was reached, samples were placed into the chamber (see Figure 17b) and the vacuum process was initiated.



(a)



(b)

Figure 17: Lyophilization system for algal freeze drying (capacity: 1.5 L, vacuum: 0.014 mbar, temperature: -50°C)

Samples were left under freeze-drying conditions overnight and after 18 hours they were withdrawn, put into a carrying cooler for transportation storage and taken back to CASIC building to store them at 5°C.

4.1.6.3. Micro-weighing Process

To determine the mass of the freeze-dried pellets, the samples were withdrawn from the fridge and stored in the cooler and transported to Funchess Hall. To let the samples reach room temperature, they were left on hold for 30 minutes and then weighed in the microbalance (see Figure 18). The weights of the 0.2 mL tube were registered and respectively subtracted from the previous weights when empty.



Figure 18: Microbalance for algal biomass determination. (range: 3 mg., resolution: 1 ug)

To summarize, a total of three runs of the following protocol were performed. An illustration of this workflow is shown in Figure 19.

1. 3D-printed fabrication of 21 plates containing 4 treatment sections.
2. Zip-tying of the plates on the surface of the PVC sheet folded with screen mat with algal biofilm
3. Pre-Micro-weighing of 84 0.2 mL-PCR tubes pre-labeled and pre-dried.
4. Deployment of the plates in the ATS (day 0)
5. Removal, harvest, and collection of biomass from the first three plates into a 50-mL falcon tube fully filled with distilled water 5 days after the deployment.
6. Pelletizing of the harvested algae samples.
7. Daily harvest of 3 plates until completing the removal of all the plates.
8. Pelletizing harvested samples.
9. Parafilming the 84 0.2-mL PCR tubes with algal samples.
10. Freezing samples at -80°C .
11. Freeze drying.
12. Storage of samples at 5°C (dark conditions)

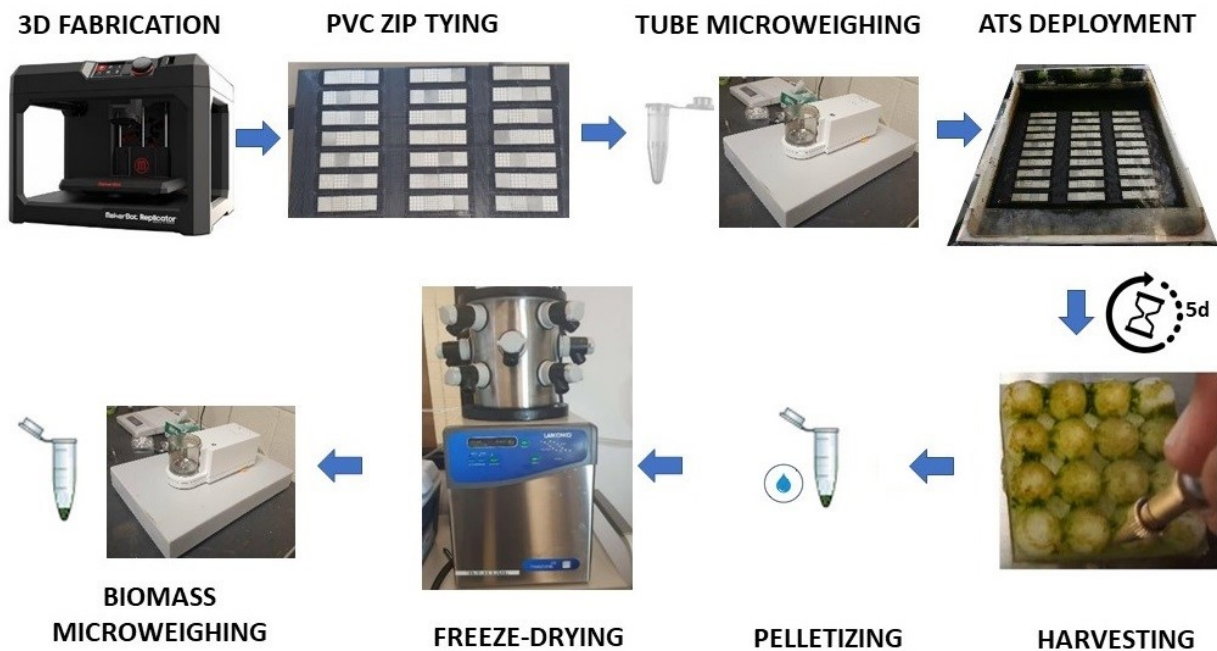


Figure 19: Illustration of protocol for Experiment 1

4.2. Results

The effect of the different interstitial surface area distributions on the substratum for algal turfs was evaluated based on the algal biomass density in the three treatments in relation to that in the control (flat surface with no pockets), at each harvest process. The estimated biomass density was based on the 7 days of harvest corresponding to days 5 to 11 of the actual cultivation process. Figure 20 shows the aspect of the 3D-printed sections between days 5 and 9 of algal colonization.

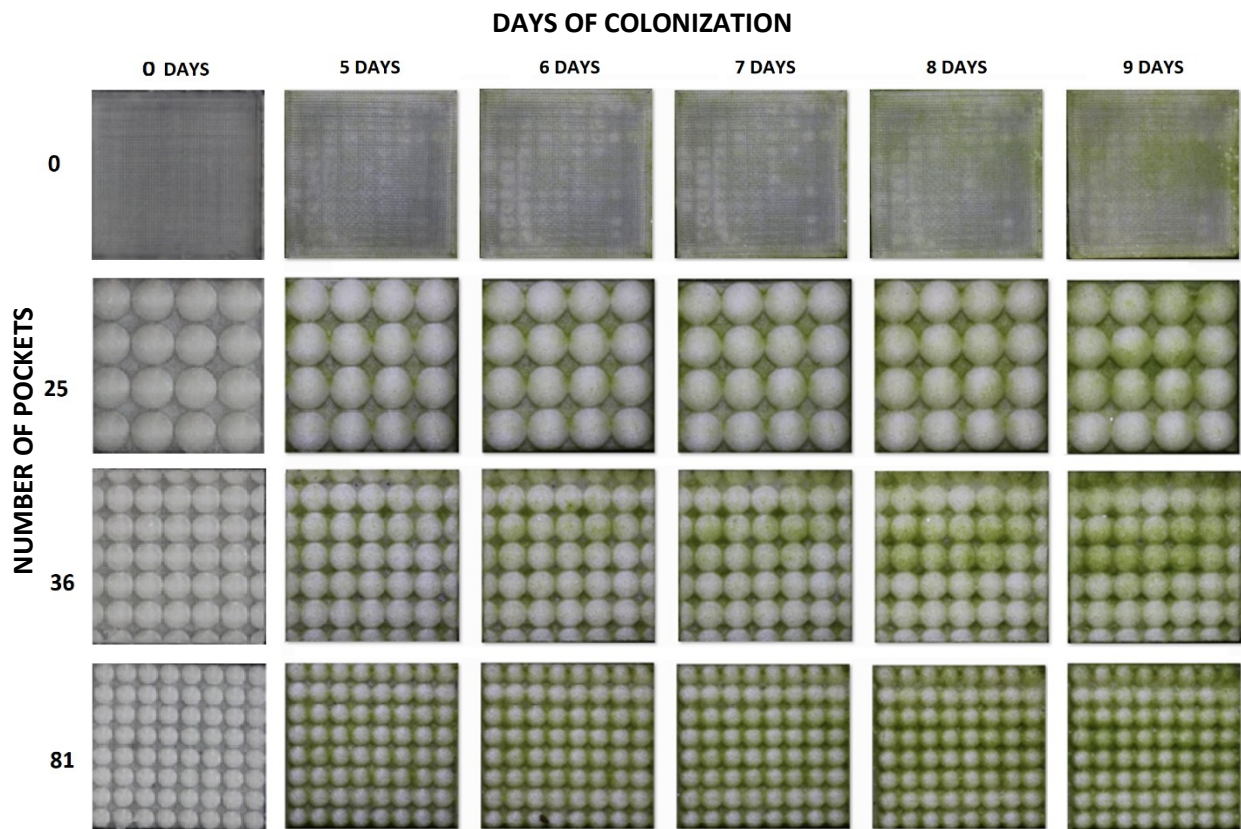


Figure 20: 3D printed plates between 5 and 9 days of algal colonization

The results of the 3 replicated runs were pooled and corresponded to normal distributed populations based on Kolmogorov-Smirnov test for normality ($p > 0.05$). When Levene's test failed for equal variances, the Kruskal-Wallis test was used for comparing medians. The significance per harvest was analyzed using a one-way ANOVA. The grouping information using Tukey Test at a 95% confidence is shown in Table 4.

Table 4: Mean values and standard deviations (in parentheses) of algal biomass densities (in mg/cm²) of each treatment per harvest, and p values from ANOVA between treatments for each harvest.

Harvest number (Day of cultivation) - Treatment -	1 (Day 5)	2 (Day 6)	3 (Day 7)	4 (Day 8)	5 (Day 9)	6 (Day 10)	7 (Day 11)
0 pockets	0.1340 (0.0318) ^b	0.1858 (0.0528) ^b	0.2449 (0.0624) ^b	0.3686 (0.1118) ^b	0.3631 (0.0961)	0.4141 (0.0964)	0.4864 (0.1332) ^b
25 pockets	0.3104 (0.1228) ^a	0.4999 (0.2497) ^a	0.5524 (0.2163) ^a	0.8010 (0.3880) ^a	0.7767 (0.2864)	0.8430 (0.3700)	0.9520 (0.3290) ^a
36 pockets	0.3781 (0.1370) ^a	0.4658 (0.1784) ^a	0.5772 (0.1555) ^a	0.6237 (0.1582) ^{ab}	0.7651 (0.2217)	0.7905 (0.2417)	0.8204 (0.2794) ^a
81 pockets	0.3597 (0.1011) ^a	0.6800 (0.1658) ^a	0.7391 (0.2342) ^a	0.9110 (0.3580) ^a	1.0990 (0.4110)	1.1950 (0.4470)	1.0479 (0.2171) ^a
<i>p</i> (ANOVA)	0.000	0.000	0.000	0.002	-	-	0.000
<i>p</i> (Normality test Kolmogorov-Smirnov)	>0.150	>0.150	>0.150	>0.150	0.107	0.096	0.085
<i>p</i> (Equal Variances Levene's test)	0.143	0.232	0.084	0.082	0.019*	0.023*	0.205
<i>p</i> (Kruskal-Wallis)	-	-	-	-	0	0.001	-

* $p \leq 0.05$ indicates non-normal distribution or non-equal variances

Treatments with the same symbol are not significantly different from each other, from Tukey's multiple comparison test, at a $p < 0.05$

4.3. Discussion

Considering that the colonizing algal cells into the interstitial surface are in continuous growth, the biomass density plot displayed on Figure 21 is proposed that can be fitted into a logistic model (Tsoularis & Wallace, 2002).

A logistic model of growth is characterized by the following expression:

$$S(t) = \frac{C}{1 + Ae^{-kt}}$$

where C is the carrying capacity, k is the growth rate and A is a constant to adjust the inflection point of the curve. The growth rate on this model changes in time, but during the linear region of the curve, it expresses its maximum value (when it reaches half of its carrying capacity). The carrying capacity instead is that boundary value up to which algal biomass can no longer keep growing.

Logistic algal growth models have been implemented already to explain the growth of periphyton algae (Rodriguez, 1987). For this reason and based on the regression coefficients obtained it is proposed that the data generated from current experimentation can be fitted to a logistic curve. The proposed logistic growth curves for each treatment are presented in Figure 21. The selection of the carrying capacity parameter shown in Table 5 was based on the maximum biomass density obtained by each treatment.

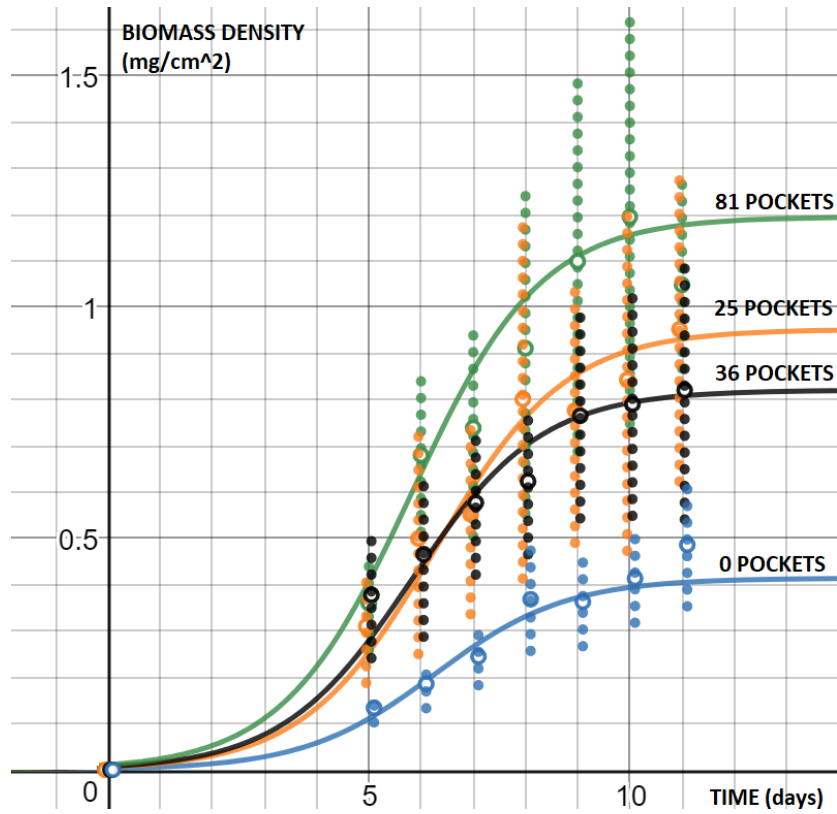


Figure 21: Logistic curve fit *Biomass Density* vs *Time* for the pooled 3 runs results

Table 5: Logistics curve fitting for biomass density per day of cultivation

Treatment	Logistic Function	Carrying Capacity (mg / cm ²)	Growth Rate (days ⁻¹)	R ²
0 Pockets	$S(t) = \frac{0.4141}{1 + 150e^{-0.8t}}$	0.4141	0.800	0.9486
25 Pockets	$S(t) = \frac{0.952}{1 + 150e^{-0.8t}}$	0.952	0.800	0.9654
36 Pockets	$S(t) = \frac{0.8204}{1 + 110e^{-0.808t}}$	0.8204	0.808	0.9680
81 Pockets	$S(t) = \frac{1.195}{1 + 110e^{-0.808t}}$	1.195	0.808	0.9571

Within the first stages of the growth curve, corresponding to the first 5 days of cultivation, the algal biomass was not able to be quantified given the sensitivity constraints of the measuring devices; however, the linear and the final phases of growth are quite distinguishable with the proposed growth model presented in Figure 21.

To address the suitability of the modeling approach, data from day 5 to 8 of algal cultivation were fitted to a linear curve as same as for days 9 to 11, but separately. Figure 22 and Figure 23 show the linear fitting for both pieces of data. Table 6 and Table 7 show the regression coefficients and the slopes obtained for such regions.

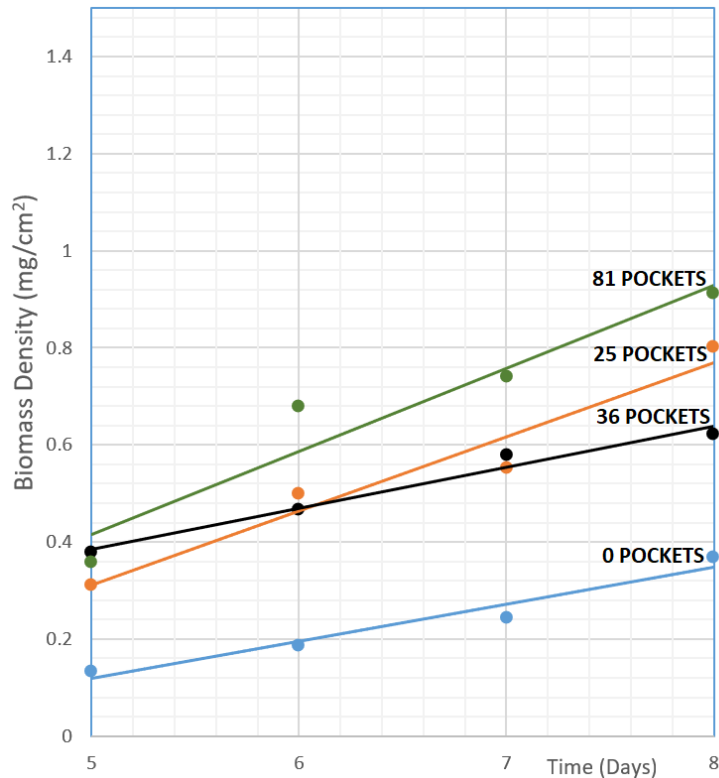


Figure 22: Linear region of the fitted logistic curve

Table 6: Linear model, growth rate and regression coefficient for the linear region of algal biomass density growth.

	Linear fit	Slope [mg/cm²/day]	R²
0 pockets	$y = 0.0763x - 0.2626$	0.0763	0.9523
25 pockets	$y = 0.1524x - 0.4499$	0.1524	0.9476
36 pockets	$y = 0.0848x - 0.0401$	0.0848	0.9778
81 pockets	$y = 0.1713x - 0.441$	0.1713	0.9215

From the linear regression analysis with the data from the first four harvest processes, it was observed that given the regression coefficients, the algal biomass density did fit a linear curve and corresponded to the linear region of the logistic curve. The slopes from Table 6 represents an approximation of the algal biomass density growth rate for each treatment during that time frame. Since the linear region of the logistic curve contains the inflection point of the curve at which the largest growth rate occurs, the calculated slope from the linear approach must be approximate to the maximum growth rate of each treatment.

The second piece of the growth analysis was based on the last three days of harvest (days 9 to 11). The best curve fit is shown in Figure 23.

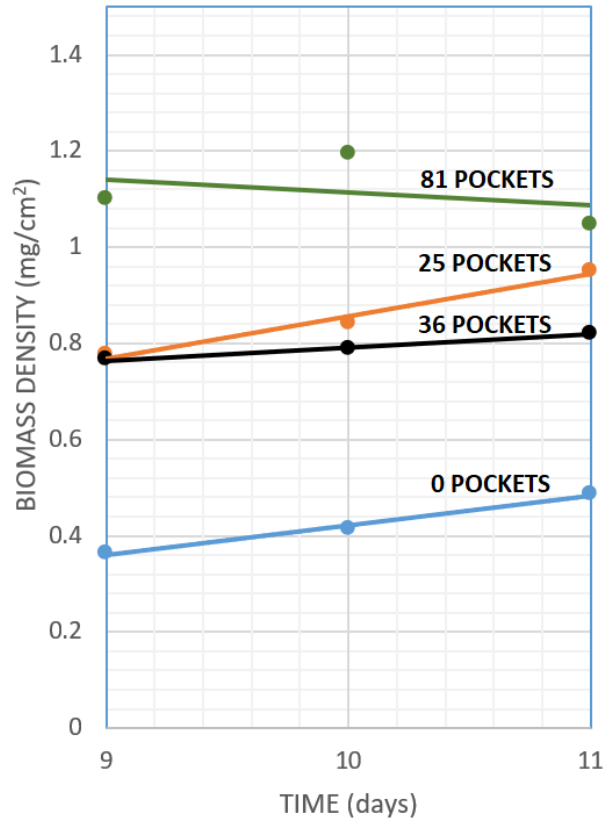


Figure 23: Final region of the fitted logistic curve

In a similar way as in the earlier analysis, the slope was estimated for such data. The results are shown in Table 7.

Table 7: Linear model, growth rate and regression coefficient for the final region of algal biomass density growth.

	Linear fit	Slope [mg/cm²/day]	R²
0 pockets	$y = 0.0617x - 0.1953$	0.0617	0.9902
25 pockets	$y = 0.0876x - 0.0193$	0.0876	0.9806
36 pockets	$y = 0.0276x - 0.5155$	0.0276	0.9978
81 pockets	$y = -0.0255x + 1.3695$	-0.0255	0.117

Table 7 shows the 81-pocket treatment with a low regression coefficient. Based on the negative slope, it can be hypothesized that by day 11 of cultivation this treatment already reached its maximum biomass density. Based on the logistic regression coefficient obtained for this treatment ($R^2=0.92$), it appears that the selection of the maximum biomass density as the carrying capacity parameter for the proposed logistic regression provides a good curve fit.

Treatments with 25 and 36 pockets showed a decrease on their slopes from the earlier analysis and by judging on the behavior of the 81-pocket treatment, it can be hypothesized that they were close to reaching a saturation on their growth. For this reason, the proposed logistic growth model for the 25 and the 36 pocket treatments was calibrated based on their expected maximum biomass density to happen on the 11th day of cultivation. The logistic regression coefficients obtained for these treatments ($R^2=0.97$) provides evidence of a good curve fit as well as support to the criteria for selecting the maximum biomass density as the carrying capacity.

To maintain the consistency with the previous treatments on the proposed growth model, the carrying capacity for the treatment with 0 pockets was set based on the maximum biomass density achieved by the treatment. Based on the good logistic regression coefficient ($R^2=0.95$), it appears that the maximum biomass density is close to the value obtained on day 11 of colonization.

4.3.1. Hydrodynamic Analysis

It is expected that early cultivation relies on the formation of *quiescent zones* near the substratum. These zones are thought to disrupting the turbulent regime of the overlying flow at the boundary layer due to the interaction between the topographic features on the substratum and the consequent changes on the hydrodynamics at the boundary layer. To investigate these arguments, a Computer Fluid Dynamic (CFD) analysis was performed based on the environmental conditions of this project. The CFD analysis aimed to visualize the hydrodynamic behaviors near to the 3D-printed plates. The parameters that are subject of discussion are the average shear stress at the surface of the plate and through the interstitial spaces, the water velocity profile with emphasis at the boundary layer of the pockets, and finally the potential effects of the water velocity on the forces present inside the pockets.

For the CFD analysis, Solidworks-Flow, a toolbox from Solidworks® (Dassault Systèmes SolidWorks Corp., Waltham, Massachusetts) was set up based on the following assumptions that simplify the conditions of the ATS:

- Water velocity: 0.042 m/s (Given the 45 L/min of water flow passing through a cross-sectional area of 0.95 m. width and 0.02 m. depth at the ATS).
- Flow type conditions: simultaneously laminar and turbulent (Given the surge generated by the tipping bucket).
- Atmospheric Pressure: 101,325 Pa
- Temperature: 25°C
- Viscosity: $\eta = 8.9E-4$ [Pa.s]

The computational domain was set following the dimensions of the actual plate and leaving some extra domain on the y-axis for the analysis of the boundary layer as shown in Figure 24.

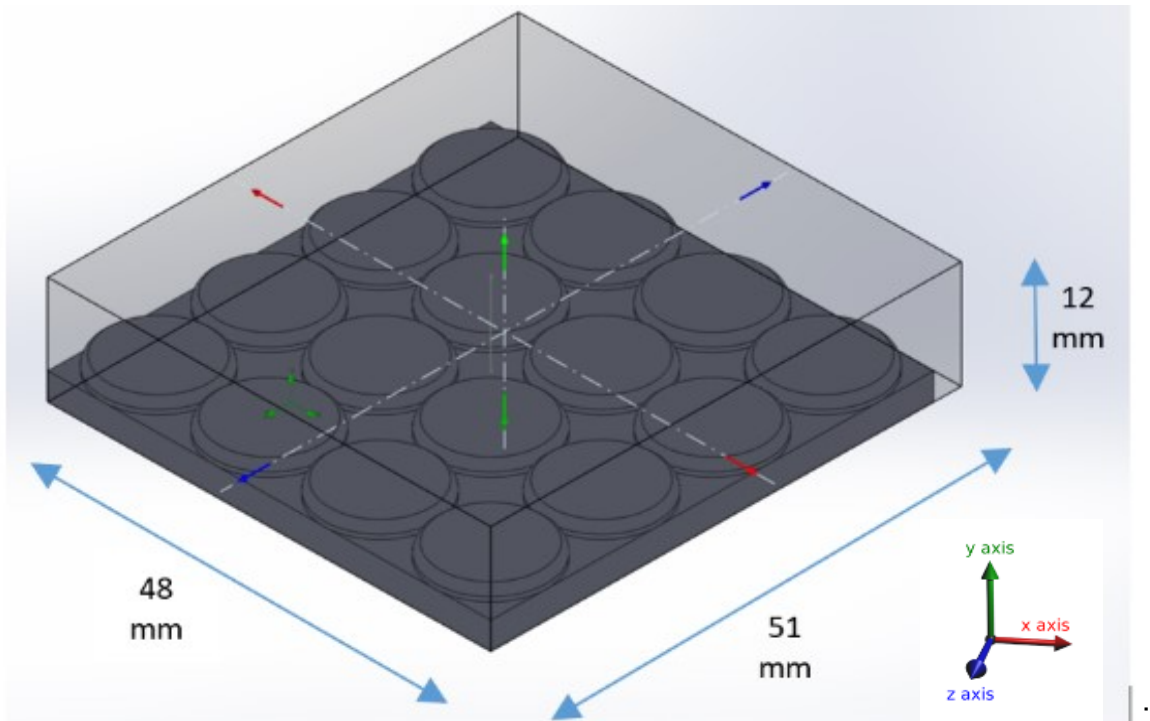


Figure 24: Computational Domain for the 3D-printed part imported into Solidworks-Flow

Solidworks Flow Simulation is based on the use of Cartesian-based meshes (Solidworks, 2018). For the series of simulations run on this chapter, the following divisions per axis were set: N_x : 48, N_y : 120, N_z : 53.

4.3.1.1. Average Shear Stress Analysis

Solidworks-Flow allowed to visualize and compare the changes in the average shear stress produced by the water flow both at the surface of the features and through the interior of the interstitial spaces. Figure 25 shows the distribution of the shear stress over the whole testing plates. The gradient in colors shows the reduction of the shear stress at the surface of the interstitial pockets (colored in blue) in contrast to the higher shear stress at the hills of the features (colored in red).

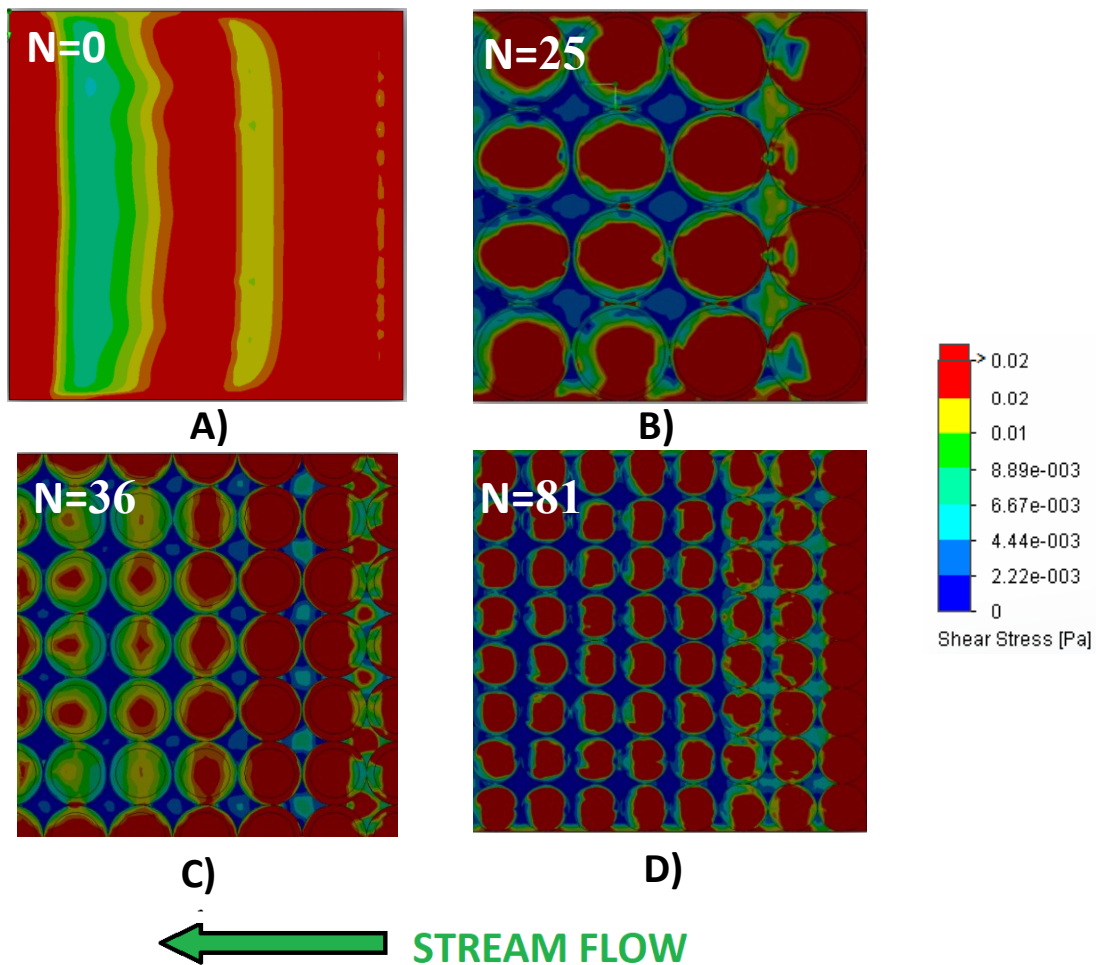


Figure 25: Distribution of the shear stress acting over the whole testing plate

Figure 26 plots a summary of the estimations on the Average Shear Stress considering both: the whole section surface area, including the printed features (blue bars) and only the interstitial surface area (orange bars).

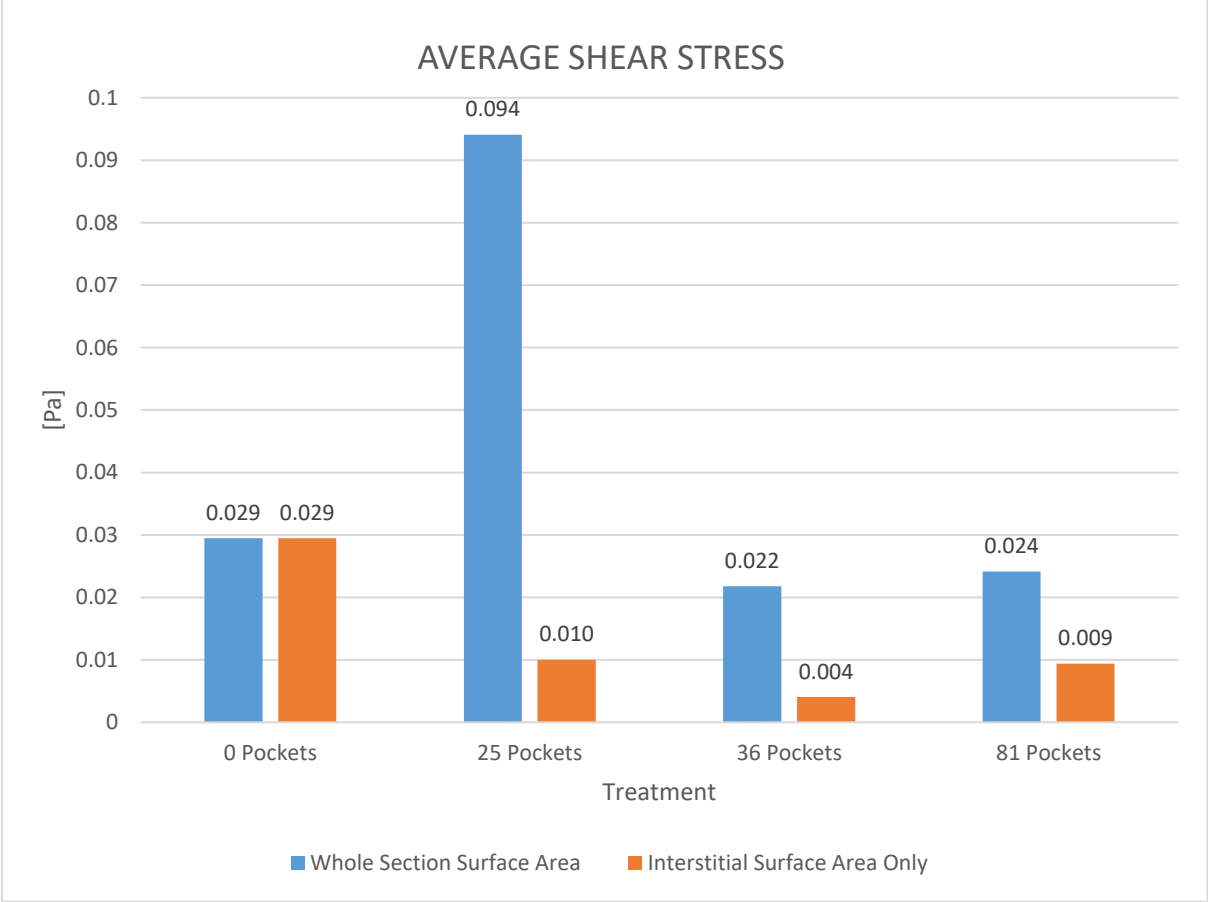


Figure 26: Average Shear Stress at the surface of the 3D-printed plates.

It is visualized that the 25-pocket treatment reaches the highest average shear stress (even more than the flat surface with no pockets) at the estimation considering the whole section.

With the generation of interstitial areas, the reduction of the average shear stress is evident over the surfaces, especially on the 25-pocket treatment. The greatest decrease in the average shear forces is experienced by the 25-pocket treatment dropping from 0.094 [Pa] to 0.010 [Pa], an 89 % reduction. A lower impact is seen on the 36-pocket treatment, where the average shear stress changed from 0.022 [Pa] to 0.004 [Pa], an 82% percent reduction. Finally, the 81-pocket treatment changed from 0.024 [Pa] to 0.009 [Pa], a 62.5% reduction in the average shear stress. The flat surface shear stress keeps the same performance as estimated earlier due to lack of pockets.

The reduction in the average shear forces at the interstitial surfaces correlates with the results of the experiment. Figure 27, on the top, shows the initial aspect of the colonized plates after being kept 5 days on hold prior to the start of the harvesting process. The comparison against the simulated shear stress shown on the bottom evidence the match between the predominantly green areas on the actual interstitial algal colonization and the regions with lower average shear forces (blue regions) from the CFD simulation. This suggests that those treatments with lower average shear stress at the surface of the substratum yield more starting algal density and hence, more algal density over time.

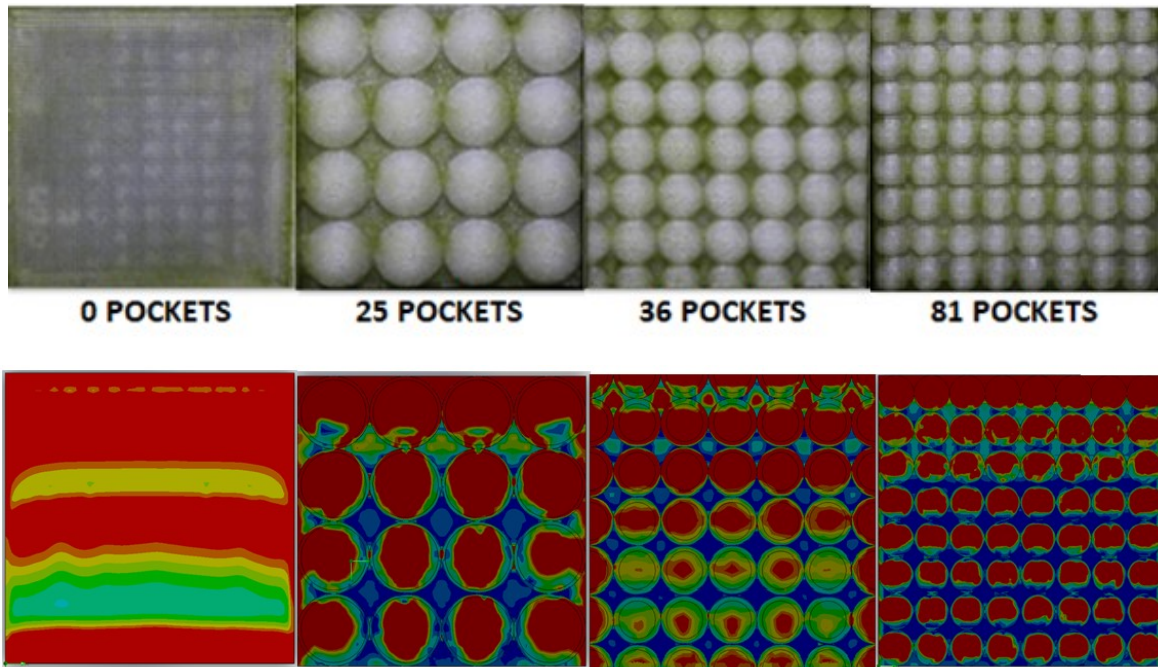


Figure 27: Visual correlation between the simulated average shear stress (bottom) and the actual starting algal density (top). *Plate oriented downstream*

The CFD simulator also shows reductions on the average shear stress once water approaches the central regions of the plate. This fact can be observed with the aid of the daily visual records that were taken by photography during the colonization process. Figure 28 shows the tendency of the plates to start the development of the algal biofilm at its center (dismissing the edge effect), just where the simulator shows reductions on the shear stress as well. This fact is also in agreement with the previous statement related to the higher algal density yields on regions with lower average shear stress.

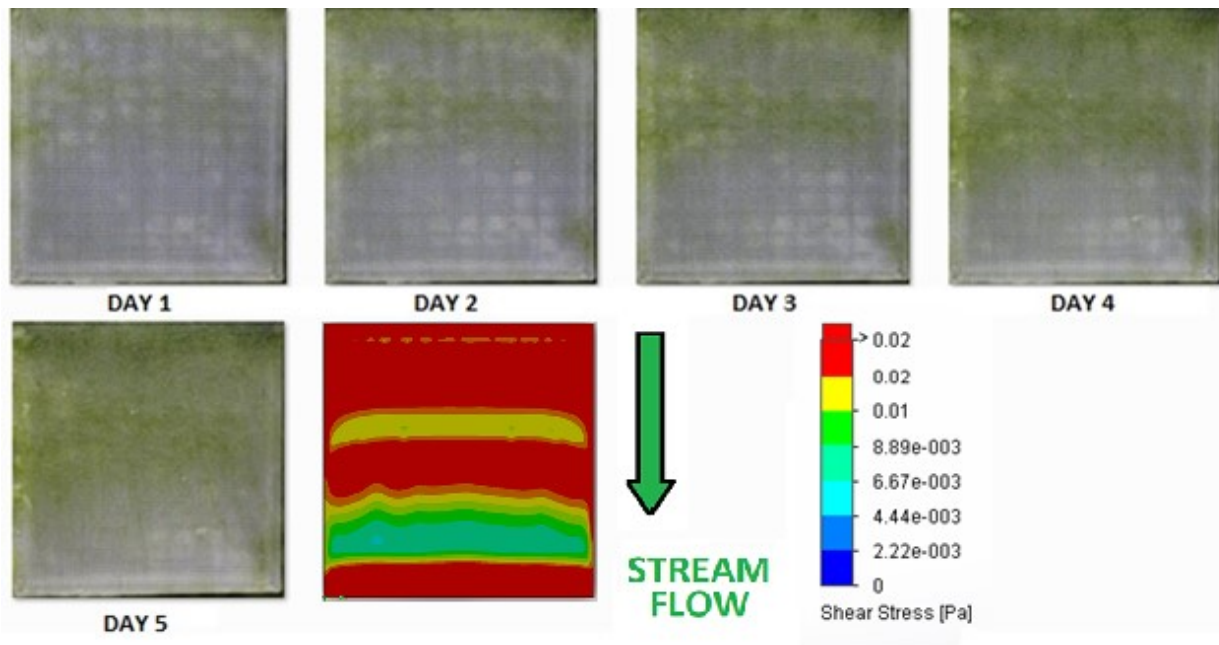


Figure 28: Algal biofilm development starting close to the center of the plate section. Picture corresponds to a sequence of snapshots taken during the second run of this project of a plate located on the first row/third column downstream

4.3.1.2. Velocity Profile Analysis

Solidworks-Flow was used to visualize the changes in the velocity vectors either in their amplitude or in their direction.

The 0-pocket treatment shows uniformity in the direction of the water flow velocities when passing through its surface even on the upstream border where the water velocity slightly increases in its magnitude (see Figure 29).

Figure 30, Figure 31 and Figure 32 show the water velocity patterns of the treatments with the generated interstitial spaces on it. The changes in the direction of the water velocity over the surface of the interstitial spaces are observed. This switch in the direction flow is caused by the presence of vorticity inside the pockets, as shown in Figure 33.

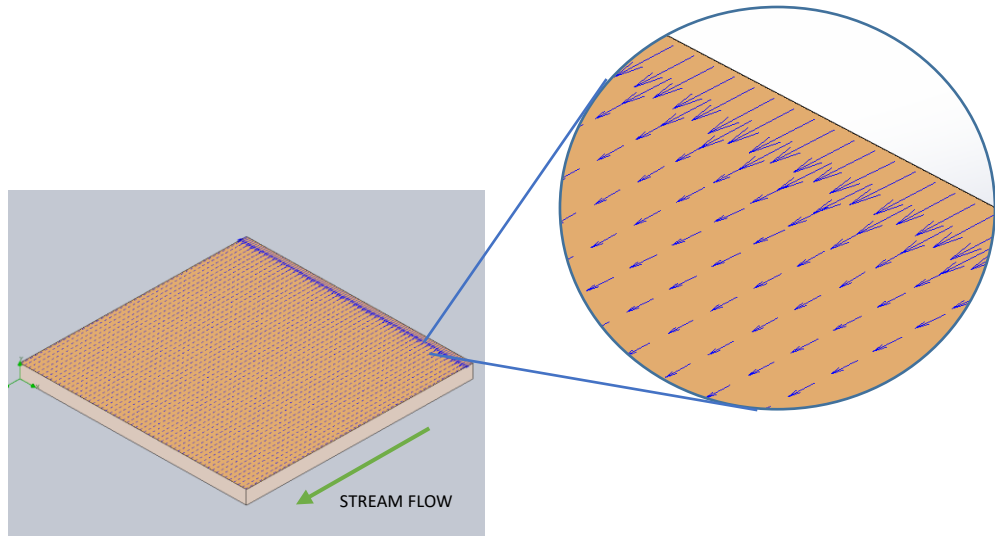


Figure 29: Water velocity vectors on the 0-pocket treatment

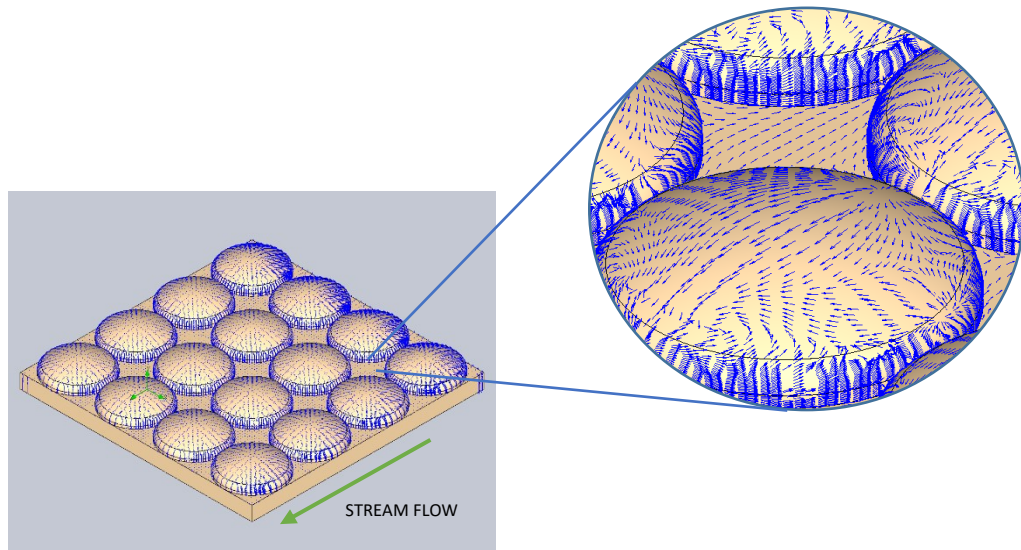


Figure 30: Water velocity vectors on the 25-pocket treatment

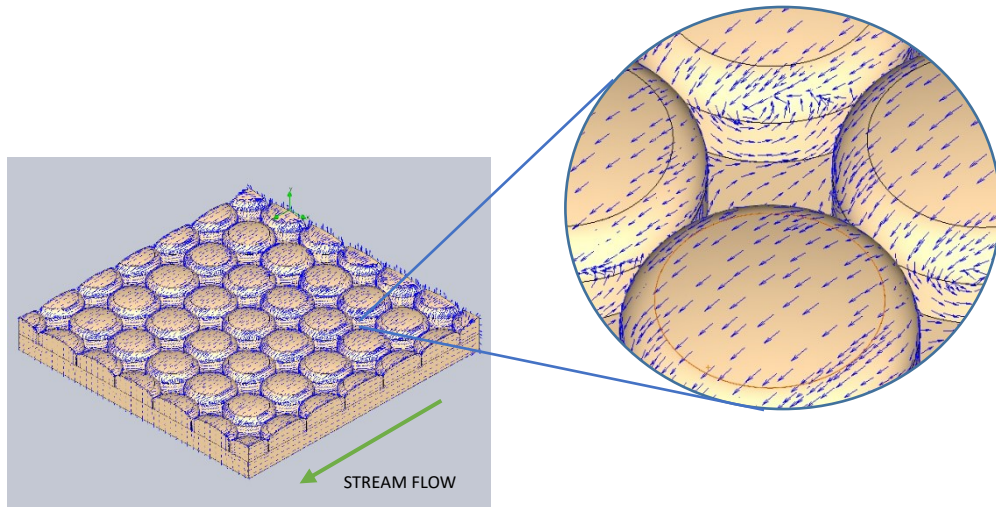


Figure 31: Water velocity vectors on the 36-pocket treatment

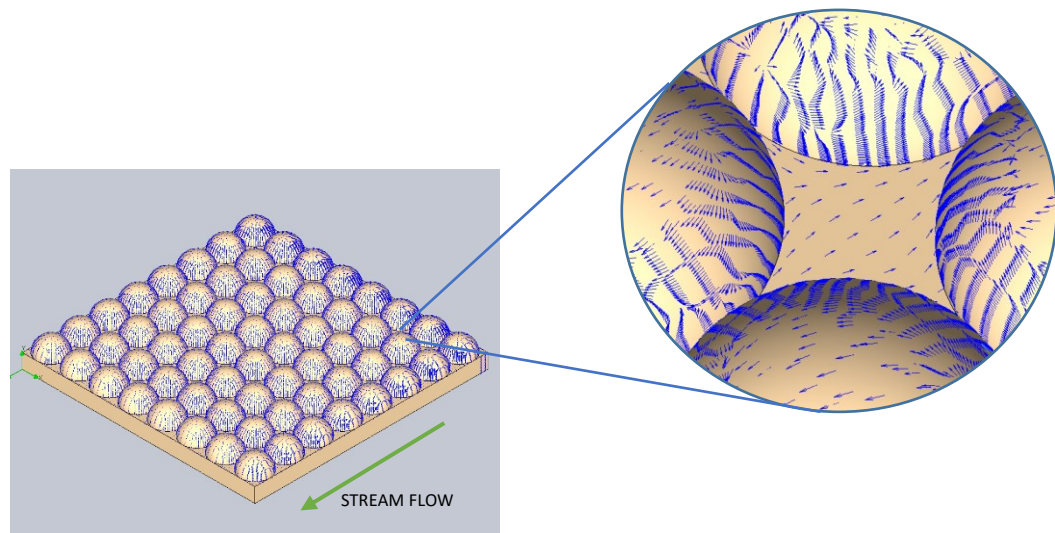


Figure 32: Water velocity vectors on the 81-pocket treatment

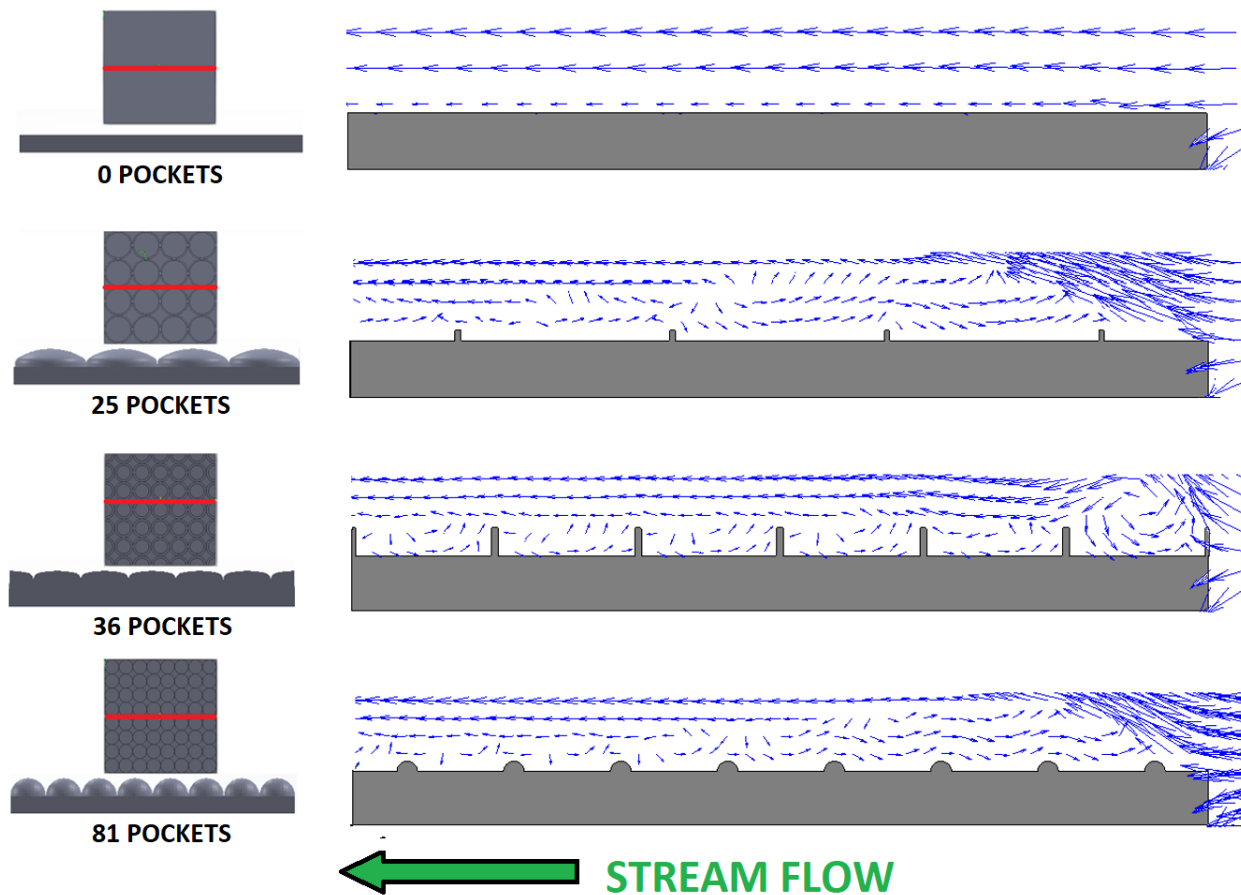


Figure 33: Vorticity along the treatments

The vorticity generation shown on Figure 33 corresponds to a cross-sectional view normal to the flat surface of the plates (coincident to the red line drawn on the top view of the plates included in the same figure). The protrusions included in the same figure are indicators of where the interstitial pocket starts and ends.

Based on these observations, it is likely that vortex generation in the interior of the interstitial pockets is a hydrodynamic factor that results in larger algal colonization rates (2-3 times according to the results) on day 5 of cultivation in comparison to the treatment with no pockets. The change in the direction of the velocity vectors provides evidence for

the role of these quiescent zones supporting algal biofilm formation. In fact, the pockets generated in this project can be considered as the microzones at the liquid-solid interface whose environmental conditions differ from the surrounding aquatic environment (Nikitin, 1973).

4.3.1.3. Velocity Boundary Layer Analysis

To get the velocity profile at the boundary layer from all treatments, 100 velocity measures were obtained from Solidworks-Flow along a 9 mm-reference-line (shown on red at the 3D-view of a plate in Figure 34 and drawn on all treatments from the floor of a random pocket for all four testing models). The blue dotted line in Figure 34 works as a reference for the maximum height of the features (3 mm height).

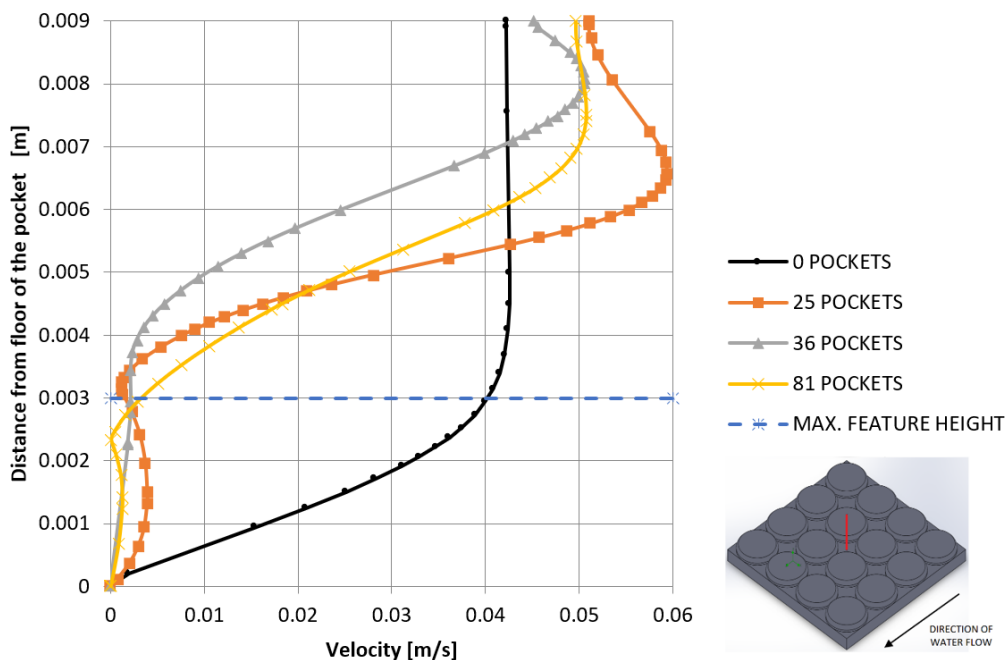


Figure 34: Boundary Layer Profile along treatments

With the data generated by Solidworks-Flow, the best curve fit was obtained for each treatment. This information is used in the next sections to model inherent hydrodynamic forces. Table 8 shows the model approach for the water velocity at the boundary layer up to 3 mm above the interstitial pockets. The R² achieved on the approach is included.

Table 8: Best curve fit for Boundary Layer Characterization

Treatment	Model approach	Equation	R²
0 Pockets	4 th order polynomy	$y = 5 \times 10^8 X^4 - 4 \times 10^6 X^3 + 8194.7 X^2 + 12.242X - 0.0004$	0.9999
25 Pockets	4 th order polynomy	$y = -2 \times 10^8 X^4 + 1 \times 10^6 X^3 - 4704.5 X^2 + 7.2002X - 2 \times 10^{-5}$	0.9999
36 Pocket	Linear model	$y = 0.7866X + 6E-05$	0.9927
81 Pockets	6 th order polynomy	$y = -4 \times 10^{14} X^6 + 3 \times 10^{12} X^5 - 1 \times 10^{10} X^4 + 2 \times 10^7 X^3 - 11281 X^2 + 4.1641 X - 9 \times 10^{-5}$	0.9811

Figure 35 complements the information on Figure 34 but emphasizes the order of magnitude of the velocity at the boundary layer for each treatment. The treatment for 0 pockets in most of the locations remains an order of magnitude greater than the other three treatments further from the floor. At the same time, all the treatments with pockets are clustered, keeping approximately the same order of magnitude on their velocity

profiles. The discontinuity of the plot at the beginning of the curves is due to the negative values of the velocity generated by the model approach.

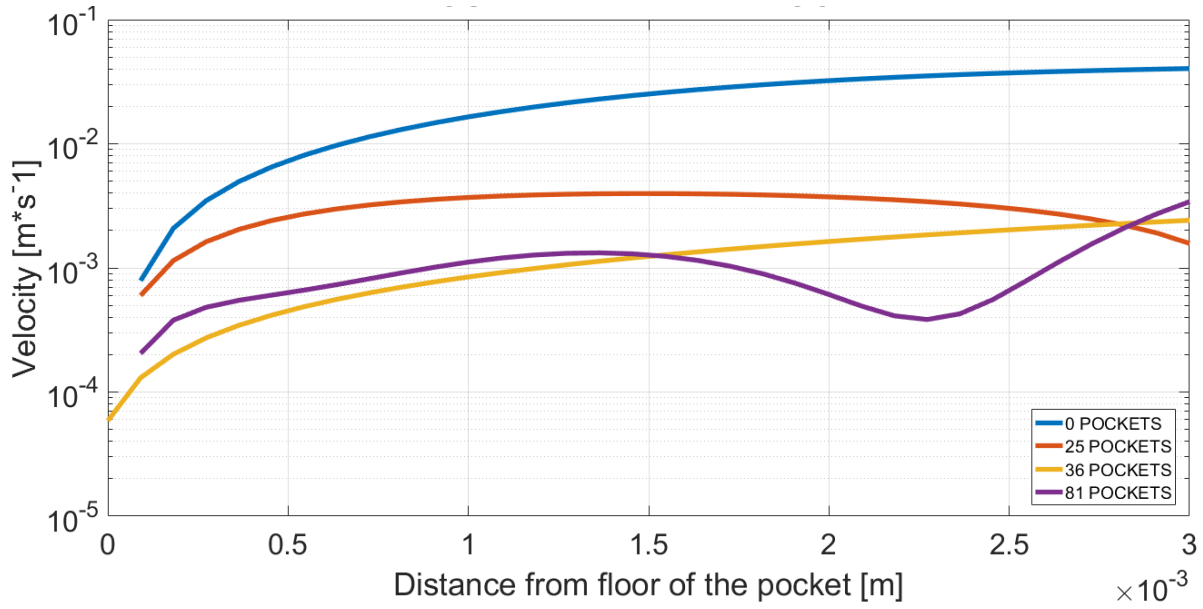


Figure 35: Semilog plot of the water velocity at the Boundary Layer

4.3.1.4. Force Analysis

Given that algal cell debris (functionally considered as seed along the cultivation process) travel in the water flow of the ATS, they attach to surfaces due to the benthic nature identified for the species for this cultivation process. Since they travel throughout the surface of the pockets and nearby the 0-pocket flat surface as well, the information provided by the models characterizing the velocity at the boundary layer can be used to perform a force analysis considering cells as a single particle. Such analysis is shown in the next section.

Lift, Gravitational, Buoyancy, and Drag are the forces that were subject of analysis for this discussion. The free body diagram with these forces acting on algal cell debris is shown in Figure 36.

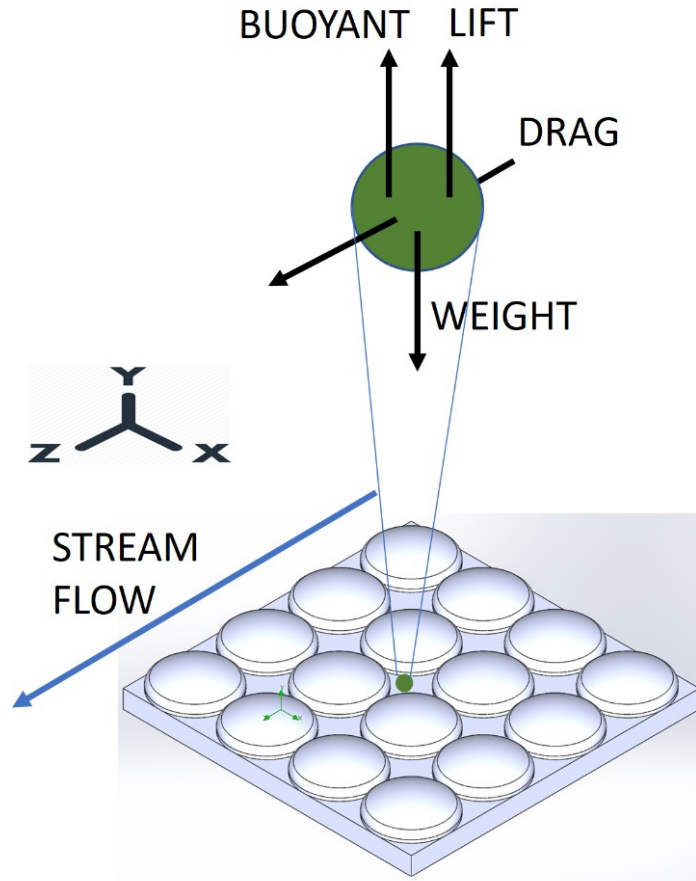


Figure 36: Free body diagram of algal cell debris

Contact forces, (adhesion forces and friction forces) and electrostatic forces were not considered, because the scope of this discussion is to assess the conditions that precede the algal biofilm formation, and this implies analyzing algal debris traveling throughout the neighborhood of the surface of the plates.

For the estimation of these forces, the following values were:

Density of the particle: $\rho_{\text{particle}} = 1370 \text{ [Kg} \cdot \text{m}^{-3}]$ (value taken from models found in the literature (Padisák et al., 2003)), (Thornton et al., 2010).

Density of the fluid: $\rho_{\text{WATER}} = 997 \text{ [Kg} \cdot \text{m}^{-3}]$, (at 25°C)

Diameter of an algal cell: $d=1.3\text{E-6 [m]}$ (spherical approach)

Gravitational acceleration on earth: $g= 9.8 \text{ [m} \cdot \text{s}^{-2}]$

Water viscosity: $\eta= 8.9\text{E-4 [Pa.s]}$, (at 25°C)

4.3.1.4.1. Lift Forces

For the current analysis, algal cell debris located inside the pocket or at the surface of the flat substratum are exposed to lift forces (F_L) whose magnitude is described by the following expression according to (Wang et al., 1997; Zoetewij et al., 2009):

$$F_L = 1.615 \eta d^2 \frac{\rho_{\text{WATER}}^{0.5}}{\eta^{0.5}} u^{0.5} U$$

where η is the viscosity of water, d is the diameter of the particle and ρ_{WATER} is the density of water, u is the partial derivative of the water velocity with respect to the perpendicular stream-wise direction ($\frac{\partial U}{\partial y}$) and U is the flow velocity at the particle location.

In other words, the lift force can be expressed in terms of a constant ($C= 2.57 \times 10^{-12}$), the water velocity at a given location and its derivative.

$$F_L = C u^{0.5} U$$

4.3.1.4.2. Gravitational and Buoyancy Forces

The weight of any particle is given by the following expression:

$$W = \rho_{\text{particle}} * V * g$$

While the buoyancy force exerted by the water body onto the particle is given by:

$$B = \rho_{\text{water}} * V * g$$

where **W** is the weight of the particle, **B** is the buoyant force (in the opposite direction of the weight), ρ_{particle} is the density of the particle, ρ_{water} is the density of water, **V** is the volume of the particle and **g** is the gravitational acceleration on earth. Rewriting the previous mathematical expressions in terms of the diameter of the particle **d** (assuming a spherical shape for this approach), this gives the following relationship:

$$W = \rho_{\text{particle}} * \frac{4}{3} \pi * \frac{d^3}{8} * g$$

$$B = \rho_{\text{water}} * \frac{4}{3} \pi * \frac{d^3}{8} * g$$

Replacing the numbers:

$$W = 1.5 \times 10^{-14} \text{ [N]}$$

$$B = 1.12 \times 10^{-14} \text{ [N]}$$

The previous analysis shows how lift forces depend on both: water velocity and its derivative, while weight and buoyancy are constants by nature.

Since it has been shown that the generated pockets are regions where water velocity increases as it gets away from the surface, the velocity boundary layer gains more relevancy to characterize the lift forces. For this reason and given the fact that the simulator provided the profile of the velocity boundary layer, a theoretical comparison between the lift forces among the four tested treatments was performed based on the mathematical models for the water velocities shown on Table 8. The lifting forces at the boundary layer of the plates are plotted on Figure 37.

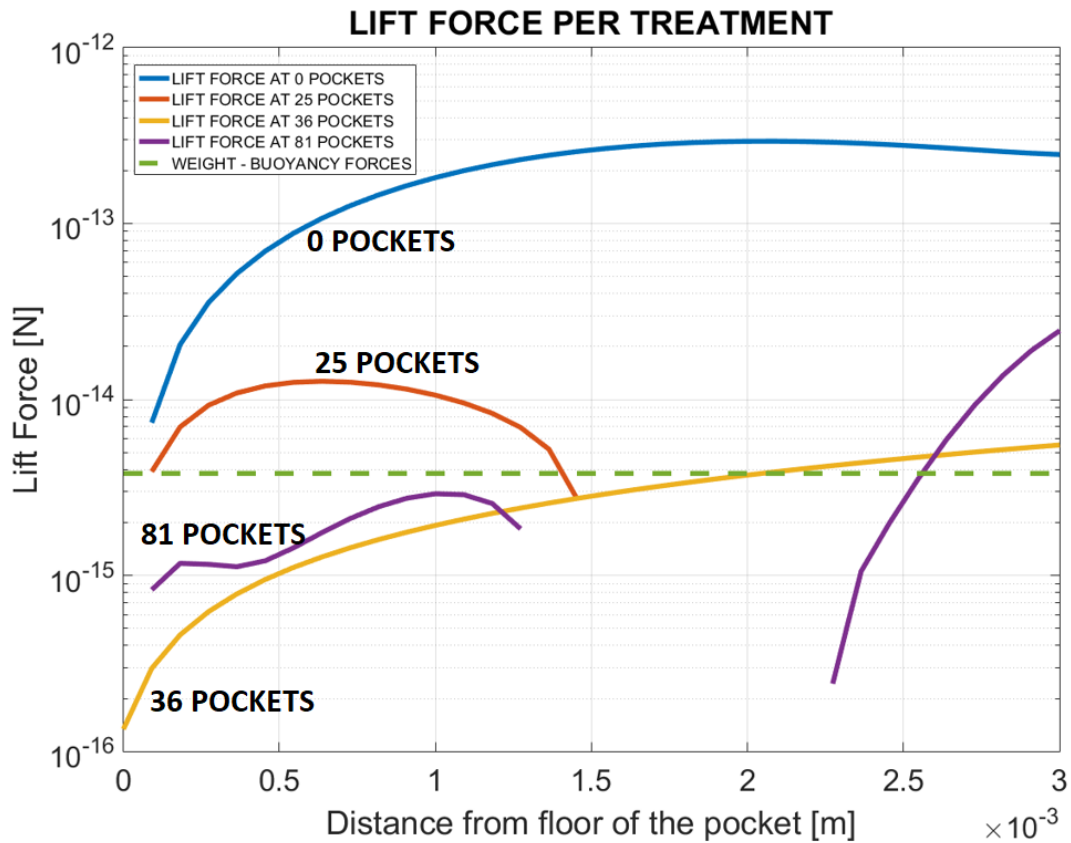


Figure 37: Theoretical Lift force at the boundary layer of the treatments

The plot on Figure 37 shows that along the 3 millimeters above the floor of the pocket, the lifting forces present on the 0-pocket treatment keep an order of magnitude larger in comparison to the other treatments. The lifting forces for the three treatments having pockets are clustered together below the lift force profile of the 0-pocket treatment. This observation agrees with the results for the biomass density because the treatments with pockets were clustered as well and they ended up having significantly more biomass density than the 0-pocket treatment. This fact can be used as evidence to hypothesize that because of the reduction on the lift forces through the treatments with pockets, a better algal colonization can be achieved on the pocket-treatments.

In addition to the previous observation, the treatments having 25 and 81 pockets shows regions inside the pocket lacking lifting forces. This happens approximately between 1.25 mm and 2.25 mm above the flat surface of the pocket for the 81-pocket treatment and beyond 1.5 mm for the 25-pocket treatment. The mathematical reason for this is that the lift force is dependent not only on the velocity but also on its derivative and in such regions the derivative is negative given the decreasing behavior of the velocity profile. Probably, for this reason, these two treatments are leading the cluster that yielded more biomass density on average as shown in Figure 21.

From the analysis performed for the weight and the buoyant forces, it can be noticed that given the slight differences in density, algal cells have a tendency to sink. However, since the net force between the weight and buoyancy forces can be calculated as 0.38×10^{-14} [N] (plotted on the discontinuous green dashes on Figure 21), this value could be used as threshold to hypothesize that lift forces above this threshold could generate a net force

pulling algal cells outwards from the surface of the plates, and the opposite effect might occur for the lift forces below the threshold.

4.3.1.4.3. Drag Forces

Algal cells are also exposed to drag forces (Koehl et al., 2003), which is expressed by the following relationship:

$$F_D = \frac{1}{2} \rho_{\text{WATER}} U^2 C_D A$$

where ρ_{WATER} is water density, U is water velocity, C_D is the Drag coefficient and A is the effective area of the particle.

The Drag coefficient for small particles with small particle Reynolds number ($10^{-4} < Re_p < 2$) (Zoetewij et al., 2009) can be expressed by the following expression :

$$C_D = 1.7009 f$$

where f is a factor that represents the friction on a spherical particle that is dependent on the particle Reynolds number (Re_p). 1.7009 is a correction factor for the changing flow pattern around the walls of the particle (O'Neill, 1968)

$$f = \frac{24}{Re_p}$$

So, the Drag coefficient profile can also be represented by the following expression:

$$C_D = \frac{40.82}{Re_p}$$

Particle Reynolds number is analogous to the fluid Reynolds number in the sense that this parameter describes the behavior of the particle in a flow. Re_p is function of the density of the fluid (ρ_{WATER}), the diameter of the particle (d), the viscosity of the surrounding fluid (η) and the water velocity (U).

$$Re_p = \frac{d\rho_{WATER} U}{\eta}$$

Figure 38 shows the profile for the Particle Reynolds number at the boundary layer of the treatments.

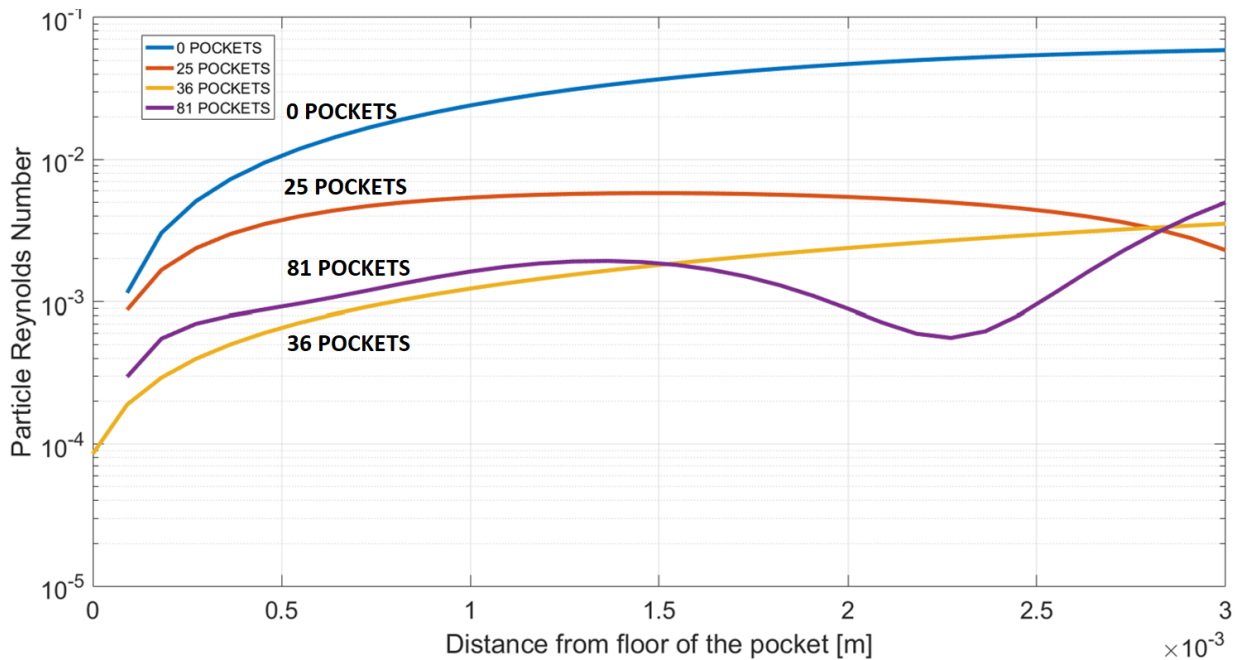


Figure 38: Theoretical Particle Reynolds number per treatment at the boundary layer

It is relevant to consider on the low Reynolds numbers obtained and the implications of it. The low particle Reynolds number is due to the size of the particle. For example, a bacterium cell has a calculated particle Reynolds number of 10^{-5} (Berg, 1993). Low Reynolds numbers basically imply that inertia is negligible compared to drag (Vogel, 1996).

Plugging the previous relationships into the formula for Drag Forces, the following expression is obtained:

$$F_D = \frac{1}{2} \rho U^2 \left(1.7009 \frac{24}{\eta} \right) A$$

The effective area of the particle (**A**) is given by a circular shape with the following expression:

$$A = \frac{\pi d^2}{4}$$

where **d** is the diameter of the particle (algal cell).

Therefore, a general expression for the calculated Drag force is:

$$F_D = B U$$

Where $B = 16 * \eta * d$.

For $\eta = 8.9E-4$ [Pa.s] (water viscosity), $d = 1.3E-6$ [m] (approach of an algal cell size), the factor **B** equals $1.9E-8$ and the Drag Force **F_D** can be estimated as:

$$F_D = 1.9E-8 U [N]$$

where U is the water velocity. It can be noticed that drag forces are likewise function of the water velocity and it can be analyzed in a similar way as the lift forces. Figure 39 shows the theoretical behavior of the drag forces inside the pockets.

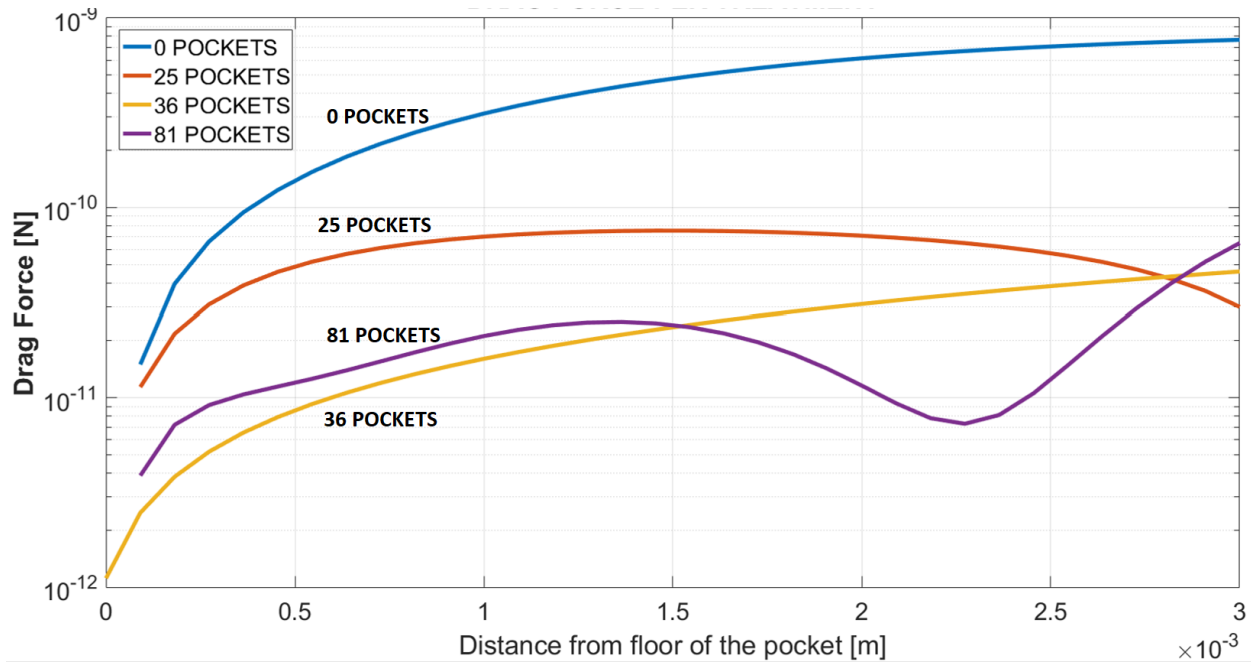


Figure 39: Theoretical drag force per treatment at the boundary layer

Figure 39 shows that because of the low particle Reynolds number, drag forces are modulated primarily by the viscosity of the fluid, and the differences between treatments are due to the water velocity profile at the boundary layer for each of them. Along the 3 millimeters above the floor of the pocket, the drag forces present on the 0-pocket treatment remain an order of magnitude greater in comparison to the other treatments. The drag force for the three treatments having pockets is clustered below the drag force profile for the 0-pocket treatment, which agrees with the results for the biomass density, where these same treatments with pockets achieved significantly more biomass density than the 0-pocket treatment. Based on the previous statement, it could be also

hypothesized that because of the reduction on the drag forces along the treatments with pockets, a higher rate of algal colonization was achieved.

Finally, the drag coefficient profile can also be presented as function of the Particle Reynolds Number (see Figure 40).

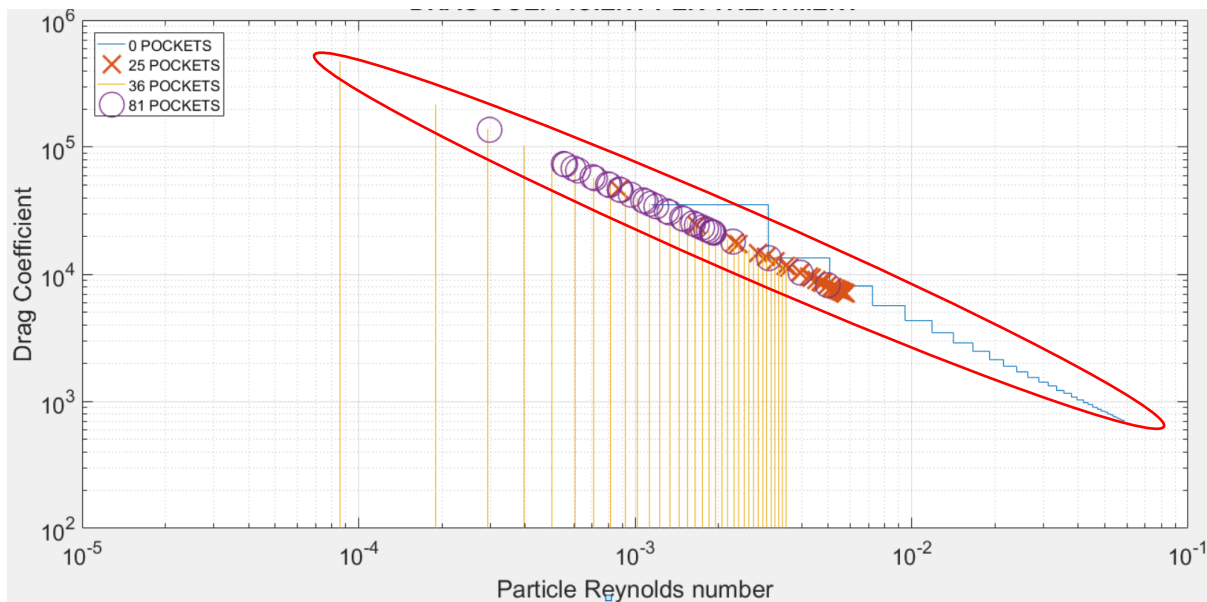


Figure 40: Drag coefficient as function of the Particle Reynolds number for the treatments at the boundary layer

Figure 40 puts in context the hydrodynamic conditions present on the current project. These are low Reynolds numbers generating high drag coefficients. This is basically because the viscosity and the effects of shear in the fluid dominate any inertial effects coming from the particles (algal cells) subject of discussion on this section (Vogel, 1996). It can be identified on the plot that the treatments with pockets (which yielded better algal densities) are concentrated in the region with Particle Reynolds number below 4×10^{-3} , hence obtaining drag coefficients above 6×10^3 . Probably this is an optimal zone that

enhances faster algal cultivation responses in a turbulent environment such as the one generated inside the algal turf scrubber.

5. Experiment 2: Comparative analysis of the functional performance between a traditional and a novel high surface area 3D printed media in a Moving Bed Biofilm Sequencing Batch Reactor for Wastewater Treatment

5.1. Materials and Methods

5.1.1. Mathematical modeling of the gyroids

The carriers were fabricated with the goal of maximizing the capabilities of Additive Manufacturing in building complex geometries to meet the requirements for optimal bacterial development in moving beds. Such requirements are the achievement of a high specific surface area, an optimal void size resulting in minimum clogging and enough shelter so that it protects bacterial biofilm from sloughing.

An approach that meets the previous requirements is the gyroid, which can be represented by a mathematical surface based equation in terms of sine and cosine functions (Equation 1) that lack straight lines (Schoen, 1970).

$$\sin x * \cos y + \sin y * \cos z + \sin z * \cos x = 0 \quad [1]$$

Equation 1 represents the mathematical model of the gyroid shown in Figure 41 by using Mathematica®.

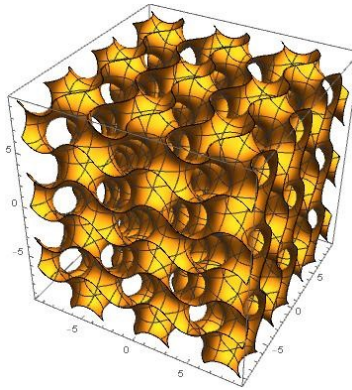


Figure 41: Gyroid surface

Mathematica® has the option of truncating any surface into any other 3D shape. For example, by introducing the instruction displayed on Code 1, the surface previously generated by equation 1 gains the shape of a sphere of radius 10 mm (Equation 2). The final surface is shown in Figure 42.

[Code 1]

```
gyroid = ContourPlot3D[Cos[x]Sin[y] + Cos[y]Sin[z] + Cos[z]Sin[x] == 0,
  {x, -3π, 3π}, {y, -3π, 3π}, {z, -3π, 3π},
  RegionFunction → Function[{x, y, z}, x2 + y2 + z2 < 100],
  Extrusion → 0.25, Mesh → None, ViewPoint → {1,1,1}]
```

$$x^2 + y^2 + z^2 < 100$$

[2]

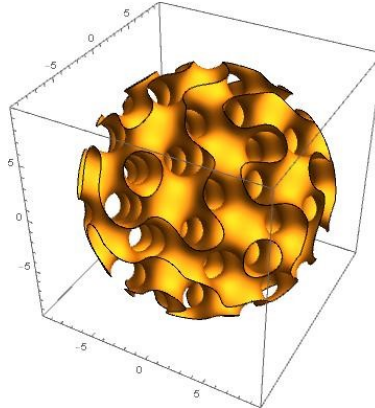


Figure 42: Spherical gyroid surface

Modifications of Code 1 resulted in three different gyroid surfaces with different truncated sphere shapes and different specific surface areas. Particularly, the parameter *Extrusion* was modified to provide different wall thicknesses on the gyroid so that it was rigid enough both for the post-printing process and for the constant agitation once inside the reactors during operation. The frequency of the sinusoidal functions was also modified to provide different levels of void sizes and hence different levels of surface area per carrier type. A summary of the coding used in Mathematica for each gyroid type is shown in Table 9.

Table 9: Modification to Code 1 to achieve the three gyroid types.

Gyroid Surface Area type	Coding implemented in Mathematica® per gyroid type
Small	<pre>gyroidSMALL = ContourPlot3D[Cos[0.5 x] Sin[0.5 y] + Cos[0.5 y] Sin[0.5 z] + Cos[0.5 z] Sin[0.5 x] == 0, {x, -3 π, 3 π}, {y, -3 π, 3 π}, {z, -3 π, 3 π}, RegionFunction -> Function[{x, y, z}, x² + y² + z² < 100], Extrusion -> 0.60, Mesh -> None, ViewPoint -> {1, 1, 1}]</pre>
Medium	<pre>gyroidMEDIUM = ContourPlot3D[Cos[x] Sin[y] + Cos[y] Sin[z] + Cos[z] Sin[x] == 0, {x, -3 π, 3 π}, {y, -3 π, 3 π}, {z, -3 π, 3 π}, RegionFunction -> Function[{x, y, z}, x² + y² + z² < 100], Extrusion -> 0.40, Mesh -> None, ViewPoint -> {1, 1, 1}]</pre>
Large	<pre>gyroidLARGE = ContourPlot3D[Cos[1.5 x] Sin[1.5 y] + Cos[1.5 y] Sin[1.5 z] + Cos[1.5 z] Sin[1.5 x] == 0, {x, -3 π, 3 π}, {y, -3 π, 3 π}, {z, -3 π, 3 π}, RegionFunction -> Function[{x, y, z}, x² + y² + z² < 100], Extrusion -> 0.20, Mesh -> None, ViewPoint -> {1, 1, 1}]</pre>

The conversion of the surface model to STL format is performed by Code 2

[Code 2]

```
Export["gyroid.stl", gyroid]
```


5.1.2. Fabrication of the gyroids.

The fabrication of the gyroids was done by means of Additive Manufacturing. The technology implemented over the process required refined methods of post-processing according to the carrier type.

5.1.2.1. Printing Parameters

The three gyroid carrier types once designed and converted into STL were fabricated using Additive manufacturing with an Objet-30 machine (Stratasys® Ltd., Eden Prairie, Minnesota). This printer uses PolyJet technology to deposit a 28 µm thick layer of UV-light cured acrylic polymer. As previously explained, the three gyroid carrier types provided three different levels of surface area: a small, medium, and a large surface area such that were subject to comparison against a control treatment based on a commercial Kaldness 1 carrier. The 3-D printer was capable of printing batches of twelve carriers at a time. Once the printer finished printing a batch of carriers, it then had to be cleaned to remove the excess support material. Each carrier had its own specific way of being cleaned.

Once the outer support material was removed from the carriers, they were soaked in sodium hydroxide (NaOH 0.5 % w/v) to break up the remainder of the support material mostly inside the carrier. Each type of carrier had different soaking times in the NaOH bath. After each type of carrier had soaked in the solution for its specified time, the carriers were removed from the bath and poked with a needle to break up the support material

inside the carrier and then moved to the water jet station. Then the carriers were water-jetted at a specific flow rate corresponding to each type to finish the cleaning process.

5.1.2.2. Printing post-process

A combination of soaking in a sodium hydroxide solution, water jetting and poking inside the printed carrier, allowed the support material to be removed from the printed gyroids. However, given the different levels of geometries and void sizes of the carriers, selective refinement was needed to achieve a proper removal of the support material.

5.1.2.2.1. Cleaning process for carrier with small surface area.

The carrier with the small surface area had large holes (voids) and had to be handled with care because it was delicate in comparison to the two others. After a batch of small surface area gyroids was fully printed, the excess support material was removed, which took approximately ten minutes to complete. After the excess support material was removed, the small surface area carriers were placed in a glass beaker that was able to fit all the carriers. Once placed in the beaker, NaOH (0.5 % w/v) was poured into the beaker submerging all the carriers. The NaOH was used because it slowly softened the support material making it easier to remove. The beaker full of NaOH and the carriers were left to sit for approximately two to three hours. If the small surface area carriers were left to sit in the NaOH for too long, then the NaOH would compromise the rigidity of the carrier and it would begin to crack. Once the small area carriers had soaked long enough they were removed one by one to remove the support material with a needle. Removing the support material with a needle took around ten minutes per carrier. After most of the support material was removed using the needle, the small surface area carrier was taken

to the water jet station and washed with a water jet on low to remove the remaining support material. Once the carrier was washed with the water jet, it was placed on a paper towel to allow it to dry. When dried, the carriers were inspected for any support material remaining on them. If there was any support material remaining, it was again washed in the water jet station and dried. After all the twelve small surface area carriers were completed, placed in a labeled storage container and stored until the bacterial inoculation stage.

5.1.2.2.2. Cleaning process for carrier with medium surface area.

Similarly, the carrier with the medium surface area, once removed from the 3-D printer, had the excess support material which had to be removed and all twelve of the carriers were placed in the NaOH solution bath to be soaked. The medium surface area carriers were left to soak in the solution for twelve to twenty hours. If the carrier was left to sit for more than twenty hours, then the material would become brittle and it would crack. After soaking, the medium surface area carriers were removed and poked with a smaller needle from the carriers with the small surface area. Once most of the support material was pushed out, the carriers were moved to the water jet station and jetted on low to medium flow and set out to dry. The last two steps sometimes needed to be repeated depending on if there was any support material left in the carriers. If the medium surface area carrier was finished, it was put in a separate labeled storage container until the bacterial inoculation stage.

5.1.2.2.3. Cleaning process for carrier with large surface area.

Finally, the carrier with the largest surface area once removed from the 3-D printer had the excess support material which had to be removed, and all twelve carriers were placed in the NaOH bath to be soaked as well. The large surface area carriers had to soak for at least twenty-four hours. After the small surface area carriers soaked for at least a day, they were removed from the acid bath and placed in the water jet station to be jetted with water at a very high velocity. Once washed with water, the biocarriers were submerged again in the solution bath and sat for another twelve to fifteen hours. These steps needed to be repeated for a total of four submersions in the bath. After the last water jet session, they were set out to dry. Following drying, the carriers were inspected and if it failed inspection the process of cleaning was repeated. If the carrier passed inspection it was placed in a separate labeled storage container until the bacterial inoculation stage.

5.1.3. Specific Surface Area characterization of the carriers

In order to quantify the specific surface area of the 3D printed gyroids, a combination of mathematical computation and information related to the designed carrier provided by software was required.

5.1.3.1. Gyroids' Specific Surface Area determination

The specific surface area is the ratio between the surface area and the bulk volume occupied by the carrier. The method implemented for estimating each of these parameters is explained in detail.

5.1.3.1.1. Gyroids´ Surface Area determination

The surface area of the carrier was obtained with the aid of Netfabb®, an additive manufacturing software that provides information on the 3D models including the surface area and the true volume of the part. True volume is defined as the effective volume occupied by the part without considering the holes (voids) of it. A snapshot of the working area of the software is shown in Figure 43.

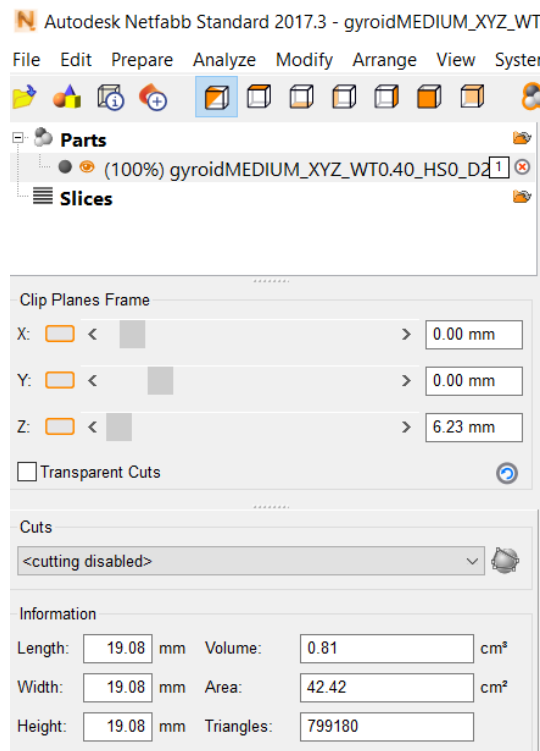


Figure 43: Netfabb® workspace for surface area determination of 3D models

Figure 43 shows the information of the STL file generated for the gyroid with medium surface area. It can be seen the information regarding the effective volume, displayed just as volume (0.81 cm³) and the area (42.42 cm²). This information was retrieved from the two other gyroid models and used for experimental design purposes.

Table 10 summarizes the surface area of the three gyroid models

Table 10: Surface Area per carrier unit determination from 3D models

Carrier type	Surface Area (taken from Netfabb®) (units in m²)
Small surface area gyroid	0.002194
Medium surface area gyroid	0.004242
Large surface area gyroid	0.008296

5.1.3.1.2. Gyroids' bulk volume determination

Even though Netfabb® provides information on the true volume of the part, the calculation of the specific surface area was based on the bulk volume. Since the three gyroid models were designed with spherical shapes, the volume of a sphere was considered for the calculation. Given the diameter (d) of the gyroid (10 mm) and the formula for a sphere ($V = \frac{4}{3} * \pi * (d/2)^3$), the bulk volume of the gyroid was obtained by simple geometry.

Table 11 summarizes the bulk volume of the three gyroid models.

Table 11: Bulk volume of gyroids

Carrier type	Bulk Volume (calculated by geometry) (units in m³)
Small surface area gyroid	4.19 x 10 ⁻⁶
Medium surface area gyroid	
Large surface area gyroid	

5.1.3.1.3. Gyroid's Specific Surface Area calculation

With the previous information regarding the surface area and the bulk volume of the gyroids, the specific surface area of the gyroid was calculated as the ratio between both parameters. Table 12 summarizes the specific surface areas obtained for each gyroid type.

Table 12: Specific surface area per gyroid type

Carrier type	Specific Surface Area (surface area/bulk volume (units in m²/m³))
Small surface area gyroid	523.78
Medium surface area gyroid	1012.70
Large surface area gyroid	1980.52

5.1.3.2. Kaldnes' Specific Surface Area determination

In a similar way as the gyroids, Kaldnes' specific surface area was determined. However additional software mediation was required to compute it.

5.1.3.2.1. Kaldnes' Surface Area estimation

To keep consistency later on the experimental design to test the functionality of the printed carriers, a similar approach was followed for the case of the control treatment (commercial carrier) even though a nominal value of $500 \text{ m}^2/\text{m}^3$ has been reported in literature under the denomination of specific biofilm surface area (Rusten et al., 2006). However, this value only considers the inner surface area of the carrier's wall because such location has been reported as where the development of the bacterial biofilm mostly takes place.

5.1.3.2.1.1. Reverse Engineering technique for Kaldnes' Surface Area determination

To obtain the quantification of the whole surface area of the commercial carrier, a reverse engineering approach was considered. The dimensions of a carrier sample were taken with a digital caliper (Westward® Model: 1AAU4, resolution: 0.01 mm) and the part was rebuilt to a 3D model using Solidworks® (Dassault Systèmes SolidWorks Corp., Waltham, Massachusetts). The purpose of the described process was to be able to import the file into Netfabb® and retrieve the information regarding its surface area.

The digital file of the carrier, the 3D printed version of the commercial carrier and the sample used for the reverse engineering process is shown on Figure 44.

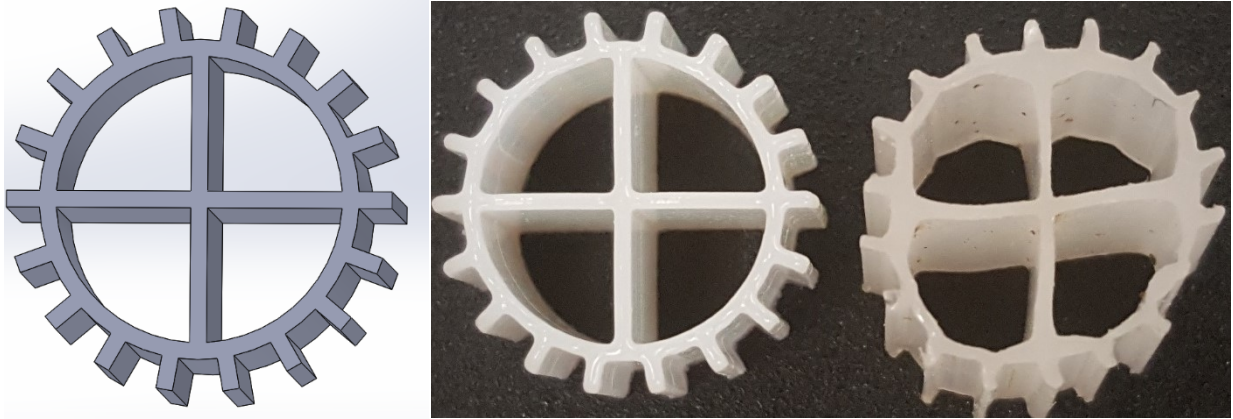


Figure 44: K1 carrier, from left to right: digital file, 3D printed part, commercial

With the generated 3D model, the information of the surface area could be retrieved from Netfabb®, and it is shown in Table 13.

Table 13: Surface area information from Netfabb® for the reverse-engineered Kaldnes 1

Carrier type	Surface Area (taken from Netfabb®) (units in m²)
Kaldnes 1	0.000944

5.1.3.2.2. Kaldnes´ volume determination

Similarly, the calculation of the specific surface area of the gyroids was based on the bulk volume of the carrier. The shape of a cylinder was used on the calculation, where the diameter (d) of the commercial carrier was measured in an average of 10.39 mm and the average height (h) was 7.33 mm. The formula for the volume (V) of a cylinder is given by $V = \frac{4}{3} * \pi * (d/2)^3$, hence the bulk volume of the commercial carrier was determined in $6.21 \times 10^{-7} \text{ m}^3$ as shown in Table 14.

Table 14: Calculated bulk volume for Kaldnes 1

Carrier type	Bulk Volume (calculated by geometry) (units in m³)
Kaldnes 1	6.21 x 10 ⁻⁷

5.1.3.2.3. Kaldnes's Specific Surface Area calculation

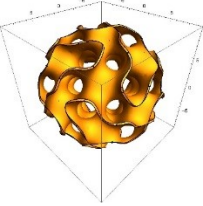
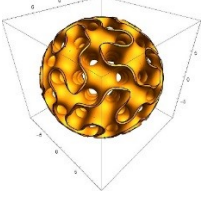
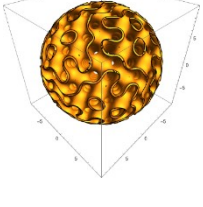

With the previous information regarding the surface area and the bulk volume of the commercial carrier, the specific surface area was calculated by obtaining the ratio between both parameters. Table 15 shows the result of the calculation.

Table 15: Calculated specific surface area for Kaldnes 1

Carrier type	Specific Surface Area (surface area/bulk volume (units in m²/m³))
Kaldnes 1	1518.96

Table 16 shows a summary of the parameters from each carrier type that were used as information for the experimental design to test the operational functionality of the printed carriers.

Table 16: Summary of parameters for carriers

Carrier aspect	Carrier denomination	Surface area (m²)	Bulk Volume (m³)	Specific Surface area (m²/m³)	Material density (Kg/m³)
	SMALL SSA gyroid	0.002194	4.9 X 10 ⁻⁶	523.78	1,033
	MEDIUM SSA gyroid	0.004242	4.9 X 10 ⁻⁶	1012.70	1,033
	LARGE SSA gyroid	0.008296	4.9 X 10 ⁻⁶	1980.52	1,033
	K1	0.000944	6.21 X 10 ⁻⁷	1518.96	950 (Ødegaard et al., 2000)

5.1.4. Moving Bed Biofilm Sequencing Batch Reactor (MBBSBR) design, fabrication, and operation

5.1.4.1. MBBSBR system components

The functionality of the carriers was tested by means of the implementation of a lab scale Moving Bed Biofilm Sequence Batch Reactors (MBBSBR) system. The system comprised two water baths, each one of them at the same time kept 6 MBBSBR with a volume capacity for treating 1.3 liters of synthetic wastewater per reactor. Physical conditions were controlled to provide optimal conditions to enhance nitrification processes as the main biological mechanism to test and compare the functional performance of each gyroid type. A picture of the actual setup of one of the two baths with a front and a top view sketch of it including dimensions of it are shown in Figure 45.

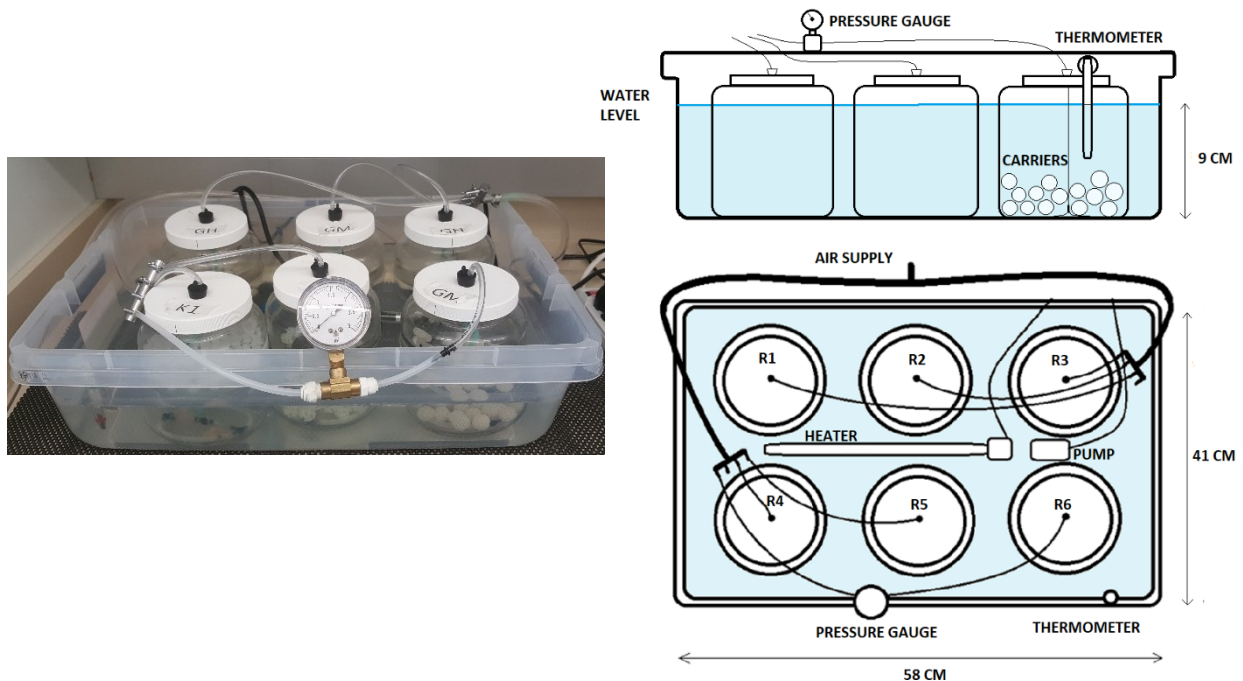


Figure 45: Picture and sketch of part of the MBBSBR system for experiment 2

The reactors were built by using commercial 2-liter jars (height: 15 cm) with an aeration mechanism and sampling ports, which are described in detail (See sketch in Figure 46).

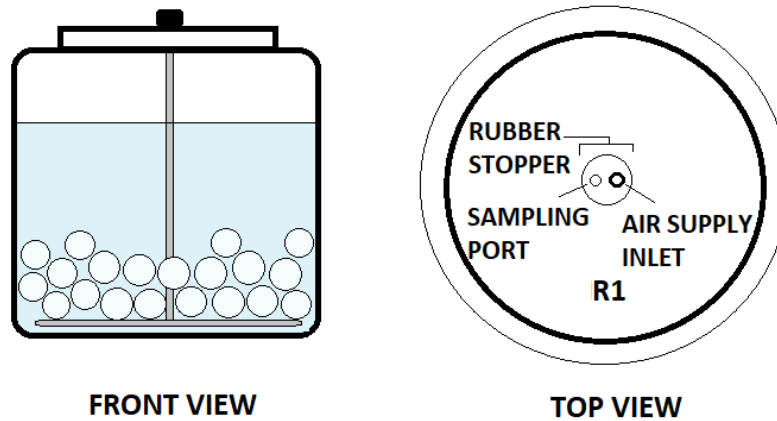


Figure 46: Sketch of a single MBBSBR and components

5.1.4.2. Aeration Mechanism for MBBSBR operation

The density of the gyroids is higher than water, so their natural tendency is to sink to the bottom of the reactor. For this reason, an aeration ring (diameter: 11 cm) was fabricated (see sketch on Figure 47) that worked with the main air supply provided by the building where this experiment took place (CASIC building). The aeration mechanism had two main functions: 1) to provide aerobic conditions to the nitrifying bacteria growing inside the reactors, and 2) to provide motion and agitation to the gyroids.

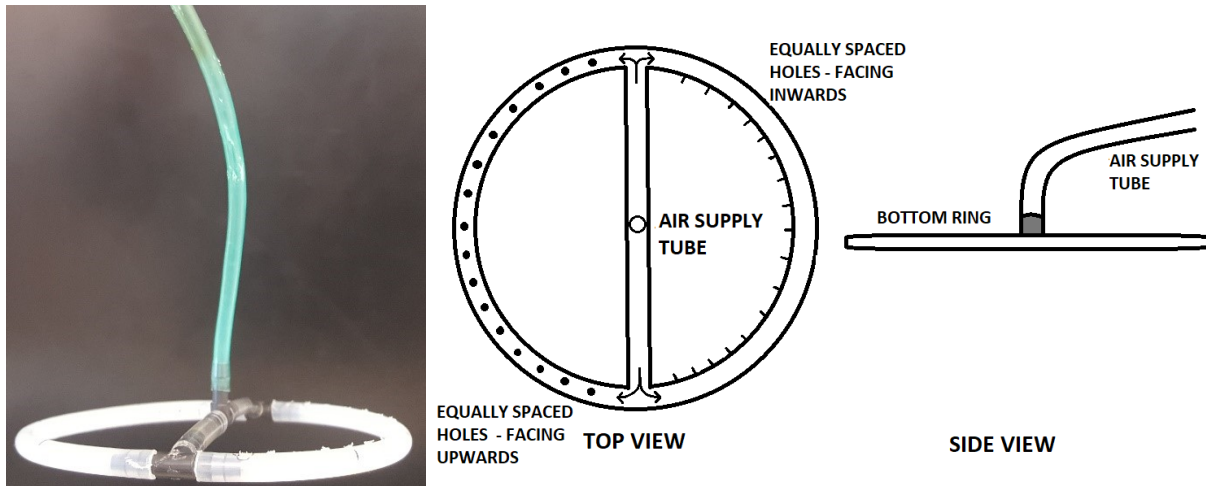


Figure 47: Picture and sketch of the aeration ring inside the MBBSBR

The aeration ring was built with plastic tubing for fish tanks, a special silicone flexible airline tubing for the vertical section of the aerator and T couplers. The design included equally spaced 1mm holes (7 cm separation) to inject air coming from the main supply. It was identified that the proper way to allow the gyroids to move upwards was by generating two directions on the air injection: 1) one half of the ring with the holes facing inwards to the center, and 2) the other half of the ring with the holes facing upwards.

5.1.4.2.1. Dissolved Oxygen (DO) considerations for nitrifying conditions

The dissolved oxygen concentration inside the reactor was a key factor to achieve nitrification. For this reason, a proper air supply pressure was constantly monitored in such a way that the operational level of DO inside the reactors was kept close to 5 ppm.

For this to happen, the air supply was manually opened by means of a valve, passed through a series of plastic tubing, T couplers, and metallic manifolds to finally reach each

of the air inlets located on the lid of the jars. The two sets of reactors were monitored with a pressure gauge with an operational level of 1 PSI of air supply.

According to (Rusten et al., 2006), for the conditions set in the reactor where there is no organic load, any DO concentration above 2 mg O₂/ L was enough to achieve nitrification. However, nitrification rates are limited by ammonium concentrations below 3 mg NH₄-N / l (Ødegaard, 1999). Since DO was controlled at 5 ppm, it was expected a nitrification rate below 1.5 [g NH₄-N/ m² d] when the ammonium concentration was 2 ppm (DO limited) and close to 1 [g NH₄-N/ m² d] when the ammonium concentration was 1 ppm (ammonium limited).

5.1.4.3. Temperature Conditioning for MBBSBR operation

The nitrification process was designed to be performed by microbial mediation, specifically by bacteria genus *Nitrosomonas* and *Nitrobacter* whose nitrifying activity is enhanced when their medium is kept at temperatures close to 30°C (Hofman & Lees, 1953). For this reason, the reactors were temperature conditioned by submerging them into a water bath that was constantly warmed by a submerged heater with an incorporated thermostat that was set at such temperature. To provide homogeneity to the bath and same temperature along the six reactors per bath, a pump was submerged. Bath temperature was monitored with a mercury thermometer attached to each of them.

5.1.4.4. Sampling Mechanism for MBBSBR

The lid of the jar was perforated and a rubber stopper with two small holes was placed on top. One of the holes served as air supply inlet and the other one worked as a sampling port that remained closed during operation by means of a port plug. When sampling was required, air supply was stopped and the treated water was allowed to sit for 30 minutes; a port plug was removed, and the sampling took place with a 100 mL syringe. (see Figure 48).

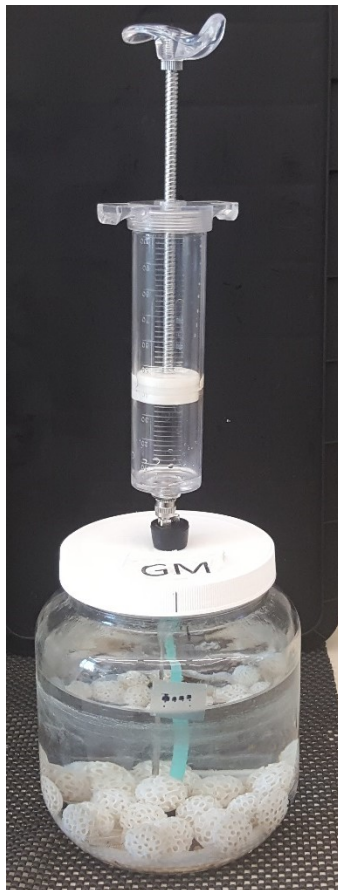
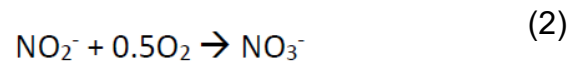
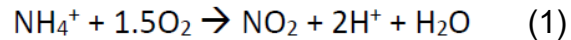


Figure 48:100 mL syringe for taking water samples

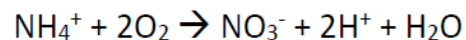
5.1.5. MBBSBR operational design

The operation of MBBRs is based on the microbial activity that takes place on the surface of the biocarriers. Therefore, the operational design parameters aimed to replicate the following conditions that enhance such activity. Bacteria in aquatic ecosystems interact with natural wastes that result in nitrogenous nutrients such as Ammonia (NH₃) and Ammonium ions (NH₄⁺). Their oxygen uptake is followed by the production of carbon dioxide as part of its respiration process, while at the same time oxidation processes take place to convert the ammonia into nitrites and nitrites into nitrates.

Equation (1) and (2) taken from (Boyd, 2015) describe the chemistry behind these processes.



Nitrosomonas, cause the first oxidation process (1). The second oxidation process (2) is conducted by *Nitrobacter*. These two types of bacteria usually cohabit together in the same aquatic environment. The overall reaction along this nitrification process can be summarized by the following equation (Boyd, 2015):



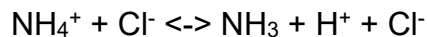
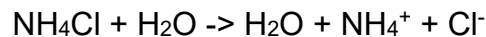
The previous chemical interactions were replicated by means of the preparation of a synthetic water whose protocol is described in detail in the following sections.

5.1.5.1. Ammonia as the substrate for testing carriers' functional performance

The performance of the carriers was tested by comparing their removal activity on the ammonia present in a prepared synthetic water that was converted into nitrates.

The recipe for the preparation of the synthetic water is described later, but its principle is based on the presence of ammonia that was generated with the addition of ammonium chloride (5 mg NH₄Cl / L during preliminary experimentation and 10 mg NH₄Cl / L during experimentation).

The stoichiometric analysis for the dissociation of ammonium chloride in water and its conversion into ammonia is shown in detail:



So, with the molar ratio between ammonium chloride and ammonia (1:1) and the molecular weight (MW) of ammonia and ammonium chloride, the starting concentration of ammonia present in the synthetic water was able to be predicted:

$$[\text{NH}_3] = [\text{NH}_4\text{Cl}] * \frac{\text{MW NH}_3}{\text{MW NH}_4\text{Cl}}$$

Since the molecular weight of ammonia (NH₃) and ammonium chloride (NH₄Cl) are respectively 17.03 g/mol and 88.94 g/mol, hence:

$$[\text{NH}_3] = 0.19 [\text{NH}_4\text{Cl}]$$

For the two concentrations of ammonium chloride, the starting concentrations, amount of ammonia and ammonium into 1.3 L of synthetic water per reactor are shown in Table 17.

Conversions were calculated by molecular weight:

MW of N: Molecular weight of Nitrogen : 14 g/mol

MW of NH₃ : Molecular weight of Ammonia : 17 g/mol

MW of NH₄⁺: Molecular weight of Ammonium: 18 g/mol

NH₃-N = NH₃ * (MW of N / MW of NH₃) = NH₃ * (14/17)

NH₄⁺ = NH₃ * (MW of NH₄⁺/ MW of NH₃) = NH₃ * (18/17)

NH₄⁺-N = NH₄⁺ * (MW of N / MW of NH₄⁺) = NH₄⁺ * (14/18)

Table 17: Calculated levels of ammonia for the beginning of the run

[NH₄Cl] (mg/l)	[TAN] (mg/l)	TAN mg
5.00	0.95	1.235
10.00	1.9	1.606

5.1.5.2. Surface area removal rate (SARR) considerations

Figure 49 taken from (Ødegaard, 1999) shows that the nitrification rate is DO limited when the substrate concentration exceeds a certain value, but if it doesn't then SARR is substrate limiting. For example, for the current water treatment conditions where DO was kept between 5- 6 mg O₂ /L, nitrification would not exceed 1.4 g/m²/ d (at 15°C), but it could be lower if the ammonium concentration were below 1.6 mg NH₃-N / L.

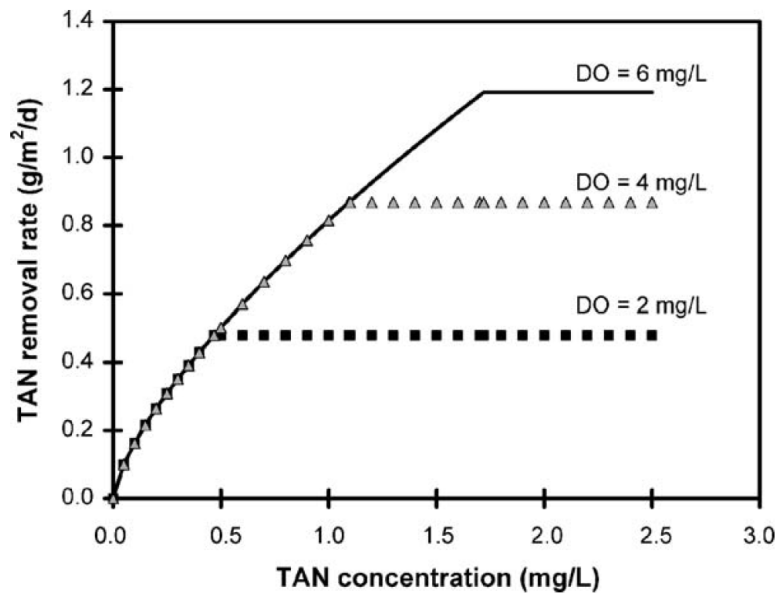


Figure 49: Influence of ammonia nitrogen and DO concentration on removal rate at 15°C (Ødegaard, 1999)

The portion of the plot on Figure 49 corresponding to substrate limiting conditions for nitrification is related to the following equation, where Ne is the concentration of ammonia:

$$SARR = \frac{Ne}{2.2+Ne} * 3.3 \text{ (Tchobanoglous et al., 2014)}$$

Table 18 summarizes the saturation limits for the family of curves shown in Figure 42

Table 18: Values of SARR_{max} and NH₃-N at SARR_{max} (at 15°C)

DO (mg/L)	SARR max g/m²/d	Min NH₃-N (effluent) at SARR max (mg /L)
2	0.61	0.5
3	0.88	0.8
4	1.03	1
5	1.23	1.3
6	1.41	1.65

Table 18 taken from (Metcalf & Eddy, 2014) shows that the maximum nitrification Surface Area Removal Rate (SARR) is 1.23 and 1.41 g/m²/d for a DO of 5 and 6 (mg/L) at 15°C respectively. To obtain the maximum value, SARR_{max}, for the current nitrifying conditions (30°C) in this experiment, the following equation was used:

$$SARR_{T=30} = SARR_{T=15} \theta^{(T-15)},$$

where T is the temperature for the current condition and θ is a biological temperature coefficient (Salvetti et al., 2006)

$$SARR_{T=30} = 1.23 * (1.058)^{(30-15)} = 2.87 \text{ (g/m}^2\text{/d)}$$

$$SARR_{T=30} = 1.41 * (1.058)^{(30-15)} = 3.28 \text{ (g/m}^2\text{/d)}$$

5.1.5.3. Surface area loading rate (SALR) considerations

The reactors were designed for 100% NH₃-N removal, so the Surface Area Loading Rate (SALR) was the same as the SARR, 3.28 (g/m²/d) for a DO concentration of 6 mg/L.

$$\frac{\text{SARR}}{\text{SALR}} = 1 \rightarrow \text{SALR} = \text{SARR} = 3.28 \text{ (g/m}^2\text{/d)}$$

5.1.5.4. Ammonia-Nitrogen loading removal rate (NH₃-N-LRR) considerations

From previous calculation, it was determined that the starting amount of ammonia nitrogen was 1.6 mg NH₃-N (Table 17) and it is designed to be removed in 8 hours, which gives an influent loading rate of 0.0048 g NH₃-N / day.

$$\begin{aligned} \text{NH}_3 - \text{N}_{(\text{loading rate})} &= \frac{\text{Initial amount of ammonia}}{\text{Hydraulic retention time}} = \frac{1.6 \text{ mg}}{8 \text{ h}} * \frac{24}{1000} \\ &= 0.0048 \text{ g NH}_3 - \text{N} / \text{day} \end{aligned}$$

5.1.5.5. Required carrier surface area (RCSA)

The required carrier surface area is given by the ratio between the ammonia-nitrogen loading rate and the surface area loading rate.

$$\text{RCSA} = \frac{\text{NH}_3 - \text{N} - \text{LRR}}{\text{SALR}} = \frac{0.0048 \text{ g NH}_3 - \text{N} / \text{day}}{3.28 \text{ (g/m}^2\text{/d)}} = 0.001463 \text{ m}^2$$

5.1.5.6. Required carrier volume (RCV)

The required volume in carriers is function of the required carrier surface area and the specific surface area of the carrier.

$$\text{RCV} = \frac{\text{RCSA}}{\text{SSA}} = \frac{0.001463 \text{ m}^2}{500 \text{ (m}^2\text{/m}^3\text{)}} = 0.00000292683 \text{ m}^3$$

The specific surface area selected for the calculation was the one reported in the literature for the Kaldnes 1 (control treatment) to have an idea of the volume required in carriers. The theoretical volume of K1s needed for an 8-hour treatment process was estimated in 1.86 mL

5.1.5.7. Alkalinity considerations for Nitrification Processes.

For nitrification to occur alkalinity conditions should be considered. For every milligram of ammonia consumed during nitrification, 7.14 milligrams of CaCO₃ is consumed (Searce et al., 1980), hence a proper dosage of alkalinity should be included for the preparation of the synthetic water.

Table 19 summarizes the alkalinity requirements for this experiment.

Table 19: Alkalinity requirements for MBBSBR operation

NH₃-N (mg)	mg CaCO₃/mg NH₃-N	CaCO₃ mg (needed)	Water volume (L)	Alkalinity needed as [CaCO₃] (mg/l)
1.606	7.14	11.5	1.30	8.82

Table 19 is based on the calculated amount of ammonia nitrogen present at the beginning of the water treatment process. Since 7.14 mg of CaCO₃ is consumed per milligram of ammonia nitrogen, then 11.5 mg of calcium carbonate is needed to support nitrification, which translates into a needed alkalinity of 8.82 mg/l as [CaCO₃] (given the 1.3 L of synthetic water treated on each reactor).

To provide buffering capacity during the nitrification and keep it in a pH range between 7 and 7.5 for an 8-hour water treatment process, an excess of alkalinity of 27 mg/l (as

CaCO₃) was added by calcium carbonate (15 mg/l) and sodium bicarbonate (35 mg/L).

The total excess of alkalinity was calculated and presented in Table 20.

Table 20: Excess of alkalinity on MBBSBR for buffering at neutral pH

NH₃-N (mg)	Alkalinity needed as [CaCO₃] (mg/l)	[CaCO₃] added (mg/l)	[NaHCO₃] added (mg/l)	[NaHCO₃] added as [CaCO₃] (mg/l)	Alkalinity added as [CaCO₃] (mg/l)	Excess of Alkalinity as [CaCO₃] (mg/L)
1.61	8.82	15.00	35.00	20.83	35.83	27.01

Transformations from [CaCO₃] to [NaHCO₃] were done by equivalent weight:

EW of CaCO₃: Equivalent weight of Calcium Carbonate : 50.000 g/eq

EW of NaHCO₃: Equivalent weight of Sodium Bicarbonate : 84.006 g/eq

$$[\text{NaHCO}_3] = [\text{CaCO}_3] \frac{\text{EW of NaHCO}_3}{\text{EW of CaCO}_3}$$

5.1.5.8. Synthetic wastewater preparation

The synthetic wastewater was based on procedures followed by the Aquatic Microbiology Laboratory at Auburn University during the initial stages for fish tank acclimation prior to experimental execution and supported by literature as well (Hem et al., 1994). The recipe was based on ammonium chloride, calcium carbonate and sodium bicarbonate plus some trace elements that were incorporated by means of a low concentration marine salt solution (0.2%) that was prepared with an off the shelf marine salt *Seachem (Salt Mixed) Marine Salt* (Seachem, Inc., Madison, Ga). See chemical composition in Table 21.

**Table 21: Chemicals composition for Seachem (Salt Mixed) Marine Salt.
(Seachem Inc., 2018)**

Chemicals in Seachem (Salt Mixed) Marine Salt	Concentration in ppm
Chloride	19,336
Sodium	10,752
Sulfate	2,657
Magnesium	1,317
Potassium	421
Calcium	380
Carbonate/Bicarbonate	142
Strontium	9.5
Boron	0.2
Bromide	56
Iodide	0.06
Lithium	0.3
Silicon	<0.1
Iron	0.0098
Copper	0.0003
Nickel	<0.015
Zinc	0.0107
Manganese	0.0023
Molybdenum	0.0098
Cobalt	0.0004
Vanadium	<0.015
Selenium	<0.019
Rubidium	0.118
Barium	<0.04

The trace elements present in the marine salt solution are reported to be required for stimulating the nitrifying activity on *Nitrosomonas* and/or *Nitrobacter* (Hem et al., 1994).

Following the directions of the supplier, the salt solution was prepared with 340 grams of marine salt mixed in 10 liters deionized water and was left stirring overnight.

Stock water was prepared to replenish the reactors due to evaporation losses while nitrification didn't occur. The stock water was dechlorinated tap water that was conditioned with 224 uL of an off the shelf Tap Water Conditioner (Api Inc.) commonly used to dechlorinate aquarium waters.

The recipe for the preparation of the 17 L container with synthetic wastewater is shown in Table 22. During the acclimatization period, reactors ran 24 hours and water was replenished with stock water every morning by refilling it up to a 1.3 mark. Dosage 1 was implemented during preliminary experimentation and dosage 2 during formal experimentation.

Table 22: Synthetic water recipe for MBBSBR

Compound	Dosage 1	Dosage 2
Dechlorinated Water	17 L	17 L
CaCO ₃	255 mg	340 mg
NaHCO ₃	595 mg	595 mg
NH ₄ Cl	85 mg	170 mg
Salt solution	34 ml	34 ml

5.1.6. Bacterial inoculation process of the carriers

Prior to introducing the carriers into the reactors and over 2 months, carriers were exposed to bacterial inoculation and hence, biofilm formation. Four buckets (each one per carrier type) with 6 liters of synthetic wastewater were built up and inside of them, on the bottom, there were an air stone diffuser and a recirculation pump. Such pump

provided water flow to a basket containing a set of carrier type that remained hung to the interior of the same bucket.

1.5 mL of Nitromax (Tropical Science Biolabs, Inc), an off the shelf mix of living *Nitrosomonas* and *Nitrobacter* was inoculated into the four buckets the first day and 750 μ L every other day. Daily evaporation losses were replenished with dechlorinated water.

Ammonia, ammonium, nitrite, nitrate, pH, chlorine, hardness and alkalinity were visually inspected daily with test strips (6-in-1 Aquarium Test Strips & Ammonia Aquarium Test Strips, Tetra, Inc) for monitoring water quality status.

5.1.7. Acclimatization Process of the carriers in the reactors

Once biofilm formation was achieved, gyroids and K1s were placed into their respective reactors with synthetic wastewater. Reactors were placed in each water bath at 30°C, air diffusion was kept at 1 PSI on the pressure gauge, hence achieving 5-6 mg O₂/L in each reactor.

163 μ L of Nitromax were added at mornings to each reactor every other day. The daily inspection was performed with test strips, digital thermometer, pH and DO probes to make sure that the proper conditions for nitrification were optimal. Two weeks after the start of the acclimatization process and under the constant operation of the reactors with dechlorinated tap water replenishment, the whole system started to cycle and to produce nitrates.

5.1.8. Ammonia and Nitrate Determination

Ammonia and Nitrate were determined by colorimetry using YSI 9500 photometer that measured the color intensity of the sample after the addition of extra reagents. Determinations were done by triplicate from each reactor and three times during the run. Every run had 3 sampling process: at the beginning, at the middle and at the end of the process. Prior to each sampling process, reactors were put on idle for 30 minutes to let the water stand, the sampling process itself took 15 minutes. So, by the time when water samples were fully stored for later analysis, they corresponded to treatment process of 0 hours 45 minutes, 4 hours 45 minutes and 8 hours 45 minutes. However, for practical purposes, results were reported to nominal values of 0 hours, 4 hours and 8 hours of treatment.

For Ammonia determination the method was based on an indophenol method. Reagents came in two tablets that were added to the water sample and ammonia reacted with alkaline salicylate under the presence of chlorine to form a green-blue indophenol complex. The final color developed after mixing and settling was proportional to the ammonia concentration.

For Nitrate determination, nitrate was first reduced to nitrite by means of a flocculation process with a zinc-based Nitratetest Powder. After decanting, the clear supernatant produced a reaction between sulphanilic acid and N-(1-naphthyl)-ethylene diamine to form a reddish dye, whose color intensity was proportional to the nitrate concentration. Figure 50 shows the aspect of the water samples prior photometric reading.

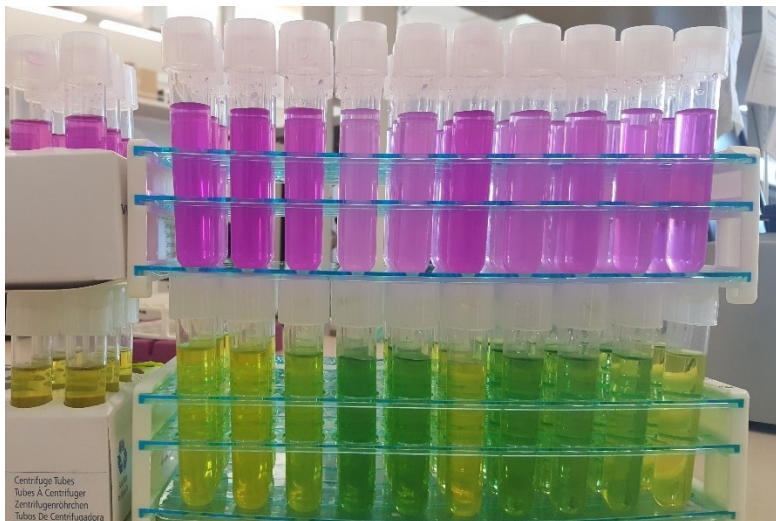


Figure 50: Water samples after the dosage of reagents for color development prior to photometric measurements.

5.1.9. Experimental Design

5.1.9.1. Methodology for hypothesis 1

To test hypothesis 1 that larger surface area generated on the 3D printed gyroid media carrier promotes faster ammonia nitrogen removal than a traditional media carrier, twelve 1.3-liter volume reactors treating synthetic wastewater were used in the lab scale water treatment system. A total of four levels of carriers were tested during experimentation. To test hypothesis 1, three runs were executed in three days. A run consisted of every 8-hour-water treatment process performed to test the hypothesis. Details of the experimental design are displayed in Table 23.

Table 23: Experimental design to test hypothesis 1

Treatment / carrier type	Replicates per treatment (reactors)	Volume of packed carriers (m³)	Surface area per carrier (m²)	Count per carrier type	Total surface area per treatment (m²)	Fill ratio (%)
K1	3	0.0002	0.0009	148	0.140	15
Small SSA gyroid	3	0.0002	0.0022	25	0.055	15
Medium SSA gyroid	3	0.0002	0.0042	25	0.106	15
Large SSA gyroid	3	0.0002	0.0083	25	0.207	15

The purpose of this design was to keep constant the volume of the carriers. For this to happen 200 mL (0.0002 m³) volume of each carrier type were packed into a glass beaker and then counted out. Same packing ratio, but different surface area levels were generated per treatment. Almost 100 times the calculated required volume in carriers was implemented for the treatment process for two reasons: 1) The visual aspect of the carriers didn't evidence a full colonization on the available surface area of the carriers. 2) 15% fill ratio got closer to some similar experiments found in the literature (Barwal & Chaudhary, 2015; Gu et al., 2014; Zhang et al., 2016)

5.1.9.2. Methodology for hypothesis 2

To test hypothesis 2 that the feature design of the 3D printed gyroid media carriers promoted faster TAN removal than traditional media carrier, a similar methodology was implemented, but instead of keeping constant the packing ratio of the biocarriers, the total surface area of the carriers was kept constant.

Once experimentation to test hypothesis 1 was completed, the same twelve 1.3-liter volume reactors treating the synthetic wastewater were used for the lab scale water treatment process to test hypothesis 2. As similar to hypothesis 1, three runs were executed in three days to test hypothesis 2. Four levels of carriers were tested during experimentation. Details of the experimental design are displayed in Table 24.

Table 24: Experimental design to test hypothesis 2

Treatment / carrier type	Replicates per treatment (reactors)	Volume of packed carriers (m³)	Surface Area per carrier (m²)	Count per carrier type	Total surface area per treatment (m²)	Fill ratio (%)
K1	3	6.91x 10 ⁻⁰⁵	0.0009	58	0.055	5
Small SSA gyroid	3	2.00x10 ⁻⁰⁴	0.0022	25	0.055	15
Medium SSA gyroid	3	1.04x10 ⁻⁰⁴	0.0042	13	0.055	8
Large SSA gyroid	3	5.30x10 ⁻⁰⁵	0.0083	7	0.055	4

An illustration to help to visualize the methodology to address each hypothesis is shown in Figure 51

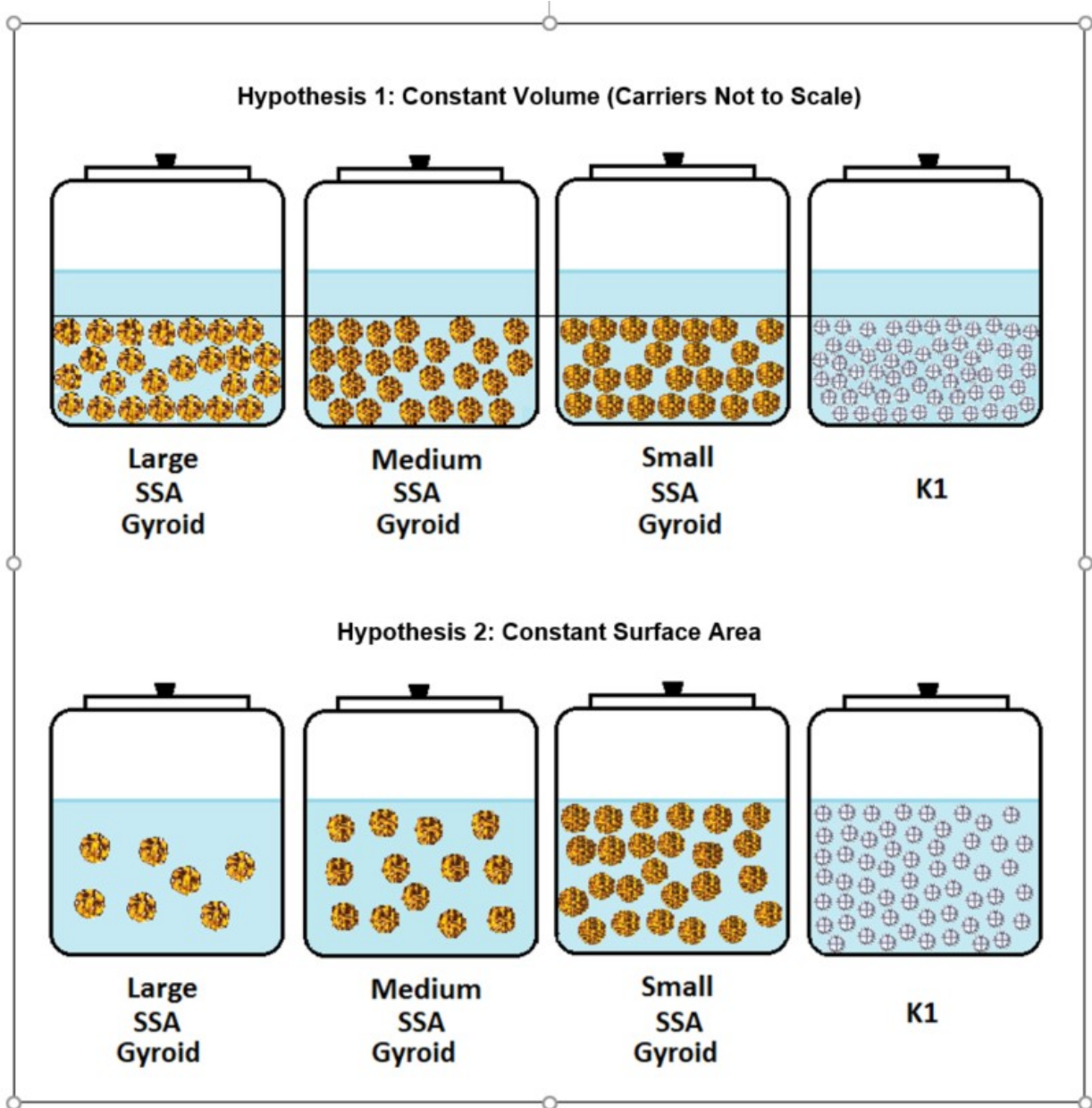


Figure 51: Illustration of Hypothesis 1 and Hypothesis 2

5.1.9.3. Randomization of the jars and carriers

To meet the workspace conditions of the laboratory where this experiment took place, two separate baths were placed on different workbenches and used to carry six reactors in each of them under experimental conditions. Even though sensitive parameters such as pH, DO concentration and temperature were constantly monitored for proper experimental setup, different randomized locations of the reactors were assigned in each run and throughout the execution of the whole experimentation to make sure no external or unknown factors were influencing the results of the experiments. Figure 52 shows the randomized locations of the reactors in every run. As mentioned earlier, three runs were executed to prove each hypothesis.

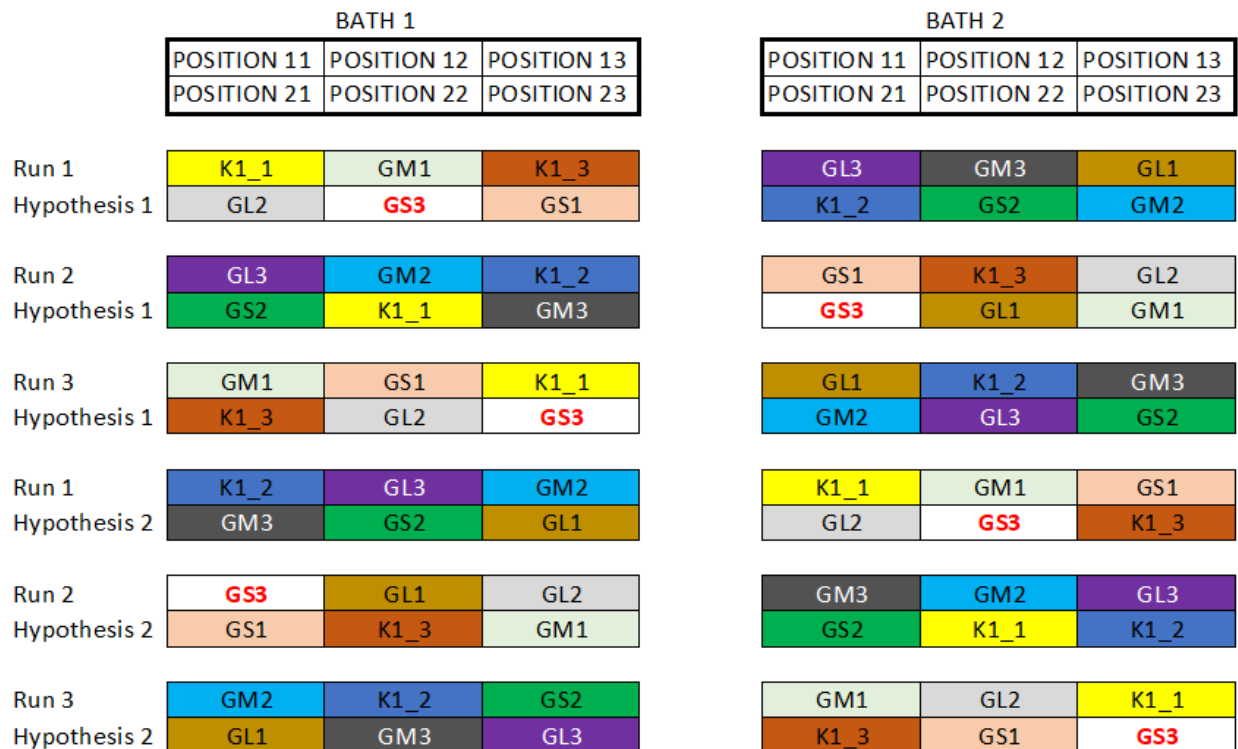


Figure 52: Randomized locations per run.
K1#: Kaldnes 1, **GS#:** gyroid small SSA, **GM#:** gyroid medium SSA, **GL:** gyroid low SSA,
#: treatment replicate

In a similar way, before every run, all carriers from the same type were put in a bag, mixed and replaced into their respective reactor type.

5.1.9.4. Protocol for experiment 2

Figure 53 shows the protocol for a single run for experiment 2. Three runs were needed to test hypothesis 1 and three more to test hypothesis 2. Note that prior to taking water samples, reactors were allowed to sit for 30 minutes. DO concentration, pH, and temperature measures were taken at the beginning and at the end of every run while drawing water samples. The water dechlorination process to prepare the synthetic wastewater was done 24 hours prior to use. Most of the water analyses were done with fresh samples (right after sampling). When this was not possible, samples were stored in the fridge for no longer than 48 hours. Once samples were taken back from the fridge for analysis, they were warmed to room temperature conditions prior to analysis.

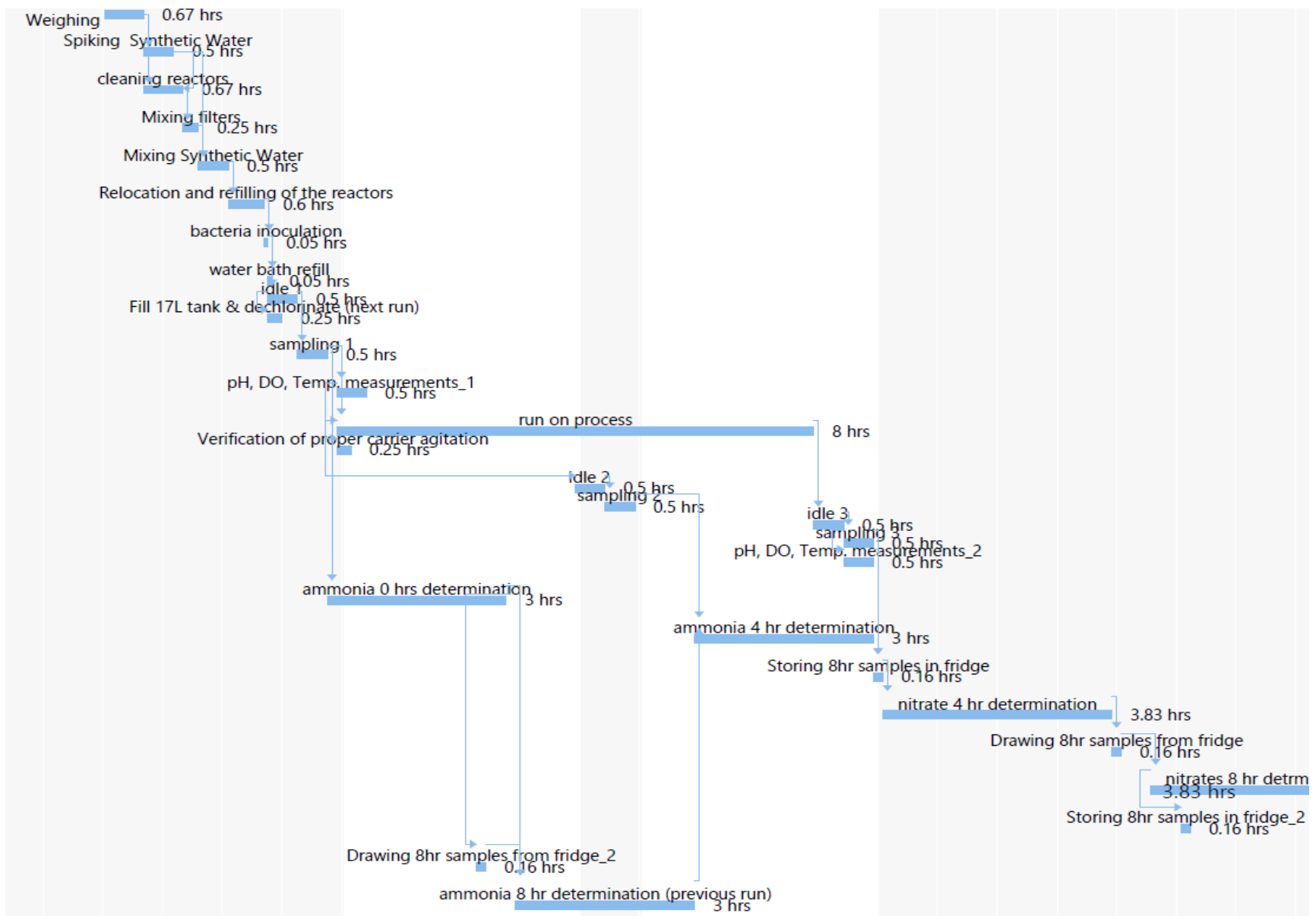


Figure 53: Workflow per run

5.2. Results

5.2.1. Preliminary results for hypothesis 1

During the first six runs of the preliminary experimentation, a single measurement was used to determine Ammonia-N and Nitrate-N, both at the beginning and at the end of each run. The error bars from Gyroid Medium SSA evidenced large variability on the replicated reactors for such treatment (see Figure 54), so it was decided to triplicate the number of measures to get the final determination, hence gaining reliability on the estimation. Additionally, from Run 7 on, all filter types were mixed in a bag and then redistributed in each reactor type prior to the start of a new run. With these two actions, error bars decreased.

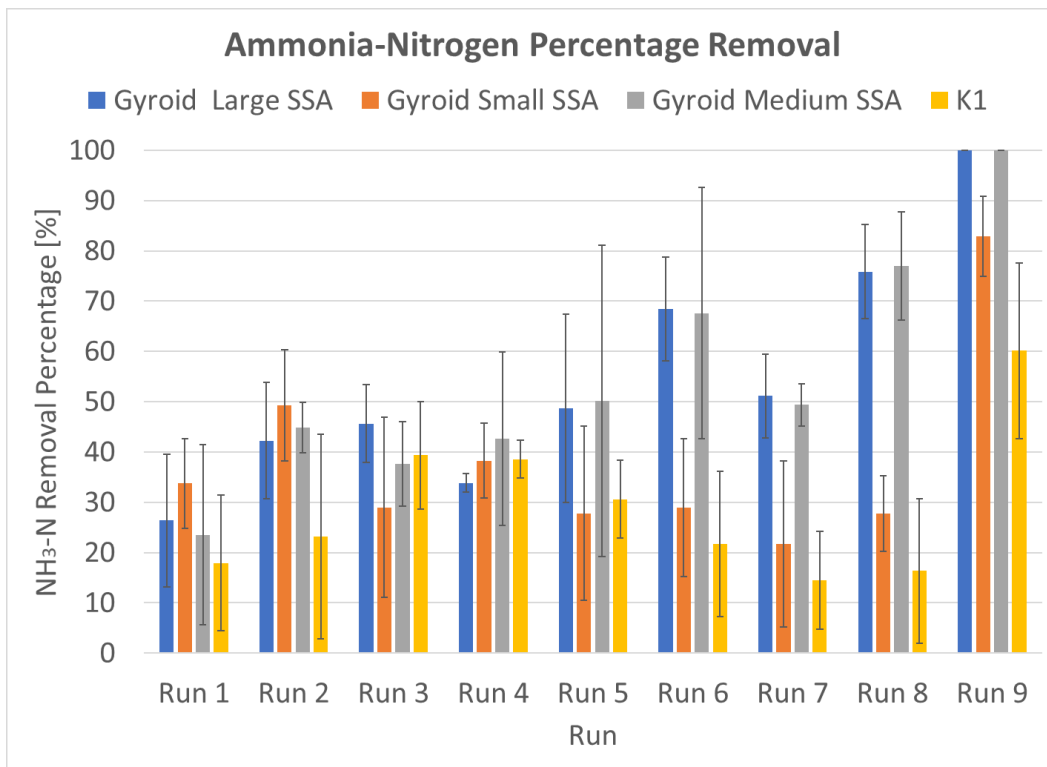


Figure 54: Ammonia-N Percentage Removal during the first nine 8 hour-runs. (Preliminary Results to test Hypothesis 1)

Run 7 and 8 both on ammonia percentage (Figure 54) removal and nitrate production (Figure 53) showed significantly greater performance for gyroid medium and large SSA than K1 and gyroid small SSA.

Figure 54 also shows no error bars both on gyroid medium and large SSA at Run 9 because by the time where samples were taken, 100% of ammonia-nitrogen removal was already achieved and readings were below the measuring range of the photometer when taken. For this reason, it was decided during formal experimentation to double the starting concentration of ammonium chloride and hence ammonia-nitrogen and also add an intermediate reading four hours after starting the run to have measurable substrate during the second and the final reading.

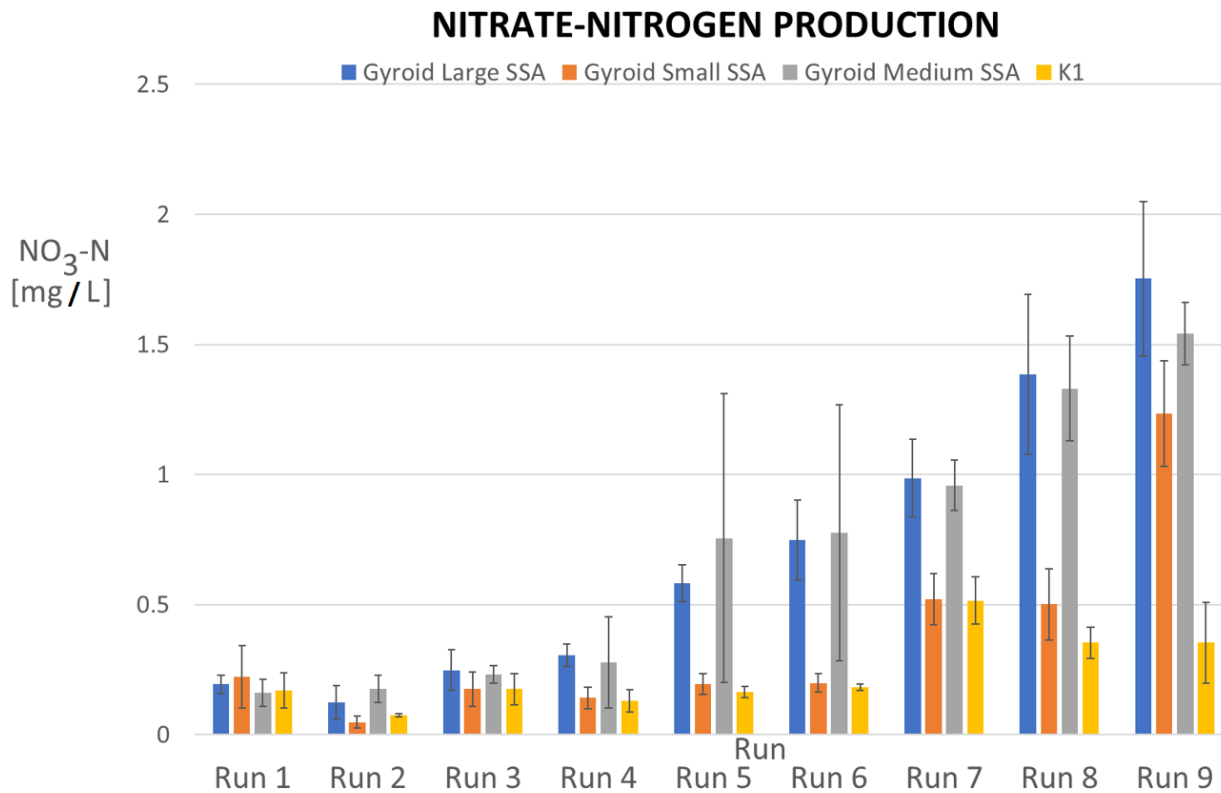


Figure 55: Nitrate-N production during the first nine 8 hour-runs. (Preliminary Results to test Hypothesis 1)

Both, Figure 54 and Figure 55 also evidenced increases in the ammonia nitrogen removal percentages and nitrate production levels run after run. It is possible that this gain was caused for the increased biofilm that was attached and kept growing on the walls of the carriers thus accelerating the ammonia removal and the production of nitrates.

Figure 56 shows separately the ammonia nitrogen and nitrates measures during run 7 and 8. Greater ammonia removal rates are evident for the gyroid medium and large SSA than the other two treatments. Similar observations are shown in the nitrate production rate. Gyroid medium and large SSA treatment show greater functionality than the other two treatments under conditions with the same packing ratio among treatments.

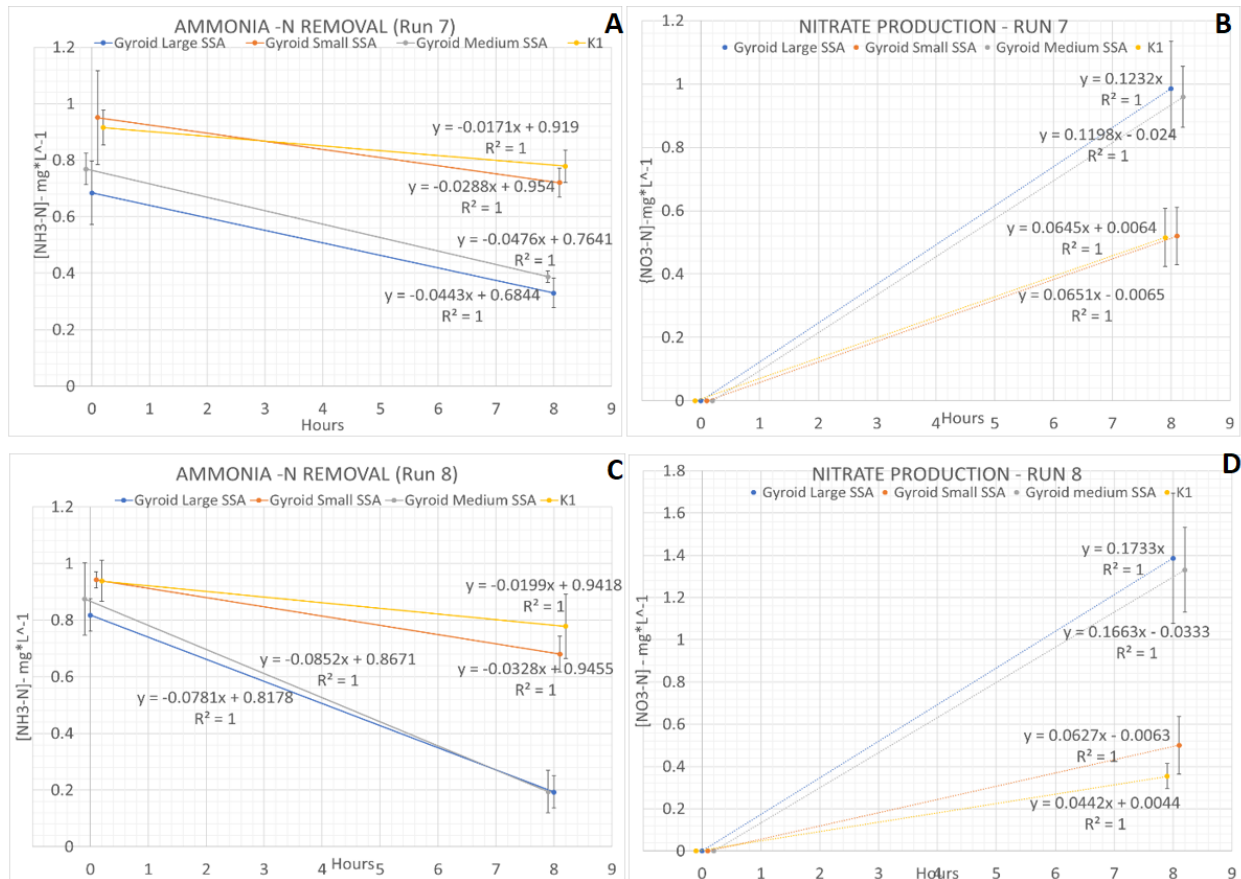


Figure 56: Raw Ammonia-N and Nitrate-N determination. In A) Ammonia-Nitrogen on Run 7, B) Nitrates-Nitrogen on Run 7, C) Ammonia-Nitrogen on Run 8, D) Nitrates-Nitrogen on Run 8. (Preliminary Results to test Hypothesis 1)

5.2.2. Results for hypothesis 1

5.2.2.1. Ammonia removal results for hypothesis 1

Three runs of water treatment processes were executed with the lab-scale MBBSBR. Water samples were analyzed at the beginning, middle, and end of the run. The addition of the intermediate reading in the middle of the run was to make sure enough ammonia was still measurable on the medium and large SSA treatments and avoid losing information due to total consumption as had happened when only one reading at the 8th hour was taken on the 9th run during preliminary experimentation.

At the start of the run, reactors were sampled by drawing 50 mL of water that was then analyzed for ammonia concentration. At the 4th and at the 8th hour of treatment, 100 mL water samples were taken to analyze for ammonia and nitrate content in triplicate. Figure 57, Figure 58 and

Figure 59 correspond to three experimental runs that showed the ammonia removal activity during the 8-hour treatment to test hypothesis 1. Two clusters of data were observed. Water samples from the medium and large specific surface area gyroid biocarrier presented consistently lower concentrations of ammonia than those from the K1 and low specific surface area gyroid media.

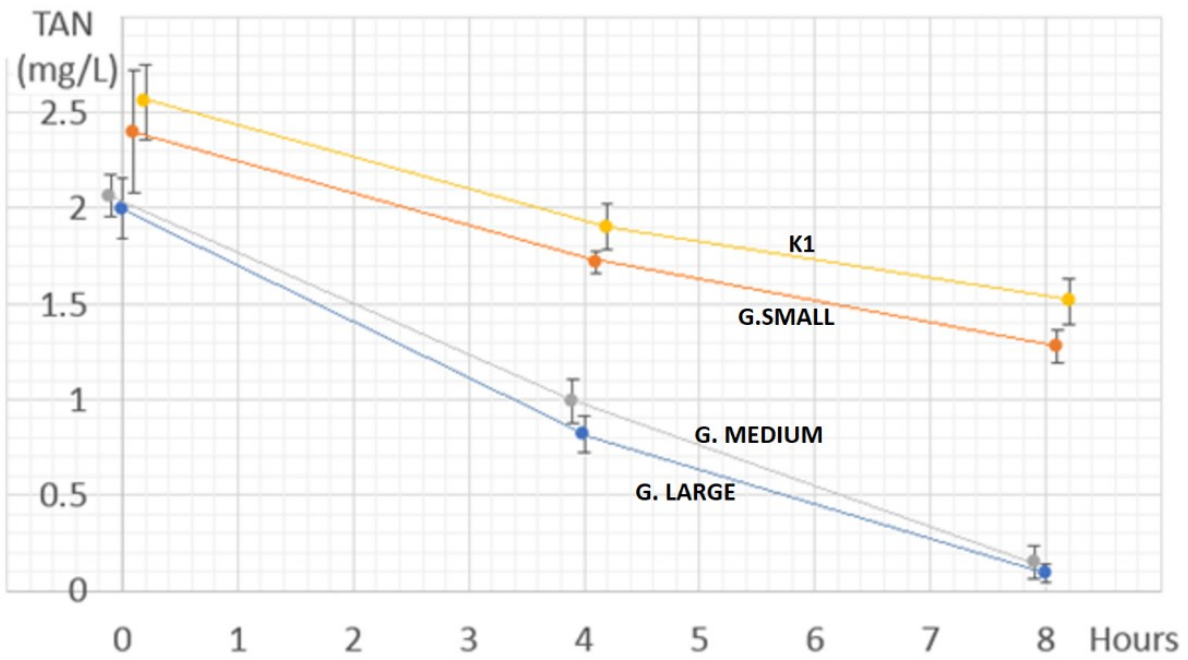


Figure 57: Ammonia concentration vs. time for run 1 (Hypothesis 1)
Error bars represent standard deviation (n=9)

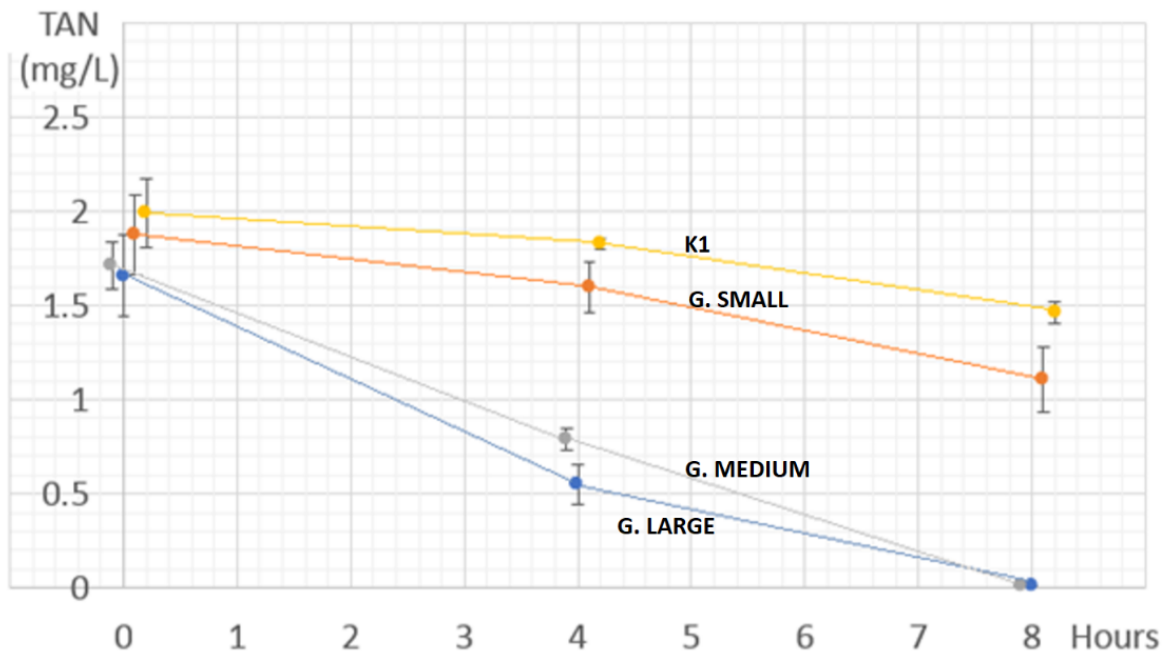


Figure 58: Ammonia concentration vs. time for run 2 (Hypothesis 1)
Error bars represent standard deviation (n=9)

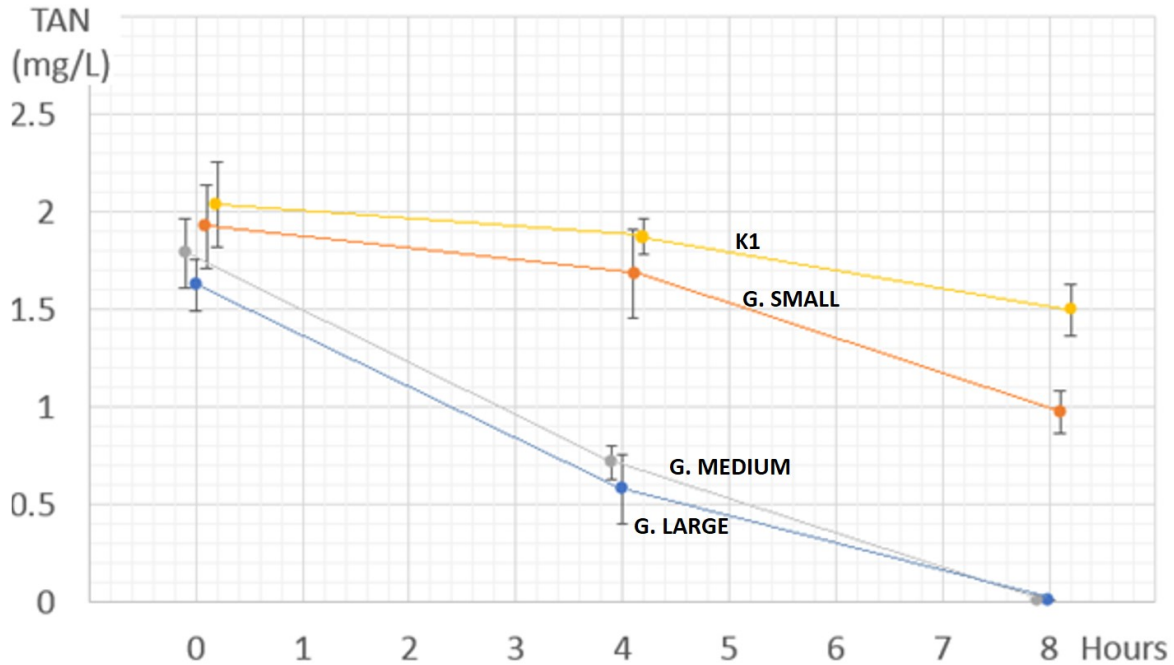


Figure 59: Ammonia concentration vs. time for run 3 (Hypothesis 1)
 Error bars represent standard deviation (n=9)

5.2.2.2. Nitrate production results for hypothesis 1

Water samples were analyzed for nitrates at the middle and at the end of the water treatment in triplicate. No water samples were taken at the beginning because it was expected to have nitrate concentrations close to zero or below the minimum level of detection of the photometer. This fact is supported by the chemical composition of the synthetic water and based on preliminary measures. Figure 60, Figure 61 and Figure 62 correspond to results from the three experimental runs to test hypothesis 1. The results showed increased concentrations of nitrate in all cases; however, two clusters of data were identified. Medium and large SSA gyroids appeared to produce significantly more concentration of nitrate in comparison to the two other treatments.

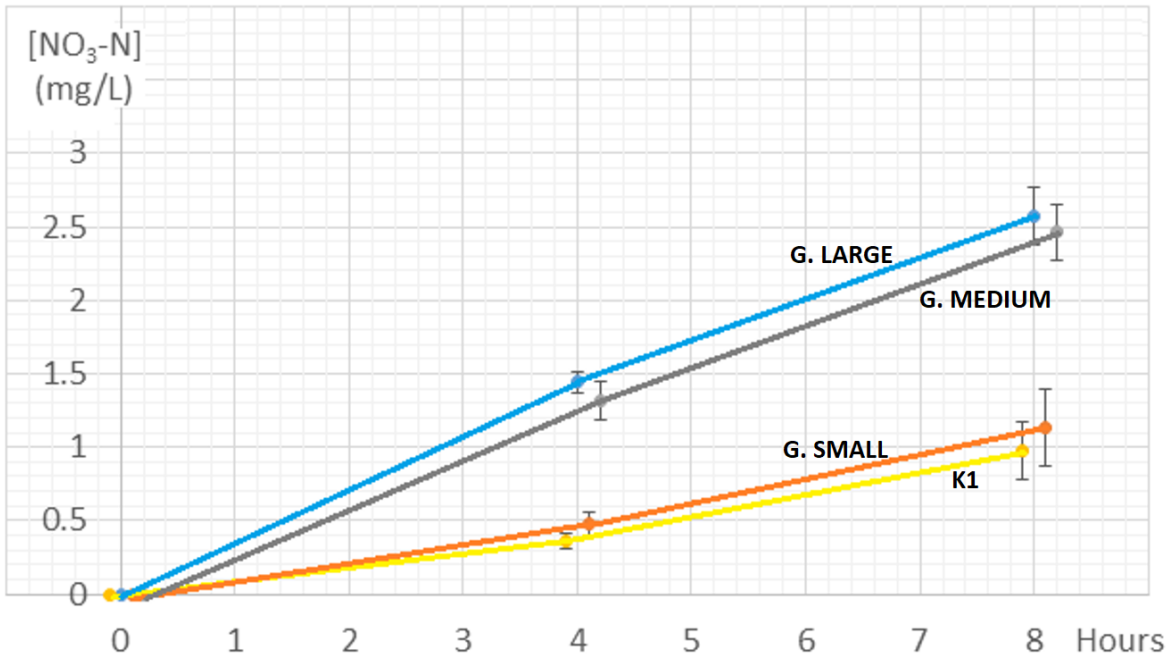


Figure 60: Nitrate concentration vs. time for run 1 (Hypothesis 1)
Error bars represent standard deviation (n=9)

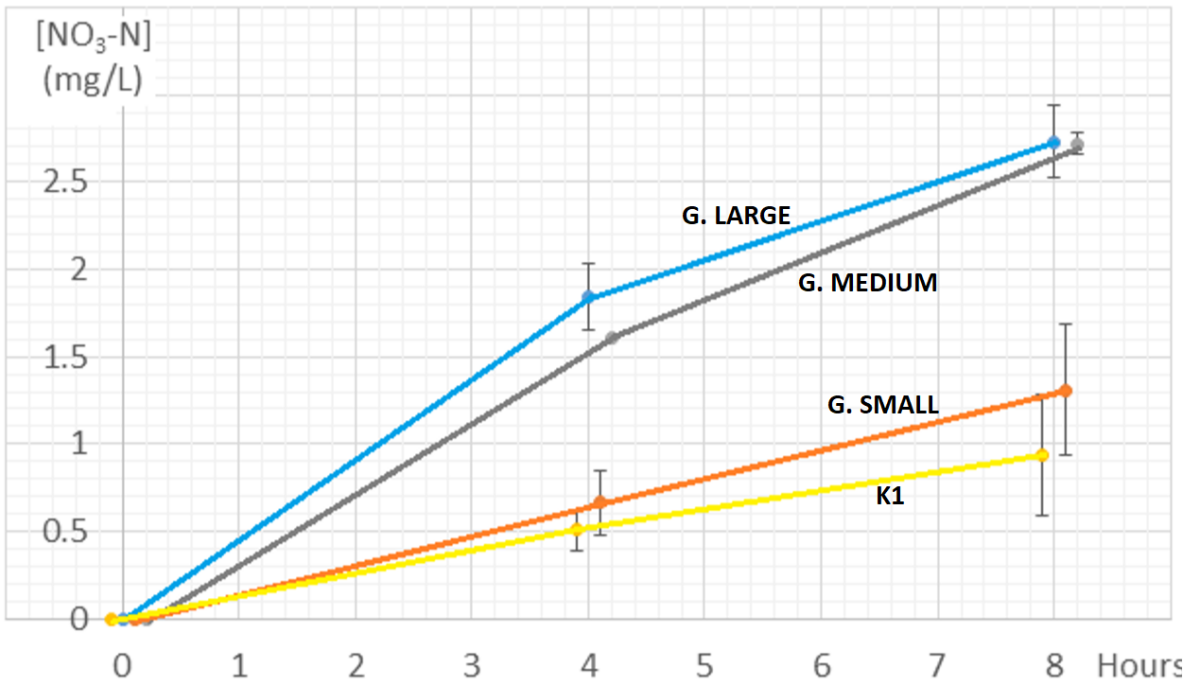


Figure 61: Nitrate concentration vs. time for run 2 (Hypothesis 1)
Error bars represent standard deviation (n=9)

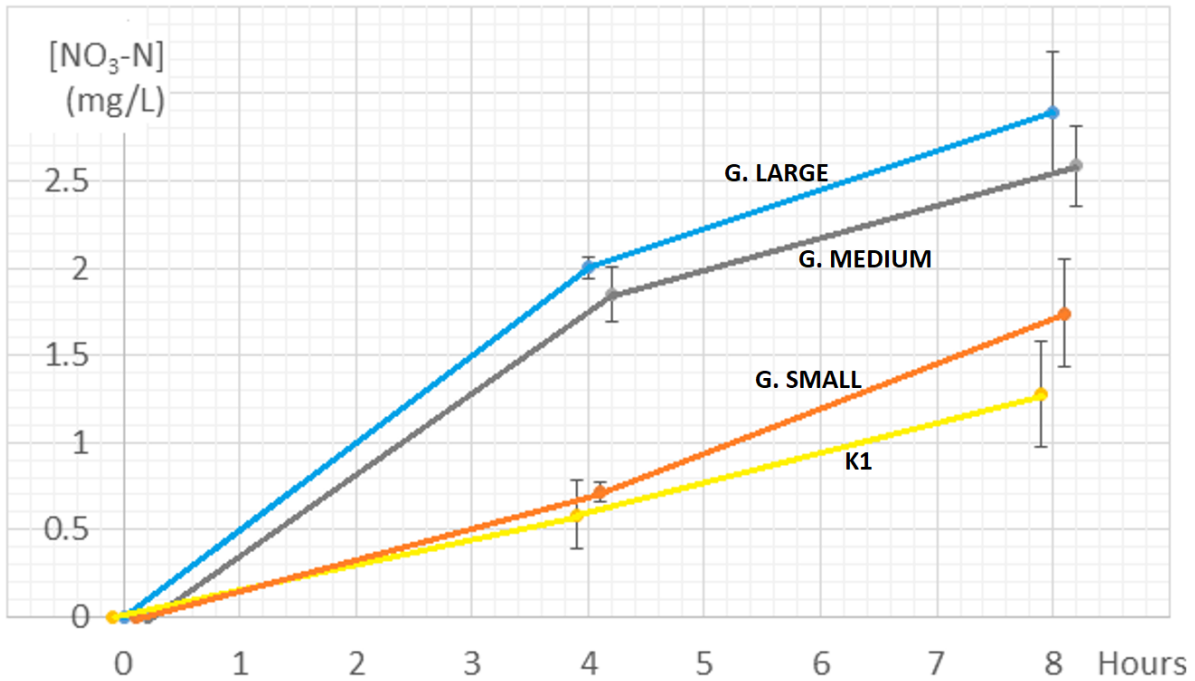


Figure 62: Nitrate concentration vs. time for run 3 (Hypothesis 1)
 Error bars represent standard deviation (n=9)

Data from run 1 to 3 to test hypothesis 1 were pooled. The results for ammonia removal are shown in Table 25 and plotted in Figure 63.

Table 25: Medians of the pooled total ammonia nitrogen (in mg/L) per treatment to prove hypothesis 1, and p values for Kolmogorov-Smirnov, Levene, Kruskal-Wallis and Mood's median test

Treatment / time (hours)	0	4	8
K1	2.2 ^a	1.85 ^a	1.50 ^a
Gyroid small SSA	2.1 ^a	1.65 ^a	1.14 ^a
Gyroid medium SSA	1.8 ^b	0.85 ^b	0.02 ^b
Gyroid large SSA	1.7 ^b	0.65 ^b	0.01 ^b
<i>p</i> (Normality test Kolmogorov-Smirnov)	*	*	*
<i>p</i> (Equal Variances Levene's test)	<0.010	<0.010	<0.010
<i>p</i> (Kruskal-Wallis)	*	*	*
<i>p</i> (Mood's median test) between medium with large SSA vs K1 with small SSA gyroid	0.000	0.047	0.000
	0.000	0.000	0.000

* $p \leq 0.05$ indicates non-normal distribution or non-equal variances

Treatments with the same symbol are not significantly different from each other, from Mood's median test, at a $p < 0.05$

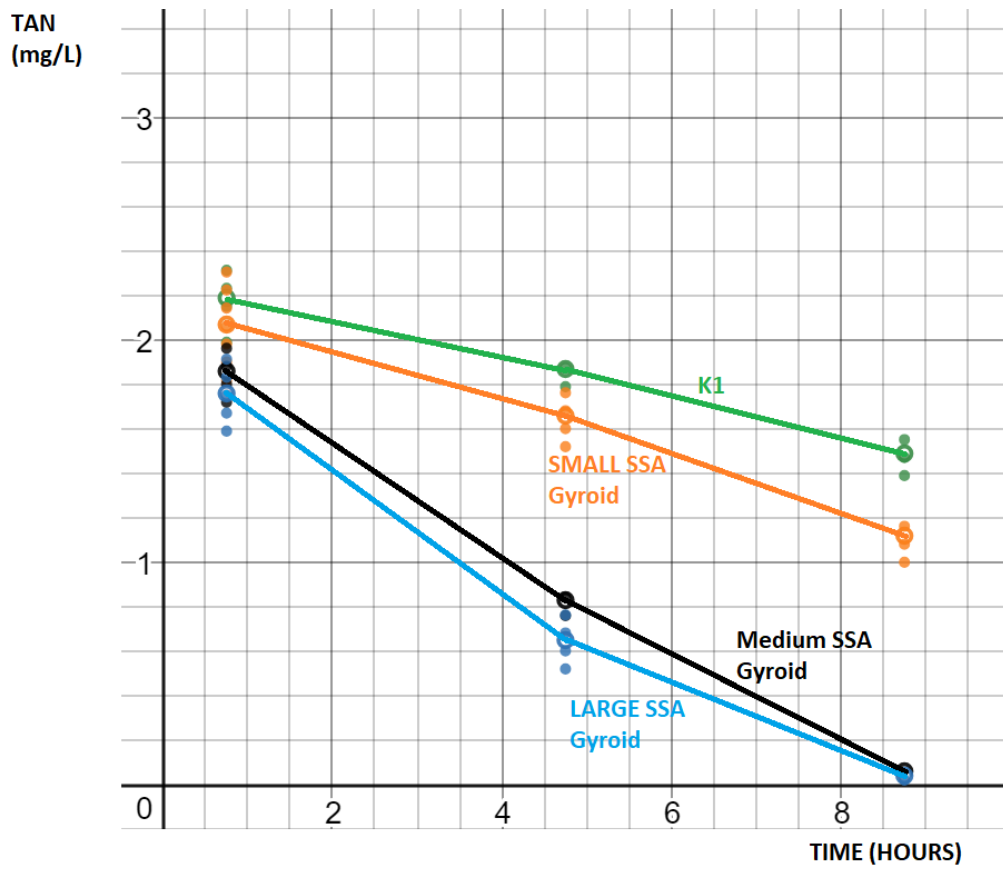


Figure 63: Pooled total ammonia concentration vs. time (Hypothesis 1)

Similarly, the pooled data for nitrate production are shown in Table 26 and plotted in Figure 64.

Table 26: Medians of the pooled nitrate nitrogen (in mg/L) per treatment to prove Hypothesis 1, and p values for Kolmogorov-Smirnov, Levene, Kruskal-Wallis and Mood's median test

Treatment / time (hours)	4	8
Gyroid large SSA	1.905 ^a	2.700 ^a
Gyroid medium SSA	1.590 ^a	2.560 ^a
Gyroid small SSA	0.605 ^b	1.420 ^b
K1	0.420 ^b	1.040 ^b
<i>p</i> (Normality test Kolmogorov-Smirnov)	*	*
	<0.010	<0.010
<i>p</i> (Equal Variances Levene's test)	*	*
	0.009	0.043
<i>p</i> (Kruskal-Wallis)	0.000	0.000
<i>p</i> (Mood's median test) between medium with large SSA vs K1 with small SSA gyroid	0.000	0.000

* $p < 0.05$ indicates non-normal distribution or non-equal variances

Treatments with the same symbol are not significantly different from each other, from Mood's median test, at a $p < 0.05$

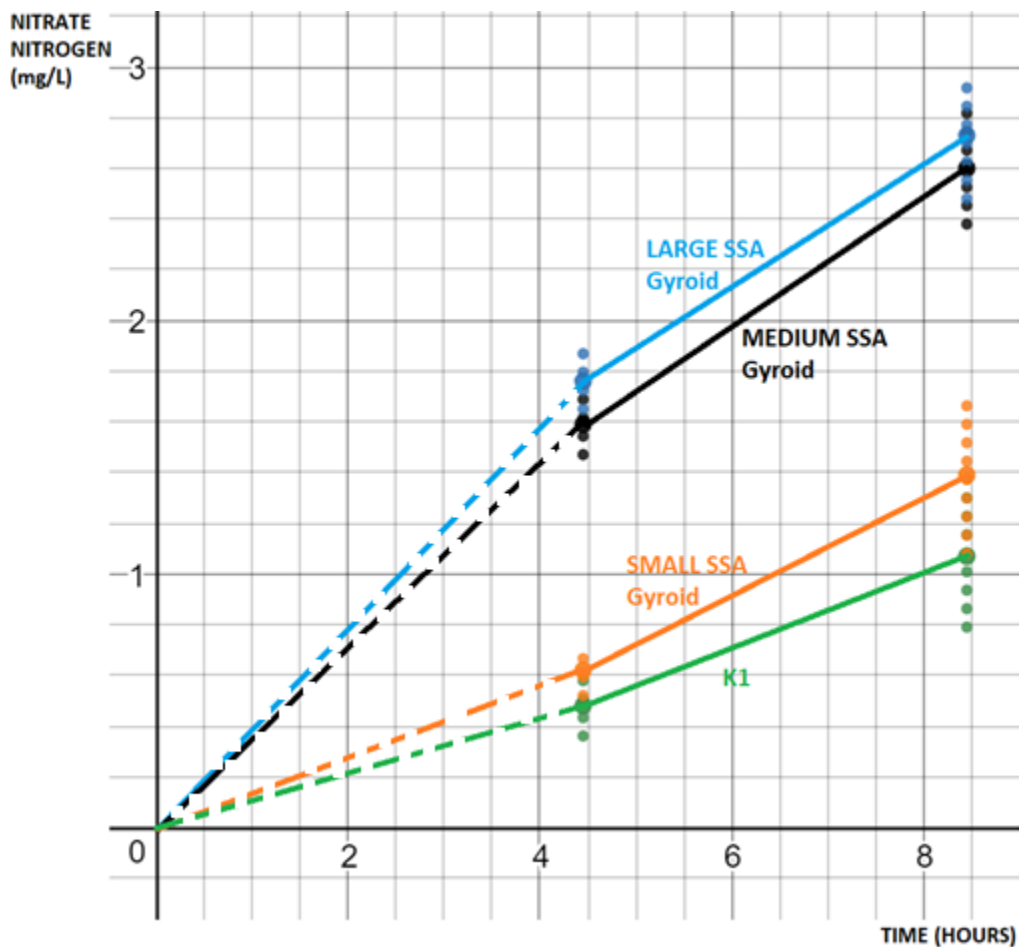


Figure 64: Pooled nitrate concentration vs. time production (Hypothesis 1)

For the calculation of ammonia removal percentage, the pooled ammonia concentration at the 8th hour was deducted from the concentration at the start of the water treatment, and the difference divided by the starting concentration of ammonia. Data of the means and standard deviations are shown in Table 28 and plotted in Figure 65.

Table 27: Medians of the pooled 8-hour total ammonia nitrogen removal percentage for each treatment (Hypothesis 1), and p values for Kolmogorov-Smirnov, Levene, Kruskal-Wallis and Mood's median and test

Treatment / time (hours)	Percentage of total ammonia nitrogen removed
Gyroid large SSA	99.33 ^a
Gyroid medium SSA	99.05 ^a
Gyroid small SSA	44.76 ^b
K1	30.00 ^b
<i>p</i> (Normality test Kolmogorov-Smirnov)	*
<i>p</i> (Equal Variances Levene's test)	*
<i>p</i> (Kruskal-Wallis)	0.000
<i>p</i> (Mood's median test) between medium with large SSA vs K1 with small SSA gyroid	0.000

* $p \leq 0.05$ indicates non-normal distribution or non-equal variances

Treatments with the same symbol are not significantly different from each other, from Mood's median test, at a $p < 0.05$

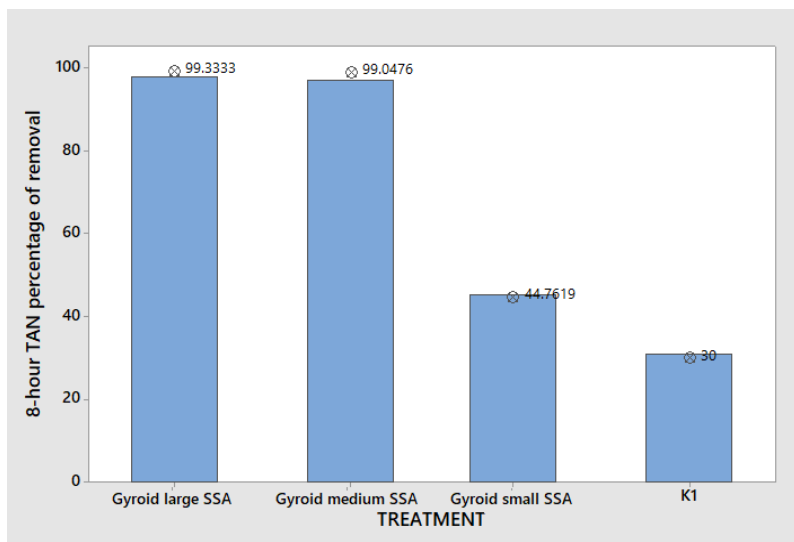


Figure 65: 8-hour TAN removal percentage for each biocarrier type for Hypothesis 1.

5.2.3. Results for hypothesis 2

5.2.3.1. Ammonia removal results for hypothesis 2

In the same way, as for hypothesis 1, water samples were drawn at the same time intervals. Figure 66,

Figure 67 and Figure 68 show the ammonia removal activity for testing hypothesis 2. Results appear to show a slight tendency for treatments with gyroids to remove ammonia at a greater rate than K1.

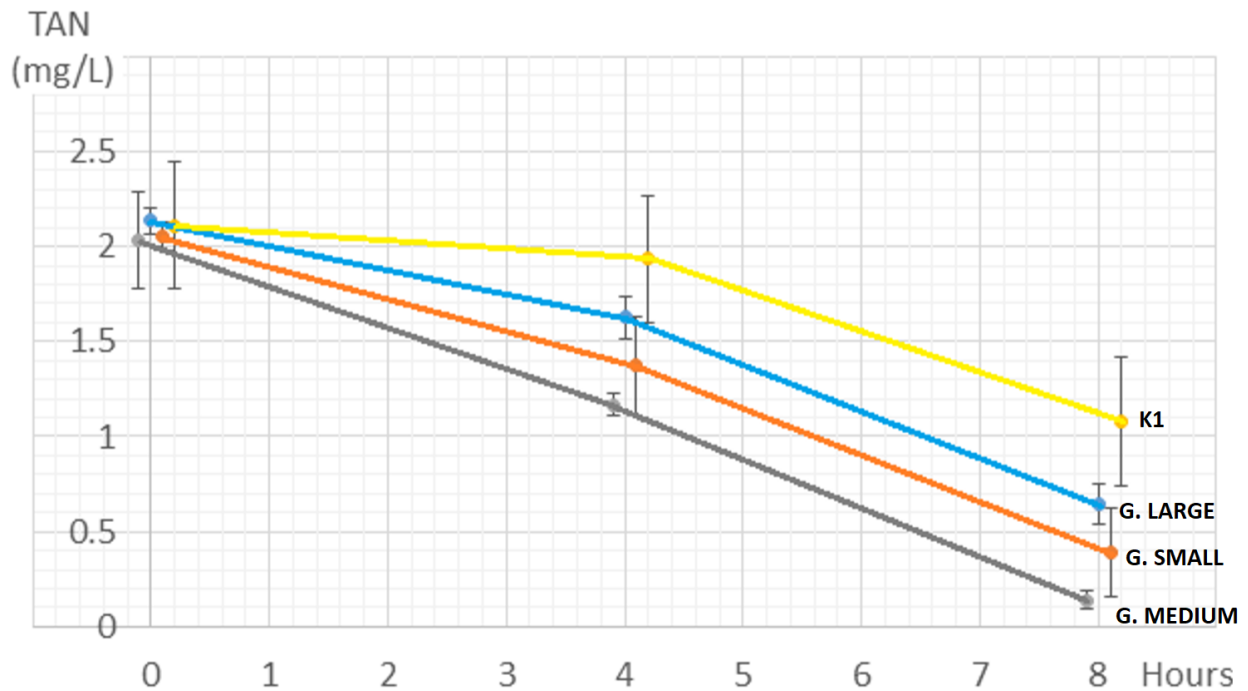


Figure 66: Ammonia concentration vs. time results for run 1 (Hypothesis 2)
Error bars represent standard deviation (n=9)

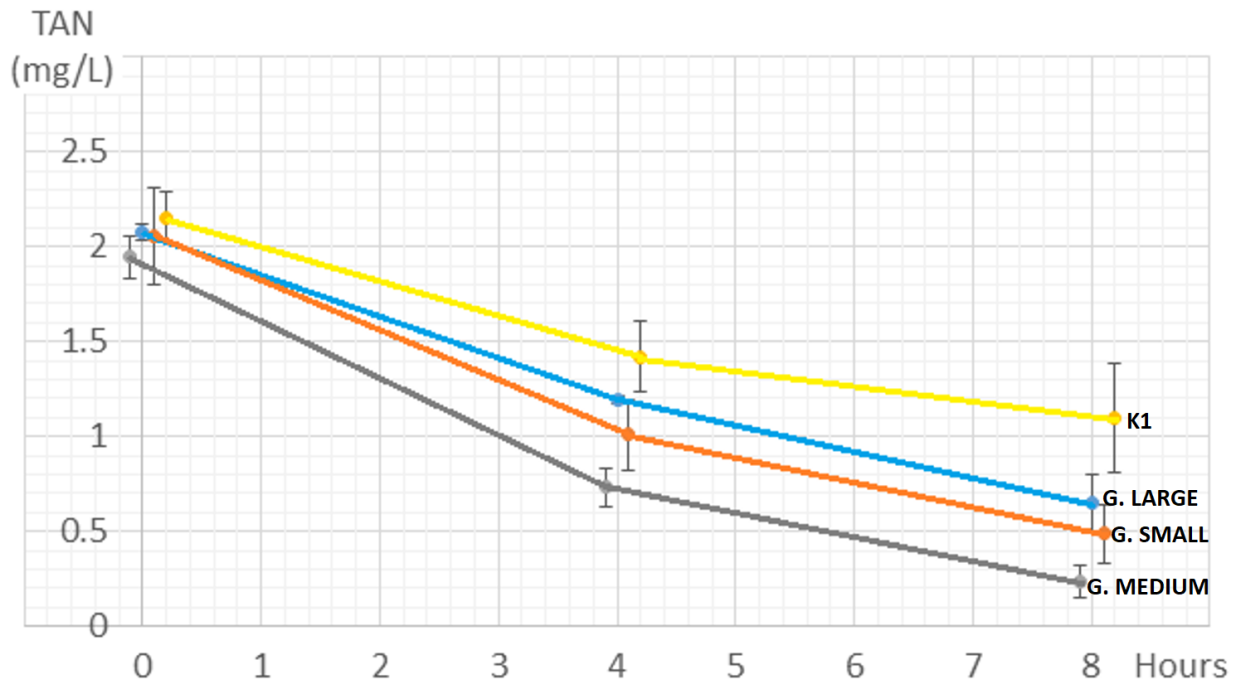


Figure 67: Ammonia concentration vs. time results for run 2 (Hypothesis 2)
Error bars represent standard deviation (n=9)

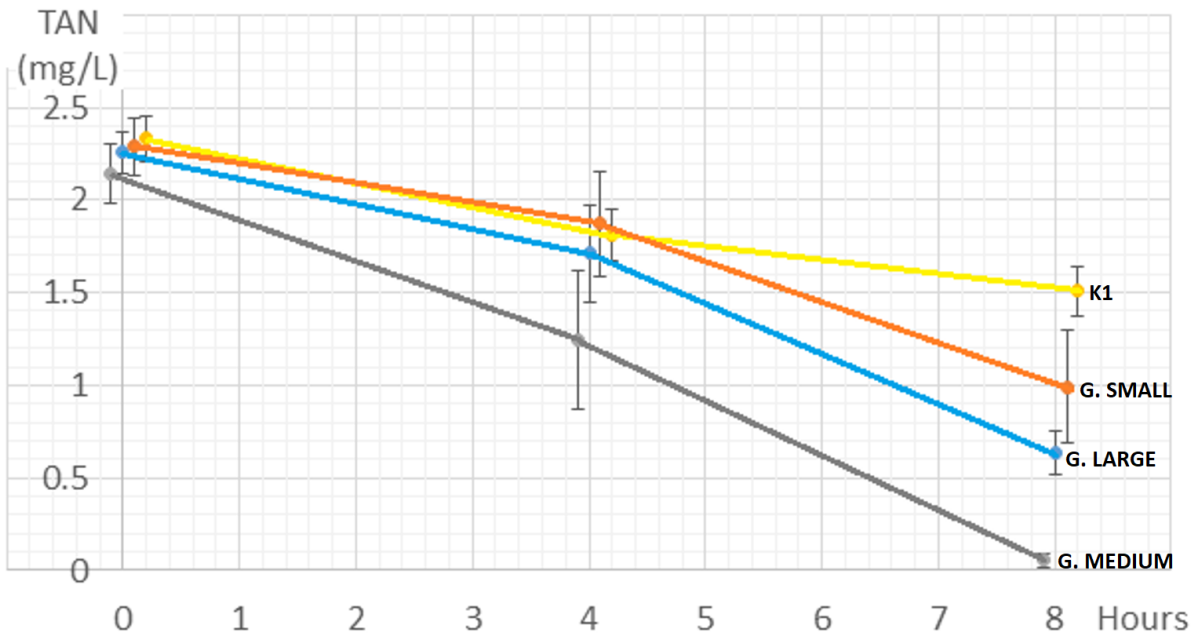


Figure 68: Ammonia concentration vs. time results for run 3 (Hypothesis 2)
Error bars represent standard deviation (n=9)

5.2.3.2. Nitrate production results for hypothesis 2

Figure 69, Figure 70 and Figure 71 are the results from the runs used for providing support to test hypothesis 2.

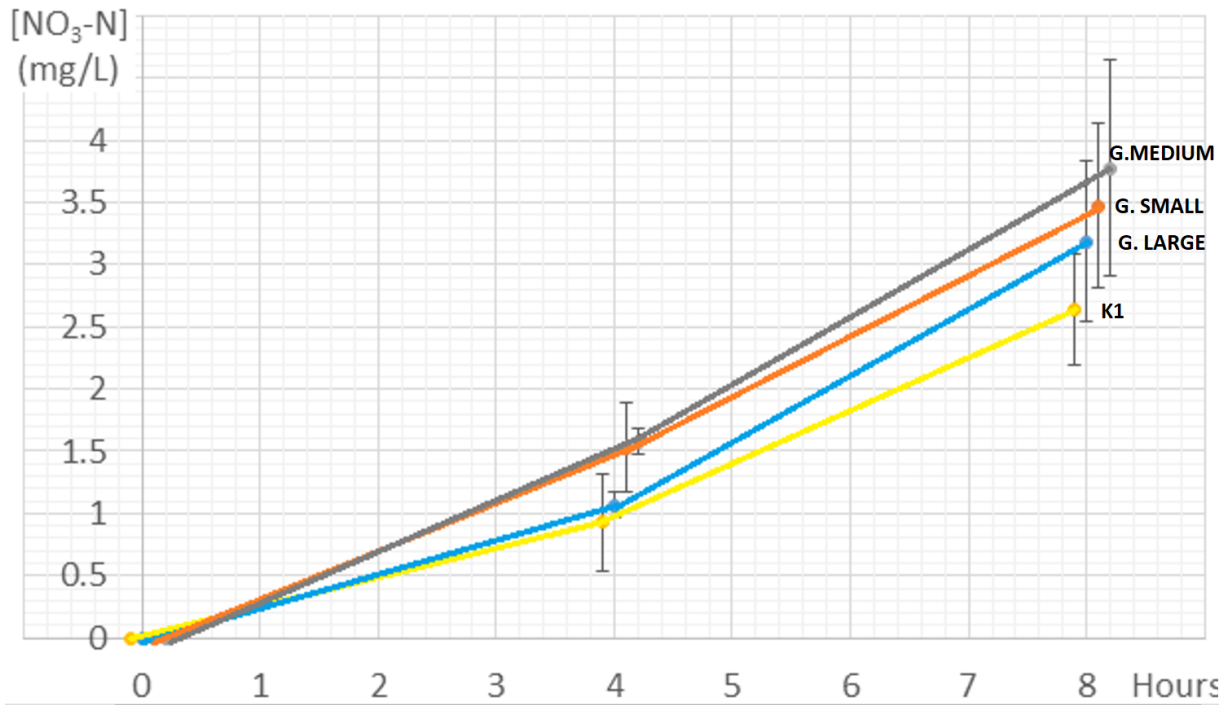


Figure 69: Nitrate concentration vs. time results for run 1 (Hypothesis 2)
Error bars represent standard deviation (n=9)

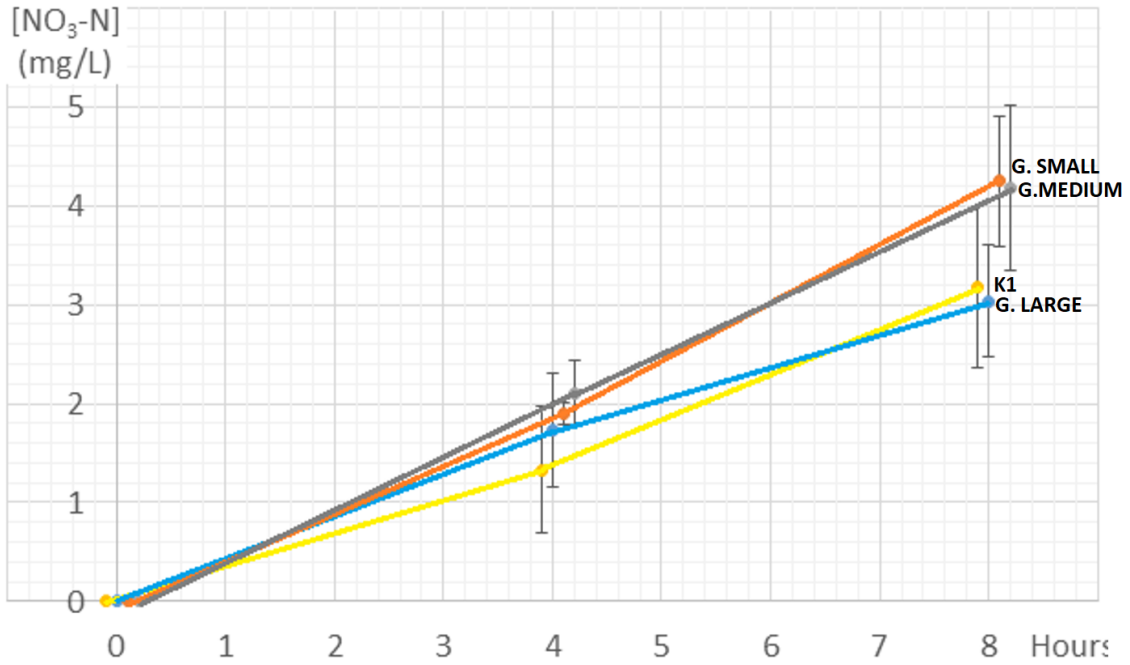


Figure 70: Nitrate concentration vs. time results for run 2 (Hypothesis 2)
 Error bars represent standard deviation (n=9)

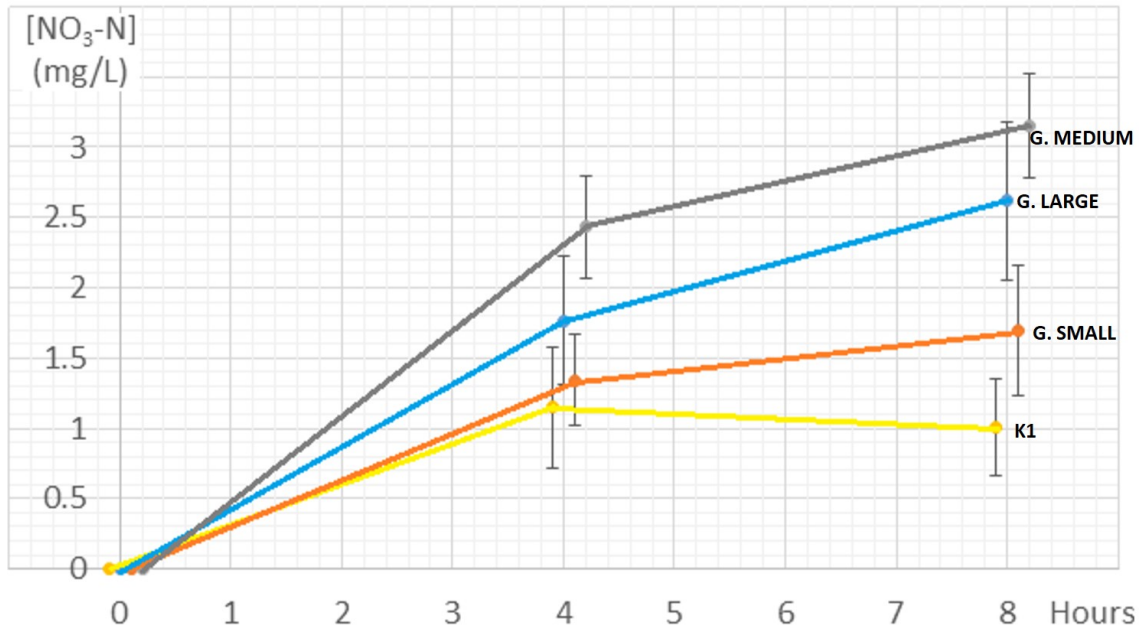


Figure 71: Nitrate concentration vs. time for run 3 (Hypothesis 2)
 Error bars represent standard deviation (n=9)

Data to test hypothesis 2, similarly to hypothesis 1, were pooled but grouped per carrier type (gyroids and K1). Results for ammonia removal are shown in Table 28.

Table 28: Medians of the pooled total ammonia nitrogen (in mg/L) per treatment to test hypothesis 2, and p values for Kolmogorov-Smirnov, Levene, Kruskal-Wallis and Mood's median test

Treatment / time (hours)	0	4	8
K1	2.20 ^a	1.68 ^a	1.32 ^a
Gyroid small SSA	2.10 ^b	1.50 ^b	0.60 ^b
Gyroid large SSA	2.10 ^b	1.50 ^b	0.68 ^b
Gyroid medium SSA	2.00 ^b	1.08 ^b	0.10 ^b
<i>p</i> (Normality test Kolmogorov-Smirnov)	*	*	*
	<0.010	<0.010	<0.010
<i>p</i> (Equal Variances Levene's test)	*		*
	0.004	0.067	0.000
<i>p</i> (Kruskal-Wallis)	0.003	0.000	0.000
<i>p</i> (Mood's median test between gyroids and k1)	0.005	0.000	0.000

* $p \leq 0.05$ indicates non-normal distribution or non-equal variances

Treatments with the same symbol are not significantly different from each other, from Mood's median test, at a $p < 0.05$

The pooled results per each carrier type were plotted on Figure 72.

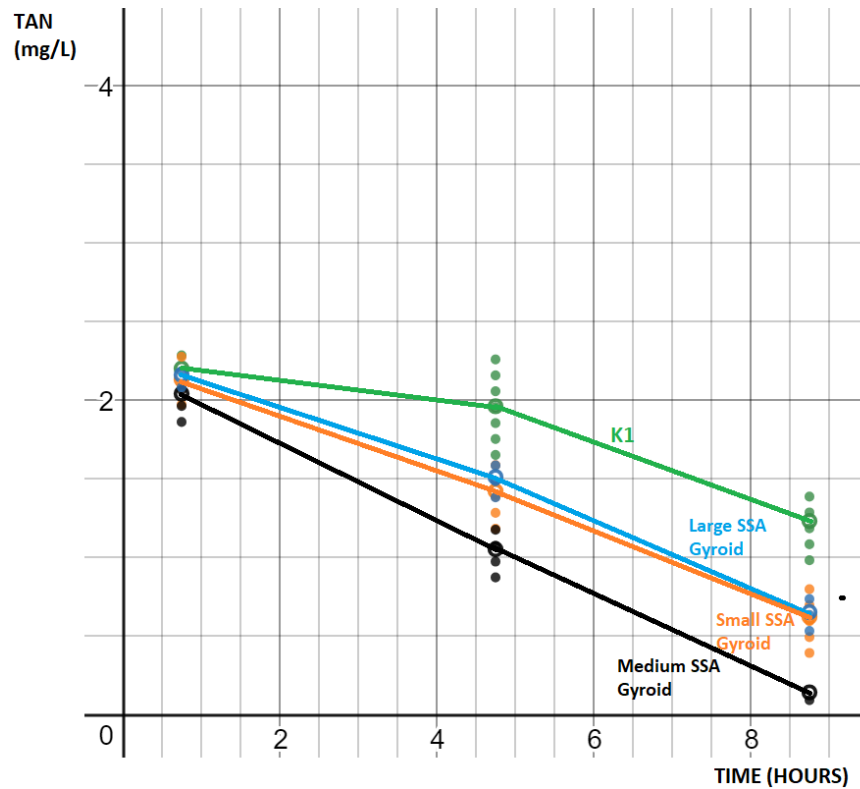


Figure 72: Pooled ammonia concentration vs. time (Hypothesis 2)

The pooled data but grouped per carrier type (gyroids and K1) for nitrates production are shown in Table 29.

Table 29: Medians of the pooled nitrate nitrogen (in mg/L) per treatment for Hypothesis 2, and p values for, Kolmogorov-Smirnov, Levene, Kruskal-Wallis and Mood's median test.

Treatment / time (hours)	4	8
Gyroid medium SSA	1.896 ^a	3.380 ^a
Gyroid small SSA	1.516 ^a	3.600 ^a
Gyroid large SSA	1.352 ^a	2.870 ^a
K1	1.204 ^b	2.220 ^b
<i>p (Normality test Kolmogorov-Smirnov)</i>	>0.150	0.122
<i>p (Equal Variances Levene's test)</i>	0.865	0.003 [*]
<i>p (Kruskal-Wallis)</i>	0.000	0.000
<i>p (Mood's median test) between gyroids and K1</i>	0.001	0.015

* $p \leq 0.05$ indicates non-normal distribution or non-equal variances among treatments. Treatments with the same symbol are not significantly different from each other, from Mood's median test, at a $p < 0.05$

The pooled results per each carrier type (K1, small, medium and large SSA gyroid) were plotted on Figure 73.

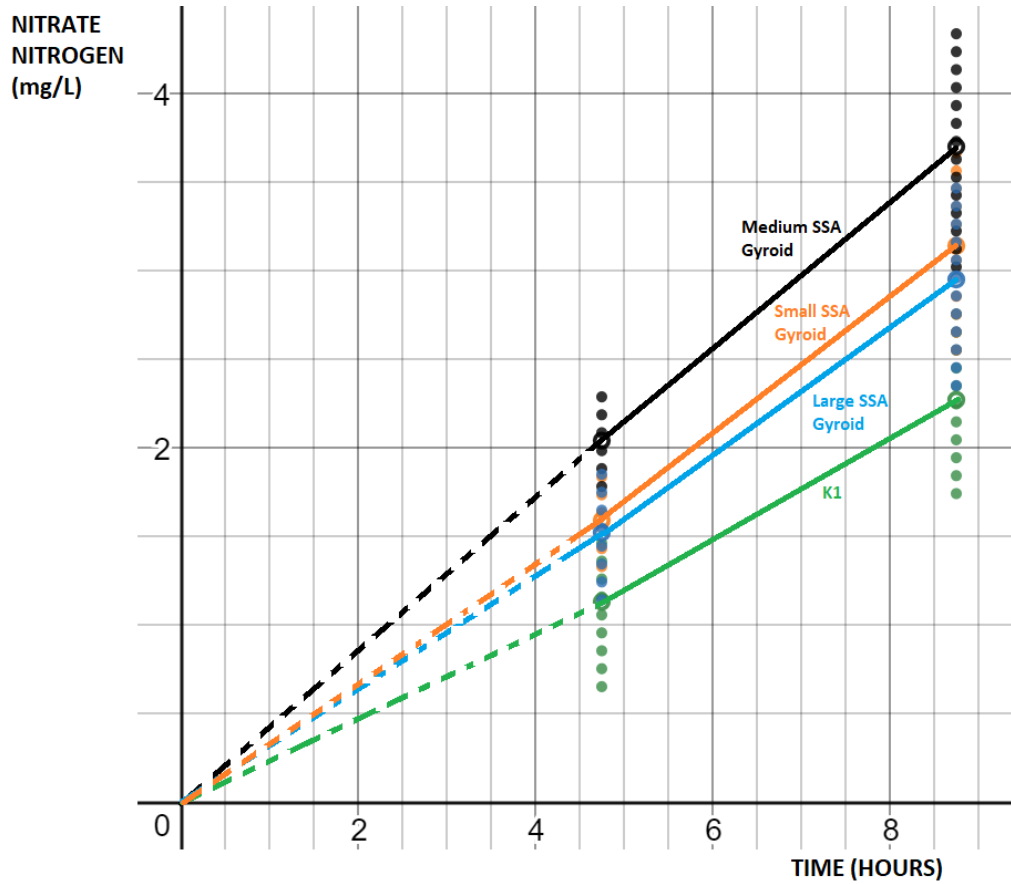


Figure 73: Pooled nitrate concentration vs. time (Hypothesis 2)

For the calculation of ammonia removal percentage, the pooled ammonia concentration at the end of the treatment was deducted from the concentration at the beginning of the water treatment and the difference divided by the starting concentration of ammonia. Data of the median percentages are shown in Table 30 and plotted in Figure 74.

Table 30: Medians of the percentage of ammonia removal for each treatment (Hypothesis 2), and p values for ANOVA, Kolmogorov-Smirnov, Levene and Kruskal-Wallis test

Treatment / time (hours)	Percentage of total ammonia nitrogen removed
Gyroid medium SSA	94.74 ^a
Gyroid small SSA	71.43 ^a
Gyroid large SSA	68.18 ^a
K1	40.00 ^b
<i>p</i> (Normality test Kolmogorov-Smirnov)	*
	<0.010
<i>p</i> (Equal Variances Levene's test)	*
	0.000
<i>p</i> (Kruskal-Wallis)	0.000
<i>p</i> (Mood's median test) between gyroids vs K1	0.000

* $p \leq 0.05$ indicates non-normal distribution or non-equal variances among treatments. Treatments with the same symbol are not significantly different from each other, from Mood's median test, at a $p < 0.05$

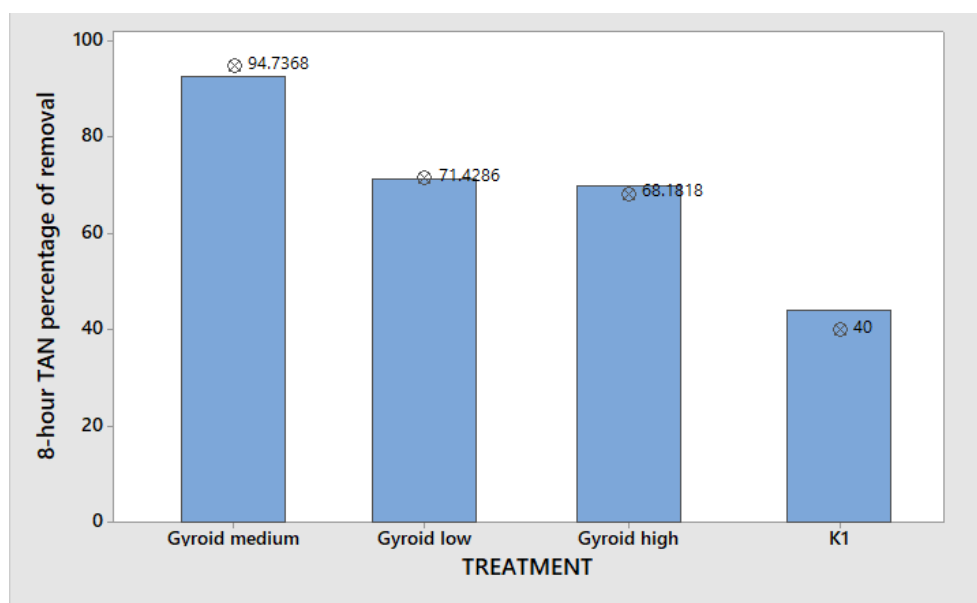


Figure 74: 8-hour TAN removal percentage for Hypothesis 2.

5.3. Discussion

Results to test hypothesis 1 appear to show a strong predominance from gyroids with medium and large specific surface area to remove significantly more ammonia than the commercial K1 and the gyroid with small specific surface area ($p=0.000$). These results are consistent with the proposed hypothesis 1 given that by using the same filling ratio (same volume of carriers) in all treatments, implicitly those treatments with the larger specific surface area were providing more surface area than those with smaller ones. This is because suspended bacteria in the synthetic water treated inside the reactors have a more available surface area to attach and develop their nitrifying activity than on those treatments with less SSA. This fact confirms that specific surface area is a main parameter for maximizing the performance of MBBRs (Barwal & Chaudhary, 2014).

From the same results to test hypothesis 1, the percentage of removal by the best treatments was almost 100% of the ammonia present in their reactors within 8 hours, while the other two treatments did not convert half of the ammonia present.

It was observed that the amount of ammonia removed and the specific surface area per carrier type were related to each other. Such relationship was identified between the treatments with small and medium SSA gyroids. In such treatments, the removed ammonia by the medium SSA was approximately two times the ammonia removed by the small SSA, which corresponds with the doubled SSA that medium SSA gyroids have.

The removal performance of ammonia was not always correlated with the specific surface area per carrier type. For example, the amount of ammonia removed by K1 was not larger than the amount of ammonia removed by the medium or smaller SSA gyroids, even though the SSA of the K1 ($1519 \text{ m}^2/\text{m}^3$) is nominally larger than the other two (1013 and

524 m²/ m³ respectively). However, the ammonia removed by the K1 carrier type was consistent with its effective biofilm surface area of 500 m²/m³ and even closer if 300 m²/m³, as advertised by the manufacturer, is used (Rusten et al., 2006). The reason why the biofilm-specific surface area from K1 does not match with the estimation performed by using the reverse engineering approach is that the latter one estimates the overall surface area of the carriers no matter if favors the biofilm attachment.

The amount of ammonia removed by the medium and large SSA gyroid types was the same for each of them (close to 100% of ammonia removal) when the same volume of carriers occupied inside the reactors. This fact suggests that there is probably a limiting condition that prevents a continued increase in ammonia removal rate despite the increased SSA. (Chen et al., 2015) suggested that when the biocarrier pore size is too small, such as in the case of the large surface area gyroid, it results in slower rates of substrate and oxygen transport to inner regions inside the voids. This might apply to the large SSA, which has the smallest pore sizes type, preventing the increase in performance to remain proportional to the increase in SSA.

In addition to the removal activity of ammonia, it was also possible to measure the concentration of produced nitrates for all treatments. A similar trend was observed as in the case of ammonia, where gyroids with medium and large surface area produced nitrates at a greater rate than small SSA gyroid and K1.

By comparing the amount of ammonia removed and the produced nitrates over time, it was possible to identify that, within the error of measurement, there is a conservation of nitrogen within the process. This means that the nitrogen present as ammonia was fully converted to nitrate (for the medium and large SSA), and for the case of the small SSA

gyroid and the K1, which did not deplete all the ammonia, the amount of ammonia nitrogen that was consumed matched the amount of nitrate nitrogen.

For the analysis of ammonia and nitrate, data can be fitted with a logistic curve function where the parameters can be selected in such a way that the initial concentration of ammonia and nitrate meet the nitrogen mass balance conditions. Upon that, a family of depletion curves (for ammonia analysis) were generated (See Figure 75). Different removal rates can be observed in the curve fitting. Table 31 shows the obtained expression for the logistic curve fitting, demonstrating the predominance of the medium and large SSA gyroids over the other two treatments quantified by means of the removal rate. By this analysis, the medium and large SSA gyroids exceeded the double the ammonia removal rate than the other two treatments when the volume of carriers was kept constant inside the reactors.

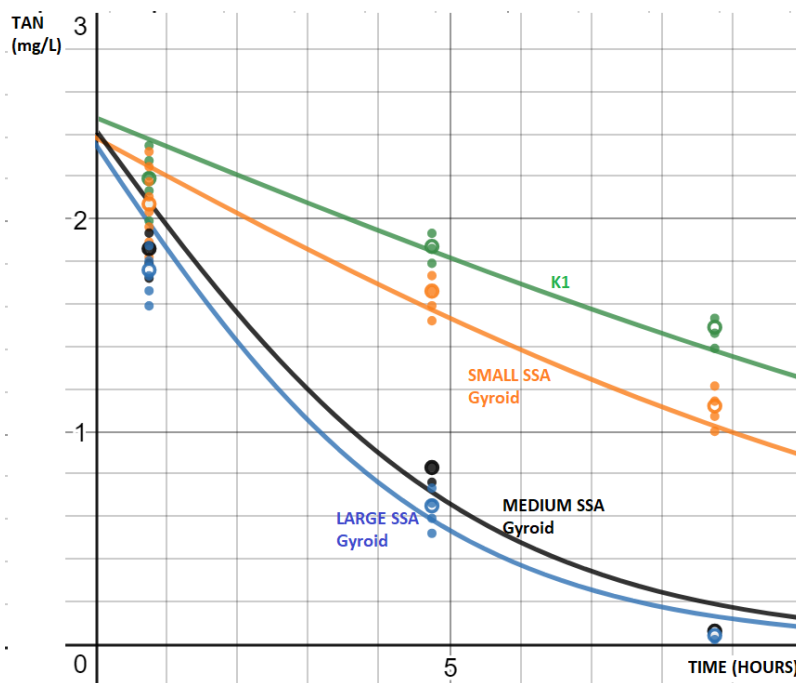


Figure 75: Total ammonia nitrogen results fitted in a logistic curve (Hypothesis 1)

Table 31: Logistic curve fitting for ammonia removal on hypothesis 1

Treatment	Logistic Function	Removal rate (mg/L/hours)	R ²
Large SSA gyroid	$S(t) = \frac{5}{1 + 1.13e^{0.40t}}$	0.40	0.9861
Medium SSA gyroid	$S(t) = \frac{5}{1 + 1.07e^{0.36t}}$	0.36	0.9834
Small SSA gyroid	$S(t) = \frac{5}{1 + 1.10e^{0.14t}}$	0.14	0.9865
K1	$S(t) = \frac{5}{1 + 1.02e^{0.11t}}$	0.11	0.9617

Similarly, as for ammonia, data from nitrate production for hypothesis 1 were fitted with a logistic curve (see Figure 76). Table 32 shows the obtained expressions for the logistic curve fitting, demonstrating the predominance of the medium and large SSA gyroids over the other two treatments by doubling the nitrate production rates (0.95 and 1.00 mg/L/hour).

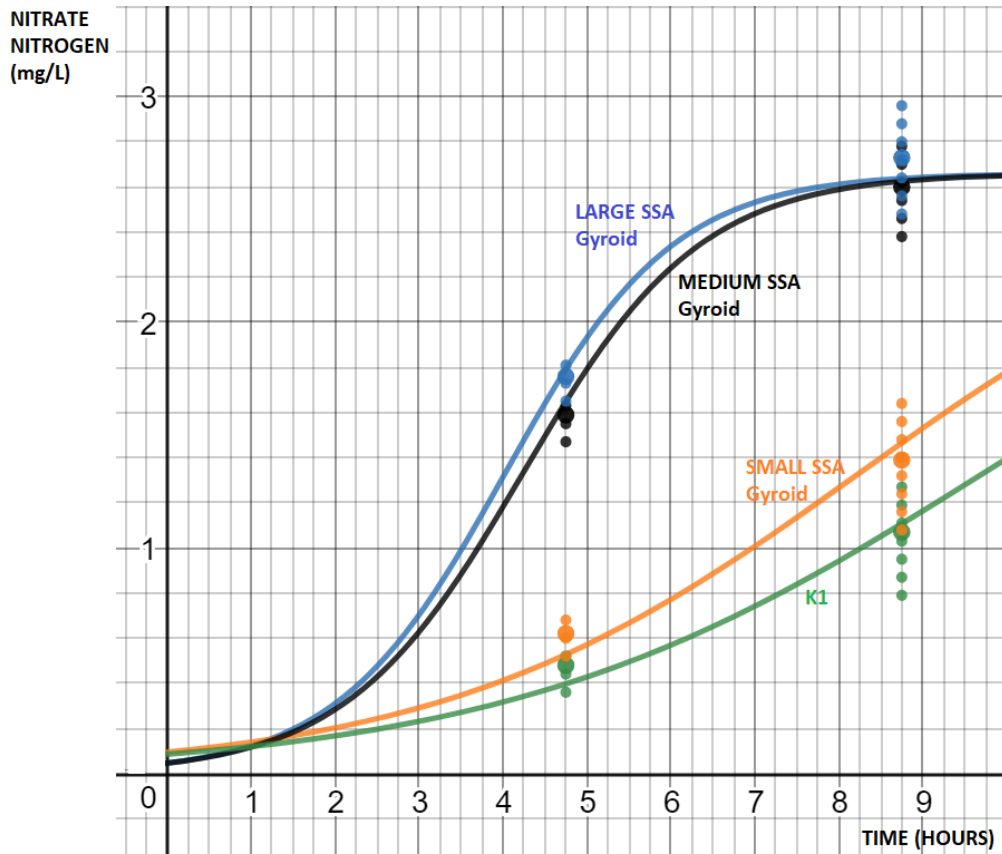


Figure 76: Nitrate production results fitted in a logistic curve (Hypothesis 1)

Table 32: Logistic curve fitting for nitrate production on hypothesis 1

Treatment	Logistic Function	Production rate (mg/L/hours)	R ²
Large SSA gyroid	$S(t) = \frac{2.66}{1 + 56e^{-1t}}$	1	0.9976
Medium SSA gyroid	$S(t) = \frac{2.66}{1 + 56e^{-0.95t}}$	0.95	0.9986
Small SSA gyroid	$S(t) = \frac{2.66}{1 + 27e^{-0.4t}}$	0.40	0.8965
K1	$S(t) = \frac{2.66}{1 + 30e^{-0.35t}}$	0.35	0.8777

Results from hypothesis 2 showed a better removal performance for gyroids than the others at the end of the whole treatment ($p=0.000$), whereas K1 treatment removed less

ammonia. It is important to highlight the performance of medium SSA gyroids, because, similar to earlier experimentation for hypothesis 1, almost 100% of ammonia was removed with the same removal rate as in hypothesis 1 (0.40 mg/L/hour), even though the number of carriers was reduced (25 to 13) due to the design conditions of keeping the same surface area for all treatments. A potential reason for this performance is that under the new conditions for proving hypothesis 2, by reducing the number of biocarriers, greater agitation patterns might have generated improved mixing intensities and enhanced oxygen transfer (Nogueira et al., 2015; Weiss et al., 2005).

Similar to hypothesis 1, ammonia and nitrate data for hypothesis 2 was fitted in a logistic curve (see Figure 77 and Figure 78). Table 33 and Table 34 shows the mathematical expression for the logistics curve fitting and the rates of ammonia depletion and nitrate production.

The fitting curves for ammonia removal on hypothesis 2 show similar removal rates for all treatments, but particularly the medium SSA gyroid show a rapid change in ammonia concentration within the first four hours of water treatment, nearly twice as fast as the k1 treatment.

When comparing the amount of ammonia removed and the nitrates produced during experimentation for testing hypothesis 2, it can be observed that, within the error of measurement, nitrogen mass balance was achieved after transformation from ammonia to nitrate.

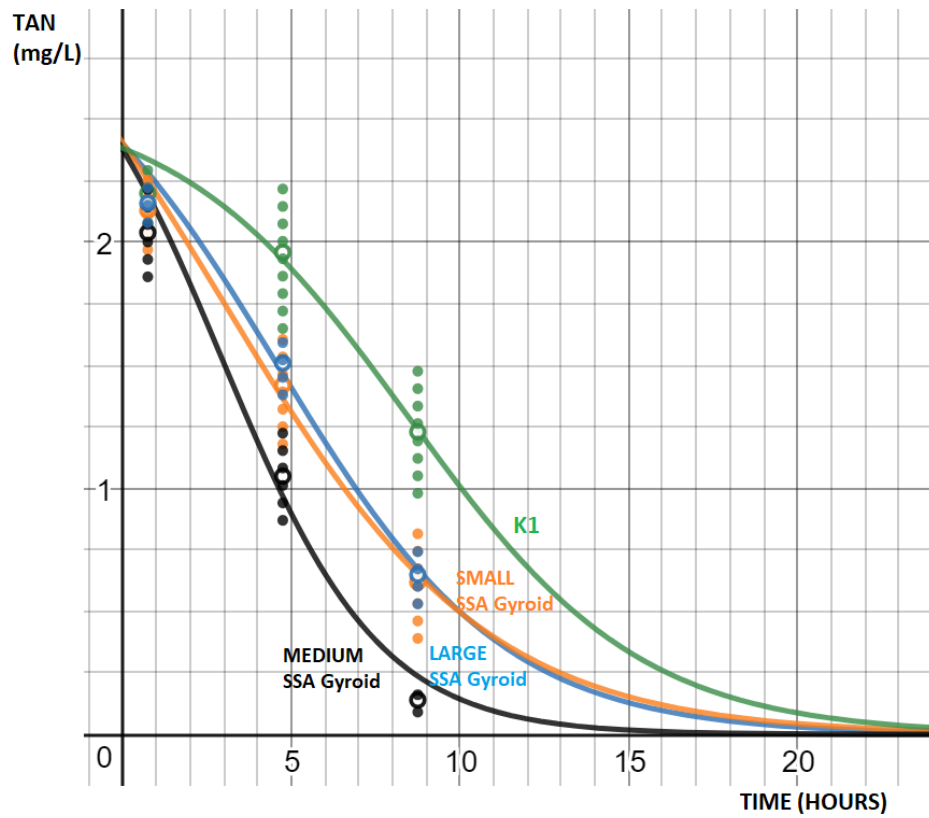


Figure 77: Total ammonia nitrogen results fitted in a logistic curve (Hypothesis 2)

Table 33: Logistics curve fitting for ammonia removal on hypothesis 2

Treatment	Logistic Function	Removal rate (mg/L/hours)	R ²
Large SSA gyroid	$S(t) = \frac{3.0197}{1 + 0.257317e^{0.297918t}}$	0.29	0.9861
Medium SSA gyroid	$S(t) = \frac{3.05384}{1 + 0.283434e^{0.427046t}}$	0.42	0.9834
Small SSA gyroid	$S(t) = \frac{3.53604}{1 + 0.469253e^{0.256794t}}$	0.25	0.9865
K1	$S(t) = \frac{2.58849}{1 + 0.085851e^{0.290482t}}$	0.29	0.9617

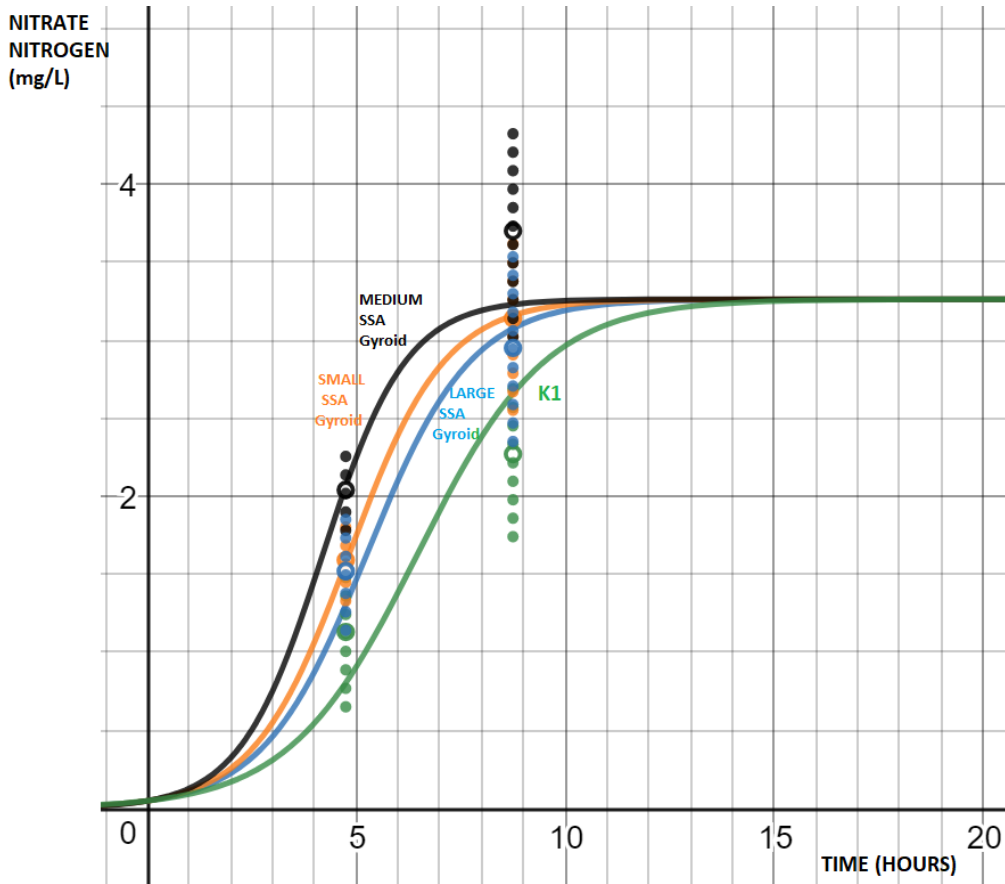


Figure 78: Nitrates production results fitted in a logistic curve (Hypothesis 2)

Table 34: Logistics curve fitting for ammonia removal on hypothesis 2

Treatment	Logistic Function	Production rate (mg/L/hours)	R ²
Large SSA gyroid	$S(t) = \frac{3.2623}{1 + 67e^{-0.86t}}$	0.86	0.9976
Medium SSA gyroid	$S(t) = \frac{3.2623}{1 + 67e^{-1t}}$	1	0.9986
Small SSA gyroid	$S(t) = \frac{3.2623}{1 + 67e^{-0.87t}}$	0.87	0.8965
K1	$S(t) = \frac{3.2623}{1 + 67e^{-0.65t}}$	0.65	0.8777

5.3.1. Economic Impact

A cost analysis is proposed based on the information from commercial providers.

A 1 ft³ bag of Kaldnes biocarriers was purchased at a garden supply for aquaponics & aquaculture applications at a cost of \$60. For fabricating gyroid media a bottle with 1 Kg of building material was purchased at a cost of \$300.

The weight of 200 mL packed biocarrier was measured with a digital balance to estimate the total cost based on weight (for gyroids) and volume (for K1s). Table 35 summarizes the previous information and calculates the total cost of fabrication based on the unitary costs.

Table 35: Cost analysis for treating 1.3 L of wastewater (15% fill ratio / 200 mL)

Biocarrier type	Volume		Weight	Unitary Cost		Total Cost
	(mL)	(ft ³)	(mg)	(\$ / mg)	(\$ / ft ³)	(\$)
Kaldness	200	0.0071	32,227	NA	60	0.42
Gyroid small SSA	200	0.0071	18,684	0.0003	NA	5.61
Gyroid medium SSA	200	0.0071	23,306	0.0003	NA	6.99
Gyroid large SSA	200	0.0071	36,568	0.0003	NA	10.97

With the information provided by Table 35, a summarized plot is presented in Figure 79. It includes the ammonia removal rates for each biocarrier type based on the concentration at the beginning and at the end of the 8-hour treatment.

Figure 79 illustrates two main points: 1) Increases in the SSA results in greater removal rates up to a certain level (probably below 1981 m²/m³) 2) Greater removal rates are associated with increases in the fabrication costs of the biocarrier.

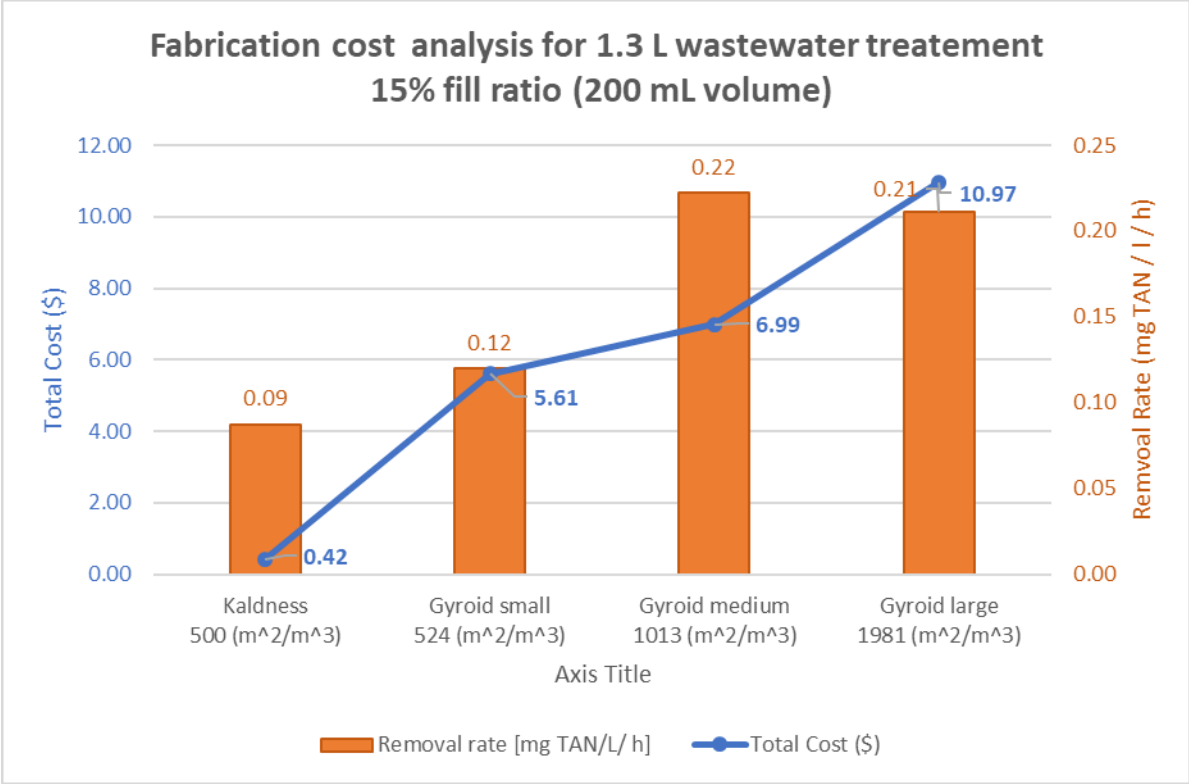


Figure 79: Cost and Removal Rate by biocarrier type

The cost analysis reveals that there is an increase in the fabrication costs of gyroids compared to K1. However, the increments observed in the fabrication costs within gyroids are not as high as those between gyroids and K1. Reports agree that raw material costs constitute the main component on the final cost of additive manufactured products, however, reductions in material costs are expected in the future (as has happened in the past) due to the role of the economics of scales on materials becoming more common (Thomas & Gilbert, 2014).

It is important to remark on the cost increments when fabricating a medium SSA gyroid and a large SSA gyroid and the lack of benefits in terms of ammonia removal rates. This

finding opens a research opportunity to identify the maximum SSA carrier capable to remove ammonia cost effectively.

6. Conclusions

It was possible to determine that, besides the benefits of having interstitial spaces for regenerating algal cultivations on surfaces (Kardel et al., 2015), the engineered generation of topographic features to obtain different interstitial surface area distributions contribute to accelerating the early stages of algal colonization on the substratum surface.

The offset of the algal biofilm observed on treatments with interstitial pockets upon the first day of harvest (5TH day of algal cultivation), could have been the result of continuous changes in the growth rate during the early stages of cultivation (from day 1 to day 4).

The capabilities to quantify the biomass during such early stages (day 1 to day 4 of cultivation) were out of reach with conventional measuring techniques. However, a refined methodology using freeze-dried weight and a microbalance made it possible to estimate the biomass from day 5 to 11 of cultivation.

The estimated growth rate calculated with the information from the last 3 days of harvest provide information about the status of each experimental treatment. Having slopes (growth rates) approaching zero, it brings the opportunity to approximate the overall algal biomass density profile to a logistic function given that, based on the growth rates, all experimental treatments reached their carrying capacity for their biomass density.

The logistic function approximation allows inference of growth rates for each experimental treatment during the actual five days of cultivation that were not quantified.

The experimental results were supported by CFD analysis. This computerized tool allowed the identification of some hydrodynamic effects that were caused by the experimental conditions that favored the substratum algal colonization. CFD analysis showed that the generation of features on the substratum provided reductions in the

average shear stress in the interior of the interstitial pockets, promoting better growing conditions during the first stages of algal colonization. Visual patterns of reduction in the shear stress on the substratum surface matched with regions with increased algal biofilm formation.

By characterizing the water velocity profiles inside the interstitial pockets, CFD analysis confirmed that the generated interstitial pockets constitute a quiescent region that provides drastic changes in the intensity and direction of the water flow due to the generation of eddies inside the pocket. Such vorticity in the pocket region induced different water flow profiles at the substratum boundary layer that were also subject of analysis.

Based on the information collected from the characterization of the water velocity at the boundary layer of the substratum, a model was proposed for the main forces (acting on any particle traveling through the pocket) in terms of the water velocity at the boundary layer. This model might be used to predict the initial pattern of cell deposition that initiates the colonization sequence for algal species.

The levels of geometrical complexity on the design and fabrication of biocarriers for water treatment processes were maximized with the capabilities of additive manufacturing. Three gyroid type biocarrier were fabricated with the increased specific surface area for nitrification of wastewater, and they were capable to operate into a lab scale MBBSBR. Gyroids were compared to standard commercial carriers under two different conditions: 1) keeping constant the volume of carriers in the reactor, and 2) keeping constant the total surface area for the water treatment process. Under both conditions, gyroids

performed better than the commercial K1, exhibiting a greater rate of removal of ammonia from a prepared synthetic water.

Gyroids with $1981 \text{ m}^2/\text{m}^3$ and $1013 \text{ m}^2/\text{m}^3$ reached almost 100% of ammonia removal within 8 hours when treatments were kept under same volume conditions, confirming that the increased surface area on both treatments was the factor that allowed a greater performance over the other two treatments.

When compared under same surface area conditions, the gyroids obtained greater ammonia removal percentage than K1 supporting the hypothesis that the geometry of the gyroids is a factor that brings better functionality to biocarriers.

With the combined effect of a larger surface area and enhanced geometry, it is able to use fewer carriers and still attain almost 100% of ammonia removal as well, providing support to previous findings that mixing intensities are a factor that improves nitrification rates in the water treatment process.

Given the level of complexity for fabricating the gyroid with $1981 \text{ m}^2/\text{m}^3$, the design of the gyroid with $1013 \text{ m}^2/\text{m}^3$ results in a more suitable biocarrier, functional enough for water treatment processes for nitrification.

The following are suggestions for future works on experiment 1:

- An experiment that includes the deposition of calcareous particles (or any other similar tracing compound) over the surface of the ATS and the printed plates to help the identification of local concentrations of such compound on the printed plates. The results could provide evidence of particle responses to the

hydrodynamics present in the ATS while supporting the hypothesized particle behaviors proposed with the CFD analysis.

- A CFD method to quantify the hydraulic retention time (HRT) inside the pockets would help to provide support to the proposed force analysis and a better understanding of the principles that promote particle deposition.
- The current project was performed under multidirectional water flow conditions given the nature of the ATS. It is necessary to test the same hypothesis under unidirectional flow conditions. Changes on the results would derive further investigations on flow dynamics.
- The experiment could have also been focused in terms of biofilm characterization. Prior to starting the experimentation, algal samples could have been taken from the surface of the ATS to identify species diversity present in the reactor. During experimentation, daily algal samples could have been taken from the interstitial spaces to characterize the succession of species during the development of the algal biofilm by microscopy.
- With the experimental results providing support that the maximum algal density is reached between day 10 and 11 of algal colonization, the same experimentation could be repeated without sampling three plates per day. Instead, all plates could be removed after 9 days of colonization and provide more statistical power with

more replicates (n=21). New results could be analyzed in terms of biomass productivity and probably by having more replicates the error might be reduced and differences between treatments might be identifiable.

The following are suggestions for future work on experiment 2:

- Include an additional hypothesis to test the percentage of ammonia removal but keeping the same numerical count of biocarriers among treatments. Results can provide support to the previous results and more information for marginal analysis from an economic standpoint.
- Future work needs to include tests on the performance of the gyroids under the exposure of organic wastewater, which will require more control over the levels of oxygen provided to the reactors. The current study did not assess conditions where the carrier was pushed to clogging, given the lack of organic matter supplied to the synthetic water and due to the duration of the whole experimentation (5 months, including inoculation period). However, it is expected that treatments that did not perform as well as the gyroids with 1981 m^2/m^3 and 1013 m^2/m^3 might show special capabilities as a response to experimental conditions different than those tested in the current experiments. For example, given the geometry of the gyroids, both the one with 1013 m^2/m^3

and with $524 \text{ m}^2/\text{m}^3$ might self-recover from accumulated biofilm or organic matter, likely providing optimal conditions for oxygen penetration to the inner layers of the biofilm (Hayder et al., 2017). Measures of the biofilm thickness, chemical oxygen demand test, and a mixed liquor suspended solid tests are some of the suggested methods that can be incorporated for the analysis of the performance of the carrier.

- Results from hypothesis 1 showed that increments in the surface area resulted in increased percentages of ammonia removal up to a saturation level (probably below $\text{SSA} = 1981 \text{ m}^2/\text{m}^3$). It would result interesting to identify the maximum level of specific surface area that provides proportional increases on ammonia removal rates. This way, the fabrication process can be handled more efficiently with reductions in labor and material consumption.

7. References

- Adey, W., Lockett, C., & Jensen, K. (1993). Phosphorus removal from natural waters using controlled algal production. *Restoration Ecology*, 1(1), 29-39.
- Adey, W. H., & Loveland, K. (2011). *Dynamic aquaria: Building living ecosystems*: Academic Press.
- Bachmann, N., la Cour Jansen, J., Bochmann, G., & Montpart, N. (2015). Sustainable biogas production in municipal wastewater treatment plants: IEA Bioenergy.
- Barber, J., & Tran, P. D. (2013). From natural to artificial photosynthesis. *Journal of The Royal Society Interface*, 10(81), 20120984.
- Barranguet, C., Van Beusekom, S., Veuger, B., Neu, T., Manders, E., Sinke, J., & Admiraal, W. (2004). Studying undisturbed autotrophic biofilms: Still a technical challenge. *Aquatic Microbial Ecology*, 34(1), 1-9.
- Barwal, A., & Chaudhary, R. (2014). To study the performance of biocarriers in moving bed biofilm reactor (mbbr) technology and kinetics of biofilm for retrofitting the existing aerobic treatment systems: A review. *Reviews in Environmental Science and Bio-Technology*, 13(3), 285-299. doi:10.1007/s11157-014-9333-7
- Barwal, A., & Chaudhary, R. (2015). Impact of carrier filling ratio on oxygen uptake & transfer rate, volumetric oxygen transfer coefficient and energy saving potential in a lab-scale mbbr. *Journal of Water Process Engineering*, 8, 202-208. doi:<https://doi.org/10.1016/j.jwpe.2015.10.008>
- Bassin, J. P., Dias, I. N., Cao, S. M. S., Senra, E., Laranjeira, Y., & Dezotti, M. (2016). Effect of increasing organic loading rates on the performance of moving-bed

- biofilm reactors filled with different support media: Assessing the activity of suspended and attached biomass fractions. *Process Safety and Environmental Protection*, 100, 131-141. doi:<https://doi.org/10.1016/j.psep.2016.01.007>
- Becker, K. (1996). Exopolysaccharide production and attachment strength of bacteria and diatoms on substrates with different surface tensions. *Microbial ecology*, 32(1), 23-33.
- Berg, H. C. (1993). *Random walks in biology*: Princeton University Press.
- Bhatnagar, A., Chinnasamy, S., Singh, M., & Das, K. C. (2011). Renewable biomass production by mixotrophic algae in the presence of various carbon sources and wastewaters. *Applied Energy*, 88(10), 3425-3431. doi:<https://doi.org/10.1016/j.apenergy.2010.12.064>
- Blersch, D. M., Kangas, P. C., & Mulbry, W. W. (2013). Turbulence and nutrient interactions that control benthic algal production in an engineered cultivation raceway. *Algal Research*, 2(2), 107-112. doi:10.1016/j.algal.2013.01.001
- Blersch, D. M., Kardel, K., Carrano, A. L., & Kaur, M. (2017). Customized 3d-printed surface topography governs species attachment preferences in a fresh water periphyton community. *Algal Research*, 21, 52-57.
- Borkar, R., Gulhane, M., & Kotangale, A. (2013). Moving bed biofilm reactor—a new perspective in wastewater treatment. *Environ. Sci. Toxicol. Food Technol*, 6(6), 15-21.
- Brinkley, J., Johnson, C., & Souza, R. (2008). Moving bed bio film reactor technology—a full-scale installation for treatment of pharmaceutical wastewater. *Chemical Business*, 77, 50-58.

- Burkholder, J. (1996). Interactions of benthic algae with their substrata. *Algal ecology-Freshwater benthic ecosystems*.
- Burkholder, J. M., & Wetzel, R. G. (1989). Microbial colonization on natural and artificial macrophytes in a phosphorus-limited, hardwater lake. *Journal of Phycology*, 25(1), 55-65.
- Cai, T., Park, S. Y., & Li, Y. (2013). Nutrient recovery from wastewater streams by microalgae: Status and prospects. *Renewable and Sustainable Energy Reviews*, 19, 360-369.
- Cao, J., Yuan, W., Pei, Z. J., Davis, T., Cui, Y., & Beltran, M. (2009). A preliminary study of the effect of surface texture on algae cell attachment for a mechanical-biological energy manufacturing system. *Journal of Manufacturing Science and Engineering*, 131(6), 064505-064505-064504. doi:10.1115/1.4000562
- Carrano, A. L., Blersch, D., Kardel, K., & Khoshkhoo, A. (2016). Understanding attachment preferences of benthic algae through controlled surface topographies on 3d printed substrata. Paper presented at the 5th International Conference on Surface Metrology (ICSM 2016).
- Chen, X., Kong, L., Wang, X., Tian, S., & Xiong, Y. (2015). Accelerated start-up of moving bed biofilm reactor by using a novel suspended carrier with porous surface. *Bioprocess and Biosystems Engineering*, 38(2), 273-285. doi:10.1007/s00449-014-1266-6
- Cho, S., Luong, T. T., Lee, D., Oh, Y.-K., & Lee, T. (2011). Reuse of effluent water from a municipal wastewater treatment plant in microalgae cultivation for biofuel

- production. *Bioresource Technology*, 102(18), 8639-8645.
doi:<https://doi.org/10.1016/j.biortech.2011.03.037>
- Christenson, L., & Sims, R. (2011). Production and harvesting of microalgae for wastewater treatment, biofuels, and bioproducts. *Biotechnology Advances*, 29(6), 686-702. doi:<https://doi.org/10.1016/j.biotechadv.2011.05.015>
- Chu, L., & Wang, J. (2011). Comparison of polyurethane foam and biodegradable polymer as carriers in moving bed biofilm reactor for treating wastewater with a low c/n ratio. *Chemosphere*, 83(1), 63-68.
- Colt, J., Lamoureux, J., Patterson, R., & Rogers, G. (2006). Reporting standards for biofilter performance studies. *Aquacultural Engineering*, 34(3), 377-388.
- Craggs, R. J., Adey, W. H., Jenson, K. R., John, M. S. S., Green, F. B., & Oswald, W. J. (1996). Phosphorus removal from wastewater using an algal turf scrubber. *Water Science and Technology*, 33(7), 191-198.
- Cui, Y., Yuan, W., & Cao, J. (2013). Effects of surface texturing on microalgal cell attachment to solid carriers. *International Journal of Agricultural and Biological Engineering*, 6(4), 44-54.
- Dong, Y., Fan, S.-Q., Shen, Y., Yang, J.-X., Yan, P., Chen, Y.-P., Li, J., Guo, J.-S., Duan, X.-M., & Fang, F. (2015). A novel bio-carrier fabricated using 3d printing technique for wastewater treatment. *Scientific reports*, 5, 12400.
- Ekong, J. (2017). Effect of three dimensional substratum features on benthic algal biomass productivity. Ph.D. Dissertation, Auburn University
- Elliott, O., Gray, S., McClay, M., Nassief, B., Nunnolley, A., Vogt, E., Ekong, J., Kardel, K., Khoshkhoo, A., & Proaño, G. (2017). Design and manufacturing of high surface

- area 3d-printed media for moving bed bioreactors for wastewater treatment. *Journal of Contemporary Water Research & Education*, 160(1), 144-156.
- Golueke, C. G., Oswald, W. J., & Gotaas, H. B. (1957). Anaerobic digestion of algae. *Applied microbiology*, 5(1), 47.
- Gong, W.-j., Liang, H., Li, W.-z., & Wang, Z.-z. (2011). Selection and evaluation of biofilm carrier in anaerobic digestion treatment of cattle manure. *Energy*, 36(5), 3572-3578.
- Graham, L. E., Graham, J. M., & Wilcox, L. (2016). *Algae* (Third ed.): LJLM Press, LLC.
- Granhag, L., Finlay, J., Jonsson, P., Callow, J., & Callow, M. (2004). Roughness-dependent removal of settled spores of the green alga *Ulva* (syn. *Enteromorpha*) exposed to hydrodynamic forces from a water jet. *Biofouling*, 20(2), 117-122.
- Gu, Q., Sun, T., Wu, G., Li, M., & Qiu, W. (2014). Influence of carrier filling ratio on the performance of moving bed biofilm reactor in treating coking wastewater. *Bioresource Technology*, 166, 72-78.
doi:<https://doi.org/10.1016/j.biortech.2014.05.026>
- Guillard, R. R., & Ryther, J. H. (1962). Studies of marine planktonic diatoms: I. *Cyclotella nana* Husted, and *Detonula confervacea* (Cleve) Grun. *Canadian journal of microbiology*, 8(2), 229-239.
- Guillard, R. R. L. (1975). Culture of phytoplankton for feeding marine invertebrates. In W. L. Smith & M. H. Chanley (Eds.), *Culture of marine invertebrate animals: Proceedings — 1st conference on culture of marine invertebrate animals* (pp. 29-60). Boston, MA: Springer US.

- Harlin, M., & Lindbergh, J. (1977). Selection of substrata by seaweeds: Optimal surface relief. *Marine Biology*, 40(1), 33-40.
- Hassan, M. F., Lee, H. P., & Lim, S. P. (2012). Effects of shear and surface roughness on reducing the attachment of *oscillatoria* sp. Filaments on substrates. *Water Environment Research*, 84(9), 744-752.
- Hayder, G., Ahmed, A. N., & Fu'ad, N. F. S. M. (2017). A review on media clogging in attached growth system. *International Journal of Applied Engineering Research*, 12(19), 8034-8039.
- Hem, L. J., Rusten, B., & Ødegaard, H. (1994). Nitrification in a moving bed biofilm reactor. *Water research*, 28(6), 1425-1433.
- Hofman, T., & Lees, H. (1953). The biochemistry of the nitrifying organisms. 4. The respiration and intermediary metabolism of *nitrosomonas*. *Biochemical Journal*, 54(4), 579.
- Irving, T. E., & Allen, D. G. (2011). Species and material considerations in the formation and development of microalgal biofilms. *Applied microbiology and biotechnology*, 92(2), 283-294.
- Kamstra, A., Blom, E., & Terjesen, B. F. (2017). Mixing and scale affect moving bed biofilm reactor (mbbr) performance. *Aquacultural Engineering*, 78, 9-17.
doi:<https://doi.org/10.1016/j.aquaeng.2017.04.004>
- Kardel, K., Carrano, A. L., Blerch, D. M., & Kaur, M. (2015). Preliminary development of 3d-printed custom substrata for benthic algal biofilms. *3d Printing and Additive Manufacturing*, 2(1), 12-19.

- Kaur, M. (2016). Effect of substratum topography on algal turf colonization and productivity under different nutrient conditions. Masters Thesis, Auburn University.
- Kinyage, J. P. H., & Pedersen, L.-F. (2016). Impact of temperature on ammonium and nitrite removal rates in ras moving bed biofilters. *Aquacultural Engineering*, 75, 51-55. doi:<https://doi.org/10.1016/j.aquaeng.2016.10.006>
- Koehl, M., Jumars, P. A., & Karp-Boss, L. (2003). Algal biophysics. *Out of the Past*, 115-130.
- Levstek, M., & Plazl, I. (2009). Influence of carrier type on nitrification in the moving-bed biofilm process. *Water Science and Technology*, 59(5), 875-882. doi:10.2166/wst.2009.037
- Mack, W., Mack, J., & Ackerson, A. (1975). Microbial film development in a trickling filter. *Microbial ecology*, 2(3), 215-226.
- Mahmoudkhani, R., Azar, A. M., Dehghani, A., & Goreishi, H. (2012). Treatment of contaminated waters with petroleum by moving bed biofilm reactor (mbbr). Paper presented at the International Conference on Life Science and Engineering, 10.7763/IPCBE.
- Metcalf, E., & Eddy, H. (2003). *Wastewater engineering: Treatment and reuse*. *Wastewater engineering, treatment, disposal and reuse*. Tchobanoglous g, burton fl, stensel hd: Tata McGraw-Hill Publishing Company Limited, 4th edition. New Delhi, India.
- Metcalf, E., & Eddy, M. (2014). *Wastewater engineering: Treatment and resource recovery*. Mic Graw-Hill, USA, 1530-1533.

- Miller, A. R., Lowe, R. L., & Rotenberry, J. T. (1987). Succession of diatom communities on sand grains. *Journal of Ecology*, 75(3), 693-709. doi:10.2307/2260200
- Nikitin, D. (1973). Electron microscopic studies of attached microorganisms. Modern methods in the study of microbial ecology. *Bull. Swed. Nat. Sci. Res. Council*, 17, 85-91.
- Nogueira, B. L., Perez, J., van Loosdrecht, M. C. M., Secchi, A. R., Dezotti, M., & Biscaia, E. C. (2015). Determination of the external mass transfer coefficient and influence of mixing intensity in moving bed biofilm reactors for wastewater treatment. *Water research*, 80, 90-98. doi:10.1016/j.watres.2015.05.010
- Norton, T. A., & Fetter, R. (1981). The settlement of sargassum muticum propagules in stationary and flowing water. *Journal of the Marine Biological Association of the United Kingdom*, 61(4), 929-940.
- O'Neill, M. E. (1968). A sphere in contact with a plane wall in a slow linear shear flow. *Chemical Engineering Science*, 23(11), 1293-1298. doi:[https://doi.org/10.1016/0009-2509\(68\)89039-6](https://doi.org/10.1016/0009-2509(68)89039-6)
- Ødegaard, H. (1999). The moving bed biofilm reactor. *Water environmental engineering and reuse of water*, 575314, 205-305.
- Ødegaard, H., Gisvold, B., & Strickland, J. (2000). The influence of carrier size and shape in the moving bed biofilm process. *Water Science and Technology*, 41(4-5), 383-391.
- Ødegaard, H., Rusten, B., & Westrum, T. (1994). A new moving bed biofilm reactor-applications and results. *Water Science and Technology*, 29(10-11), 157-165.

- Padisák, J., Soróczki-Pintér, É., & Rezner, Z. (2003). Sinking properties of some phytoplankton shapes and the relation of form resistance to morphological diversity of plankton—an experimental study *Aquatic biodiversity* (pp. 243-257): Springer.
- Quirynen, M., & Bollen, C. (1995). The influence of surface roughness and surface-free energy on supra-and subgingival plaque formation in man: A review of the literature. *Journal of clinical periodontology*, 22(1), 1-14.
- Reed, D. C., Laur, D. R., & Ebeling, A. W. (1988). Variation in algal dispersal and recruitment: The importance of episodic events. *Ecological Monographs*, 58(4), 321-335.
- Rodriguez, M. A. (1987). Estimating periphyton growth parameters using simple models1. *Limnology and Oceanography*, 32(2), 458-464.
- Rusten, B., Eikebrokk, B., Ulgenes, Y., & Lygren, E. (2006). Design and operations of the kaldnes moving bed biofilm reactors. *Aquacultural Engineering*, 34(3), 322-331. doi:<https://doi.org/10.1016/j.aquaeng.2005.04.002>
- Rusten, B., Mattsson, E., Broch-Due, A., & Westrum, T. (1994). Treatment of pulp and paper industry wastewaters in novel moving bed biofilm reactors. *Water Science and Technology*, 30(3), 161-171.
- Salvetti, R., Azzellino, A., Canziani, R., & Bonomo, L. (2006). Effects of temperature on tertiary nitrification in moving-bed biofilm reactors. *Water research*, 40(15), 2981-2993. doi:<https://doi.org/10.1016/j.watres.2006.05.013>
- Scardino, A., Harvey, E., & De Nys, R. (2006). Testing attachment point theory: Diatom attachment on microtextured polyimide biomimics. *Biofouling*, 22(1), 55-60.

- Scearce, S. N., Benninger, R. W., Weber, A. S., & Sherrard, J. H. (1980). Prediction of alkalinity changes in the activated sludge process. *Journal (Water Pollution Control Federation)*, 52(2), 399-405.
- Schnurr, P. J., & Allen, D. G. (2015). Factors affecting algae biofilm growth and lipid production: A review. *Renewable and Sustainable Energy Reviews*, 52, 418-429.
doi:<https://doi.org/10.1016/j.rser.2015.07.090>
- Schoen, A. H. (1970). Infinite periodic minimal surfaces without self-intersections. NASA technical note, NASA TN D-5541
- Seachem Inc. (2018). Seachem - marine salt. Retrieved from <https://seachem.com/marine-salt.php>
- Shapiro, O. H., Fernandez, V. I., Garren, M., Guasto, J. S., Debaillon-Vesque, F. P., Kramarsky-Winter, E., Vardi, A., & Stocker, R. (2014). Vortical ciliary flows actively enhance mass transport in reef corals. *Proceedings of the National Academy of Sciences*, 111(37), 13391-13396.
- Sheath, R. G. (1984). The biology of freshwater red algae. *Progress in phycological research*, 3, 89-157.
- Sindelar, H. R., Yap, J. N., Boyer, T. H., & Brown, M. T. (2015). Algae scrubbers for phosphorus removal in impaired waters. *Ecological Engineering*, 85, 144-158.
doi:<http://dx.doi.org/10.1016/j.ecoleng.2015.09.002>
- Solidworks. (2018). Numerical basis of cad-embedded cfd form. Retrieved from <https://www.solidworks.com/sw/numerical-basis-cad-embedded-cfd-form.htm>
- Sombatsompop, K., Songpim, A., Reabroi, S., & Inkong-ngam, P. (2011). A comparative study of sequencing batch reactor and movingbed sequencing batch reactor for

- piggery wastewater treatment. Maejo International Journal of Science and Technology, 5(2).
- Swanson, J., & Kittelson, D. (2008). A method to measure static charge on a filter used for gravimetric analysis. *Aerosol Science and Technology*, 42(9), 714-721.
- Tchobanoglous, G., Metcalf, & Eddy, I. (2014). *Wastewater engineering : Treatment and reuse*. London: McGraw Hill.
- Teughels, W., Van Assche, N., Sliepen, I., & Quiryneen, M. (2006). Effect of material characteristics and/or surface topography on biofilm development. *Clinical oral implants research*, 17(S2), 68-81.
- Thomas, D. S., & Gilbert, S. W. (2014). Costs and cost effectiveness of additive manufacturing. *NIST Special Publication*, 1176, 12.
- Thornton, A., Weinhart, T., & Bokhove, O. (2010). Modeling and optimization of algae growth. *Mathematics in Industry, Study Group Report*
- Tsoularis, A., & Wallace, J. (2002). Analysis of logistic growth models. *Mathematical Biosciences*, 179(1), 21-55. doi:[https://doi.org/10.1016/S0025-5564\(02\)00096-2](https://doi.org/10.1016/S0025-5564(02)00096-2)
- Vadeboncoeur, Y., Kalff, J., Christoffersen, K., & Jeppesen, E. (2006). Substratum as a driver of variation in periphyton chlorophyll and productivity in lakes. *Journal of the North American Benthological Society*, 25(2), 379-392.
- Vogel, S. (1981). *Life in moving fluids. The physical biology of flow*, 352 pp: Boston: Willard Grant Press.
- Vogel, S. (1996). *Life in moving fluids: The physical biology of flow*: Princeton University Press.

- Wang, Q., Squires, K. D., Chen, M., & McLaughlin, J. B. (1997). On the role of the lift force in turbulence simulations of particle deposition. *International Journal of Multiphase Flow*, 23(4), 749-763. doi:[https://doi.org/10.1016/S0301-9322\(97\)00014-1](https://doi.org/10.1016/S0301-9322(97)00014-1)
- Weiss, J. S., Alvarez, M., Tang, C.-C., Horvath, R. W., & Stahl, J. F. (2005). Evaluation of moving bed biofilm reactor technology for enhancing nitrogen removal in a stabilization pond treatment plant. *Proceedings of the Water Environment Federation*, 2005(14), 2085-2102.
- Zhang, X., Chen, X., Zhang, C., Wen, H., Guo, W., & Ngo, H. H. (2016). Effect of filling fraction on the performance of sponge-based moving bed biofilm reactor. *Bioresource Technology*, 219, 762-767.
- Zippel, B., & Neu, T. (2005). Growth and structure of phototrophic biofilms under controlled light conditions. *Water Science and Technology*, 52(7), 203-209.
- Zoetewij, M. L., van der Donck, J. C. J., & Versluis, R. (2009). Particle removal in linear shear flow: Model prediction and experimental validation. *Journal of Adhesion Science and Technology*, 23(6), 899-911. doi:10.1163/156856109X411247

Appendix I: Log data from ATS (Experiment 1)

Run 1	Date	Time	pH	Temp (°C)	Conductivity (ms)	Total water level (G)	Water Removed (G)	Water addition (G)	Nutrient addition (ml)
Harvest 1	24-Mar	20:51	7.85	24.7	0.1	27.5	12.5	15	7.5
Harvest 2	25-Mar	21:00	7.67	24.7	0.11	27.5	12.5	15	7.5
Harvest 3	26-Mar	21:30	7.63	24.2	0.11	27.5	12.5	15	7.5
Harvest 4	27-Mar	23:00	7.75	25	0.11	26	11	15	7.5
Harvest 5	28-Mar	21:50	6.97	24.9	0.1	27.5	12.5	15	7.5
Harvest 6	29-Mar	16:00	7.37	25.8	0.1	27.5	12.5	15	7.5
Harvest 7	30-Mar	21:00	7.74	24.4	0.1	26	11	15	7.5
Run 2									
Harvest 1	17-Apr	23:00	8.07	23.9	0.09	25	10	15	7.5
Harvest 2	18-Apr	23:00	7.89	24.5	0.09	25	10	15	7.5
Harvest 3	19-Apr	23:00	7.81	23.7	0.08	25	10	15	7.5
Harvest 4	20-Apr	23:00	7.78	23.5	0.08	25	10	15	7.5
Harvest 5	21-Apr	23:00	7.71	24.5	0.08	25	10	15	7.5
Harvest 6	22-Apr	23:00	7.7	24.9	0.08	25	10	15	7.5
Harvest 7	23-Apr	23:00	7.71	25	0.08	27.5	12.5	15	7.5
Run 3									
Harvest 1	16-May	5:30	7.61	24.2	0.06	25	10	15	7.5
Harvest 2	17-May	6:00	7.55	24.6	0.06	25	10	15	7.5
Harvest 3	18-May	6:00	7.51	24.7	0.08	25	10	15	7.5
Harvest 4	19-May	8:00	7.56	24.9	0.08	25	10	15	7.5
Harvest 5	20-May	7:00	7.58	25.1	0.08	25	10	15	7.5
Harvest 6	21-May	6:00	7.62	24.7	0.07	25	10	15	7.5
Harvest 7	22-May	9:00	7.57	24.8	0.08	25	10	15	7.5

